NTNU
Det skapende universitet

Effekten av akustisk strålingskraft på levering av nanopartikler til kreftvev

Mia Kvåle Løvmo

The effect of acoustic radiation force on the delivery of nanoparticles to tumor tissue

Mia Kvåle Løvmo

Preface

This masters thesis marks the end of my fifth and final year at NTNU, studying nanotechnology with specialization in Bio-nanotechnology. The thesis was carried out at the Department of Physics at NTNU and is part of a collaboration between NTNU, St. Olavs hospital and SINTEF. The collaboration is led by Professor Catharina de Lange Davies and is called "Multifunctional nanoparticles in diagnosis and therapy of cancer".

I want to thank my supervisor, Catharina deLange Davies, for letting me write my project thesis on this exciting topic, and my co-supervisor, Mercy Afadzi, for excellent training and guidance in the with US exposures. A great thanks to both my supervisors for the patients and for sharing your knowledge.

I am very grateful that I got to learn more about this research field that I have found especially interesting since I started studying Nanotechnology. Thanks to the whole nanoparticle group at biophysics at NTNU and for sharing your expertise, advise and research with me.

A great thanks to Astrid Bjørkøy, for training and assistance on the microscope.

A great thanks to Philip Lauffenburger for making matlab my friend and for all the support.

Lastly, to all my friends and family, thanks for all the support.

Trondheim, juni 2016
Mia Kvåle Løvmo

Abstract

By encapsulating chemotherapeutic agents in nanoparticles, cancer treatment could be improved, and in combination with ultrasound, the the drug delivery could be further optimized. While cavitational ultrasound (US) exposures earlier have been found to improve the extravasation of particles and microbubbles across the blood vessel wall, the penetration of the Extracellular Matrix (ECM) in tumor tissue still remains a barrier to drug delivery, with collagen predicted to constitute the main hindrance. In this project, the effect of focused non-cavitational US exposures on penetration of nanoparticles in collagen gels was investigated. Two types of nanoparticles were used; a commercial charge-stabilized polystyrene microbead and a PEGylated polymeric nanoparticle, the latter synthesized by SINTEF Materials and Chemistry. Nanoparticles in aqueous suspension were administered on top of collagen gel droplets and exposed to US. The fluorescent labeled particles intensity as a function of penetration into the collagen gel, were imaged with a confocal laser scanning microscope (CLSM) and resulting tilescans were analyzed with ImageJ and Matlab. The acoustic energy deposition from US exposures was not larger that the variations in deposition rates occurring from interactions of NPs and collagen fibers of various polymerization.

Contents

1. Introduction

"Cancer" is used as a term for a collection of diseases that are characterized by abnormal cell growth that can invade nearby tissue and spread to other parts of the body. Novel strategies for treating cancer are chemotherapy, often in combination with radiation, surgery, or immunotherapy among others. These treatments are not efficient and repetitions are therefore required giving rise to increased side effects and limits the likelihood of cure and recovery. To be able to fight cancer specifically, has been a goal for chemotherapy by targeting fast dividing cells. However, the cancer cells are very similar to healthy cells, targeting remains unspecific [17], and cancer remains one of the leading causes of morbidity and mortality worldwide [98].

By utilizing nanotechnology, drugs can be encapsulated in various kinds of nanoparticles (NPs) that can circulate in the vasculature, passively accumulate in solid tumors and deliver chemotherapeutic agents specifically to the cancer cells and potentially leaving the healthy tissue untreated and increase the effect of the cancer treatment [46]. This is possible by utilizing certain cancers remodeling of their microenvironment in the body. There are several physiological barriers to overcome before an drugs can be delivered effectively and specifically to cancer cells. The circulation of nanoparticles in the vasculature was highly prolonged by the discovery of the surface modification molecule, Poly Ethylene Glycol (PEG), and reduced the immune system clearance of drug delivery vehicles significantly.

Another barrier to drug delivery is the crossing of the capillary wall. Several research groups are trying to design a stimulus responsive delivery of drugs with or without the use of a nano carrier platform to promote a tumor specific delivery [62]. This stimulus could be internal, such as pH change [87] or enzymatic activities [54] in the tumor ECM. The stimulus could also be externally applied as with temperature elevations [53], exposure to light [12] or exposure to ultrasound (US) waves traveling through the tissue [75, 66]. This project will focus on the use of US as a tool for NPs to overcome some of the physiological barriers to reach their target.

SINTEF Materials and Chemistry have developed such a novel drug delivery system based on biodegradable polymeric nanoparticles (PNPs). They are synthesized in a polymerization process where surface functionalities, drugs, contrast agents and other functionalities are fairly easy to incorporate ([68]). The particles have been used in studies to characterize their properties and their function, by scientists at the Department of Physics at NTNU, as of circulation time, degradation and stability of the particles, the cell uptake and the cytoxicity of the particles both in vitro and in vivo. In collaboration with SINTEF the nanoparticles have been optimized. Several types PNPs have been used in research and several PEGylation methods have been tried out.

If a particle reaches the solid tumor, and crosses the capillary wall, it still has to penetrate the connective tissue around the cells, before it can be taken up. This tissue consist of a complex assembly of collagen, glycosaminoglycans, and proteoglycans. Convection through the tumor tissue is poor due to

interstitial hypertension, leaving diffusion as the major mode of drug transport ([10]). The diffusion in the extracellular matrix of tumors therefore constitute a major barrier to drug delivery and is a topic for further investigation in this project thesis.

In this project, one SINTEF polymeric particle and will be compared with a commercial latex bead. The two different nanoparticles behaviour in collagen gel will be investigated in two regimes. One regime limited to diffusion only and one where a US exposure could potentially lead to an NP displacement and increased penetration.

Earlier work done with acoustic radiation force at NTNU, has revolved around using the radiation force along with acoustic cavitation and MBs in tumor models in mice. Also some work was put into simulating the radiation force produced by transducers of set parameters. In the in vitro work it is difficult to distinguish between the effects seen from sveral US exposures as well as to large variations in tissue.

1.0.1 Objectives

In my masters thesis I will correlate the diffusion of NPs to their different surface modification, and see if the distribution of them can be rendered by an applied US exposure.
I will attempt to develop a simple model of collagen for a potential proof of principle of the acoustic radiation force. I will try to improve the penetration of ECM, resembled by collagen gels with acoustic radiation force. If this is possible, I will optimize the US parameters for maximum effect.

2. Theory

2.1 Drug delivery

One of the most common novel cancer treatments up to this date is chemotherapy. Chemotherapyt involves cytotoxic chemotherapy drugs that primarily cause cell death and damage to fast proliferating cells. A desired property for a chemotherapeutic drug is specificity towards cancer cells. However, cancer cells are relatively similar to healthy cells and non-specificity of cytotoxic agents is a major drawback and potential to damage normal tissues and recovery from cancer with chemotherapy is often not achieved [17].

One approach to optimize cancer treatment is the use of a carrier to deliver drugs more specifically and efficiently to cancer cells. To achieve this, the cytotoxic drugs can be encapsulated in some kind of capsule or particle. This drug carrier need to be bio-compatible, meaning that no large response in the immune system should be triggered when it is incorporated into the body. The carrier should also be targeting diseased cells, meaning that it is selective to diseased cells and causes a higher concentration of drugs in diseased cells, than in healthy tissue.

Opsonization - the initial barrier to drug delivery

To reach the cancer cells in the body, drug carriers must circulate in the vasculature. Most drug delivery carriers are foreign objects to our body and are attacked by immune cells of the mononuclear phagocytic system (MPS) once they are administered into the bloodstream. Initially, the MPS is binding opsonin proteins to the carrier surface. After the opsonization, the carrier's surface is coated in opsonin and readily ingested by a phagocyte [72]. Since the initial opsonization of drug carriers in the vasculature is critical for the phagocyte recognition, much research have been conducted on how to avoid this step of the body's clearance process and have resulted in technologies utilizing stealth strategies for drug carriers, as described further in section 2.6.

2.2 Tumor tissue characteristics and the EPR effect

As mentioned before, a major obstacle for chemotherapy is the difficulties in distinguishing cancerous cells and normal cells. However, there are some typical characteristics of cancers, although the characteristics vary significantly between cancer types. Typically cancer cells have abnormal activities leading to changes in the tumor environment allowing the tumor to grow rapidly. To allow for the rapid growth of a tumor, increased supply of nutrients and oxygen is needed. Cancer cells typically have an up-regulated

secretion of pro-angiogenic factors to surrounding tissue, resulting in growth of new blood vessels that connect the tumor to the body's vascular system. Because of the rapid growth, these blood vessels are abnormal with poor differentiation, chaotic architecture and increased permeability [46]. The endothelial and pericytes cells lining the capillary walls of these abnormal capillaries, are "leaky". The gap between endothelial cells in healthy vessels are typically $5-10nm$, while for vessels in cancerous tissue the gap can be as much as $2\ \mu$m [41].

Cancers often lack functional lymphatic vessels [7]. The "leaky" vessels, along with a lack of lymphatic system leads to a increased permeability, decreased rate of clearance and these effects results in an elevated interstitial fluid pressure (IFP) in solid tumors.

The increased permeability and reduced clearance by the lymphatic system results in an accumulation of macromolecules in tumors compared to normal tissue, making the macromolecules tumor selective. This forms the basis for the Enhanced Penetration and Retention (EPR) effect that can be utilized for passive accumulation of drug delivery vehicles in many cancer types. The EPR effect could possibly be increased by the simultaneous use of radiation, microbubbles and ultrasound (US) and or digestive ECM enzymes (collagenase/hyaluronic acid) and or active targeting [68, 22, 29].

Drug carrier characteristics

To overcome the physiological barriers in the body and benefit from the EPR-effect, the properties of the drug delivery vehicles can be tailored to maximize accumulation. The size, charge and polarity are important regards to drug delivery.

Size: The size should be of sufficient drug load and stability but still not effect extravasation and diffusion to a large extent.

Charge: Particles with highly charged surfaces are removed efficiently from the circulation by MPS, the liver and kidneys [5, 24]. On the other hand, the extravasation across the blood vessels and in the tumors are increased for positively charged macromolecules [25]. Charge is also related to how well a particle diffuse in interstitial medium, and neutral particles seem to diffuse faster [60, 96, 28].

Polarity: Hydrophobic molecules are associated with serum proteins and are recognized and metabolised by the liver [5]. Therefore, the nanoparticles should have a hydrophilic surface.

2.3   Nanoparticles and medicine

The term, "Nanoparticle" (NP) is typically referring to particles with a diameter in the nano-scale range (1-1000 nm), or to particles that show a certain behavior. NPs used for medicine, allows for interactions with cells and molecules in the body on the same size scale, and the large surface to volume ratio in NPs leads to various properties that will interact differently than their bulk counterparts [101]. The properties of NPs can be manipulated and utilized for various applications [45, 6].

For drug delivery purposes, the NPs can be loaded with chemotherapeutic agents as well as contain surface modifications to tailor the interactions of the NPs in the body. There is a large interest in developing biodegradable NPs as effective drug delivery devices. Biodegradable NPs have been used frequently as drug delivery vehicles due to their bioavailability, better encapsulation, controlled release and less toxic properties [55]. Nanosized carriers behave differently when interacting with biological barriers.

Some types of NPs show more promising characteristics in studies of the effect of penetration into skin and through tissue [34].

Polymeric particles, liposomes, dendrimers, solid lipid particles (SLN), metallic particles, mineral particles, Carbon nanotubes (CNT)/fullerenes and Quantum dots (QD)/ semiconductor nanocrystals are a few common classes of NPs, all biocompatible. Possibly the carbon materials could have a toxic effect in the body.

Polymeric particles

For drug delivery purposes, the most promising and mostly applied carrier technology is based on polymeric materials [85]. The use of polymer particles, Poly (alkyl cyanoacrylate) nanoparticles (PACA NPs) as drug carriers emerged in the 1980s due to their size, structure, degradability, and drug sorptive properties [18]. The field of polymer nanoparticles (PNP) is quickly expanding and is thought to be useful in many different areas like electronics, photonics, pollution control, medicine among others [36].

In the experimental work of this project, one subgroups of (PACA) NPs have been studied, poly(isohexyl) cyanoacrylate (PIHCA). The particle used is a SINTEF produced particle called Targ-233. In addition a commercial microsphere (latex bead) have been used.

2.4 Polystyrene bead

The polystyrene bead is a spherical particle in the colloidal size range that is formed from an amorphous polymer such as polystyrene. The bead is manufactured using high-quality, ultraclean polystyrene, with rights reserved to Thermofisher Scientific. A polystyrene chain is a linear hydrocarbon chain with a benzene ring attached to every second carbon atom. The aromatic rings control the way the chains coil and entangle and dominate the space; when a model of the particle surface is viewed all that can be seen is randomly stacked benzene rings with an occasional chain end sticking out. Thus the surface is very hydrophobic in character and provides for strong physical adsorption of molecular species with hydrophobic regions. Surfactants and protein molecules stick strongly by simple passive adsorption. The microsphere used in this project had a carboxylate-modified with a high density of pendent carboxylic acids on their surface. Such surface modulation make beads suitable for covalent coupling of proteins and other amine-containing biomolecules.

2.5 Polymeric NP synthesis

Several methods are developed and successfully utilized to prepare PNPs. These methods can be separated in two main types; Preparation of PNPs by dispersion of preformed polymers and preparation of PNPs through the polymerization of monomers. The nanoparticles used in the experimental work of this project had been made using a miniemulsion polymerization technique. When making particles with a hydrophobic core, a monomer of low water solubility, co-stabilizer, and the substance being encapsulated are mixed together in a oil-phase. The water-phase contains a surfactant and is usually acidic to have a surplus of protons. An initiator is usually also added and can be in both phases depending on its

properties. The two phases are mixed and high shear forces are applied using a sonifier or a mechanical homogenizer [68]. The structure of The IHCA monomer is used in Targ-233 is shown in Figure 2.1.
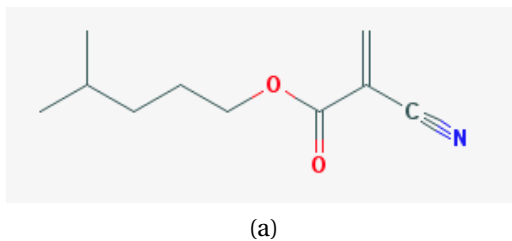

(a)

Figure 2.1: The structure of the IHCA monomers.

2.6 PEGylation

As mentioned earlier, stealth strategies are utilized to decrease opsonization of NPs in the vasculature. The addition of an inert molecule on the surface of nanoparticles is shielding the NPs charge and interactions with the environment, and is showed to increase circulation time and diffusion time of particles in vasculature and in tissue and tissue models [65, 51, 58, 74]. Later reports have also showed contradictory results of PEGylation, leading to a reduced drug delivery effect for certain cancers [97].

NPs without any kind of stealth strategy is efficiently removed from the blood circulation within minutes or at most a few hours by the mononuclear phagocyte system (MPS) [67]. Some strategies have been studied to work around this problem such as dextran conjugation [56], dendrimers [91], poly(ethylene oxide) [79], but PEGylation have shown to be most promising. PEGylation is the process of attaching polyethylene glycol (PEG) polymer chains to molecules. In addition to lengthen the circulation- and diffusion time, PEGylation may affect other properties of NPs, like uptake in cells and stability in different solutions. There are three main properties of the PEG that impacts the circulation time of NPs; the structure of PEG chains attached, the number of PEG chains attached to the polypeptide and the chemistry used to attach the PEG to the NPs [81].

The basic structure of PEG is a linear or branched polyether with hydroxyl groups attached to each end:

$HO - (CH_2CH_2O)_n - CH_2CH_2 - OH$
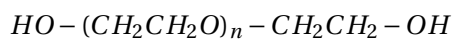
where n describes the length of the chain and is a crucial property of the PEG. The length is not easy to measure, so molecular weight (MW) is often used instead. Longer chains create greater steric hindrance, resulting in less recognition by macrophages and therefore lengthen the circulation time. The downside of long PEG chains is inhibition of cellular uptake and reduced active targeting properties [78]. Research indicates that a minimum MW of 2000 Da is required to achieve stealth characteristics [13].

Attaching the PEG to the surface of a PNP can be done both covalently and non-covalently. In the miniemulsion polymerization technique, the PEG can act as an initiator and simultaneously be grafted to the particle [68].

For Targ-233 used in this project, two types of PEG was added in the dispersion process of making the particles; one PEG initiator and one PEG stabilizer. The two PEG molecules seem to compete in the PEGylation process and the resulting composition of PEG on the NP surface is difficult to predict but possible to modulate by carefully selecting lipid mixtures used for preparation [35].

The resulting amount of PEG on NP surface can be measured with Nuclear Magnetic Resonance (NMR) if the PEG molecules on the surface can be differentiated. If not, the amount of PEG can be estimated by assuming that there is 100 % of one PEG.

The zetapotential of the particles are also an indication of how well PEGylated they are, since addition of PEG makes the zetapotential more neutral (shields the charge) [49].

The different kinds of PEG used in Targ-233 will be discussed in details in materials and methods, along with the surface modulation of the polystyrene bead.

2.7   Degradation of Nanoparticles

Understanding the mechanisms for degradation are important to be able to control the rate of release of therapeutic agents. PACA NPs are classified as nanospheres, where the therapeutic agents are dispersed throughout the polymeric matrix in contrast to nanocapsules where they are encapsulate in the core of the particles [37]. There are different pathways for degradation of NPs and the degradation pathway will vary depending on the conditions and surroundings.

Studies with PIHCA particles have showed that PIHCA NPs have a slower degradation rate than a PNP of a different monomer, PBCA [94]. The PBCA and PIHCA particles are thought to be taken up by cells by endocytosis [94, 59], suggesting an uptake before degradation is occurring.

2.8   Main barriers to drug delivery

To be able to use nanoparticles as drug carriers to treat cancer, the particles have to circluate in the vasculature as explained, then the NPs have to cross the capillary walls and diffuse through the ECM of the tumor interstitial medium to reach cancer cells and potentially be taken up by the cells. Some of the main barriers to drug delivery is therefore extravasation, ECM penetration and NP uptake [46]. As shown in Figure 2.2, intact lipsomes (labeled blue) containing the drug doxorubicin (green) has extravasated through the capillary wall but have not moved far from the vessels. The free drug, Doxorubicin, had penetrated the ECM up to 450 μm from the rim of the tumor [22]. The ECM penetration by nanoparticles is the barrier of interest for this project.

2.9   Extra Cellular Matrix (ECM)

A significant volume of living tissue is occupied by interstitial medium (IM) surrounding cells in a tissue. This space is filled with the extracellular matrix (ECM) and are composed of a fibrous network of proteins and glycosaminoglycans (GAGs). This matrix is organized at the surface of the cells that produce them and form a network between cells ([39]). Aside from role in structure and support, the ECM has a major role in cell regulation, migration, proliferation, and survival.

Collagens are large fibers and constitute the largest protein content of the ECM. The collagens polymerize into long hydrophobic fibers and have a slightly positive total charge, although it is containing both hydrophilic and hydrophobic patches and both positive and negative charges along the fibers [60].
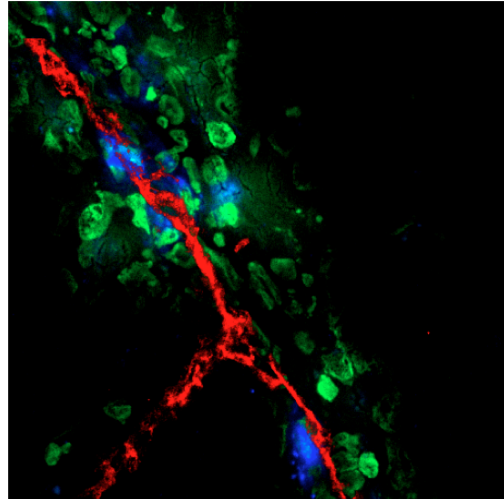
Figure 2.2: Localization of intact labeled liposomes (blue) and released doxorubicin (green) relative to capillaries (red). Intact liposomes (blue) were located close to the capillaries (red) [22].
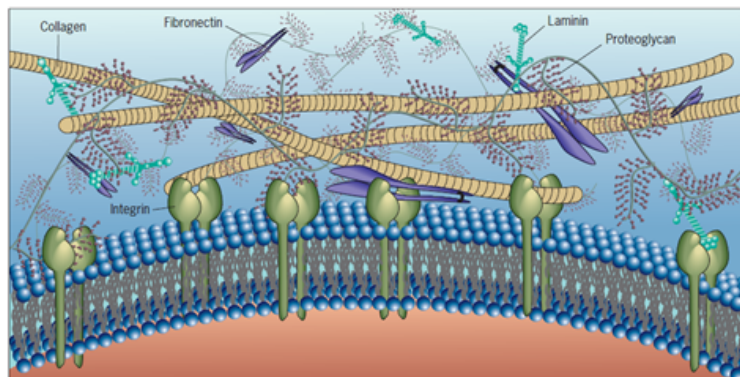
Figure 2.3: An overview of the extracellular matrix molecular organization. Collagen and other proteins as fibronectin and laminin contain binding sites for one another, as well as binding sites for receptors like integrins that are located at the cell surface. The proteoglycans are large protein polysaccharide complexes that occupy much of the volume of the extracellular space. This figure has been adapted from Cell and Molecular Biology Concepts and Experiments, by ([50]).

Hylauronan is a relatively stiff and hydrophilic polysaccharide with a total negative charge. HA is abundant in ECM and is one of the main backbones of the GAGs. These fibers and polysaccharides are depicted in Figure 2.4.

The collagen network has been suggested to be the main barrier for transport in the ECM [80], especially for larger molecules [30]. GAGs and proteoglycans are thought to reduce the diffusion of smaller molecules in the ECM [30] and has also been found to increase the hindrance presented by the protein network [16]. The role of the HA is contradictory in the ECM, and its influence is likely dependent on the diffusing agents characteristics. Being negatively charged, it is likely to interact with positive particles more than negative ones.

The focus of this project has been on making a very simple model to start with and based on these

previous finds, the model includes collagen, likely the main barrier to negatively charged particles. The model can be expanded to include more complex compositions if desirable at a later stage.

<div align="center">(a)   (b)   (c)</div>
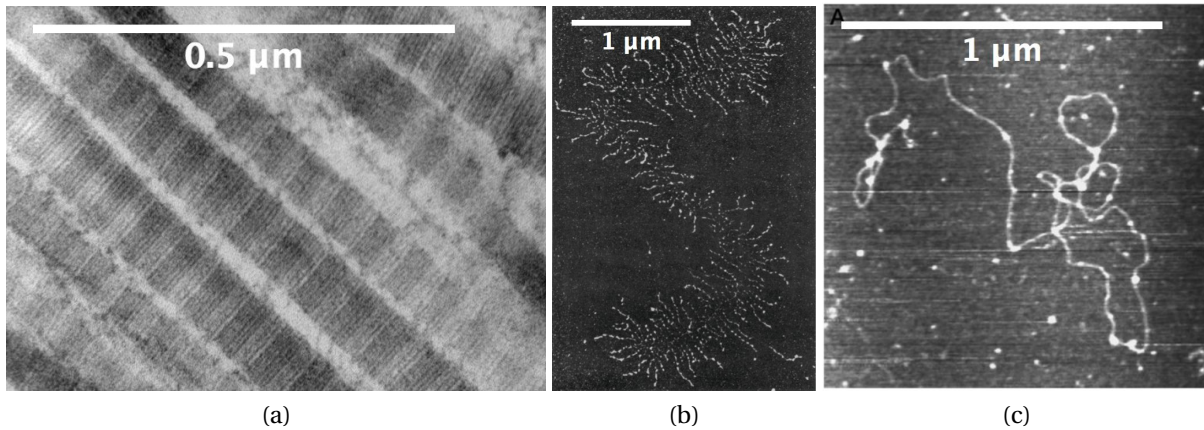
Figure 2.4: (a) Transmission electron microscope image of connective tissue area shows fibers of Collagen Type I, obtained from [42]. (b) Proteoglycan from cartilage imaged with dark field electron microscopy, obtained from [82]. (c) HA imaged with tapping mode atomic force microscopy. High molecular weight hyaluronan was deposited on mica from dilute aqueous solution and imaged in air, obtained from [19].

Collagen and HA content of cancer ECM

While ECM remodeling is very important in the normal development, many studies have also linked the remodeling of ECM to disease pathogenesis and, notably, to fibrosis [20].

The collagen and HA content varies between tissue types and between healthy and diseased ECM. In the table in Figure 2.5, the collagen and hyaluronic acid content of the interstitial matrix (IM) in four different tumors are presented, based on data from [70]. The following tumors were implanted in mouse dorsal chambers: human colon adenocarcinoma LS174T, mammary carcinoma MCaIV, human soft tissue sarcoma HSTS-26T, and human glioblastoma U87. These estimations are based on approximations regarding interstitial volume fraction and matrix component distribution, but the values can provide a rough basis for comparison of collagen content.

Tumor Type	Collagen Content (mg/g wet tissue)	HA Content (mg/g wet tissue)	IM Collagen (mg/ml IM)	IM HA (mg/ml IM)
MCaIV	1.8 ± 0.5	0.16 ± 0.03	9.0 ± 2.5	0.80 ± 0.15
LS174T	1.8 ± 0.5	0.11 ± 0.02	9.0 ± 2.5	0.55 ± 0.10
U87	8.9 ± 4.2	0.11 ± 0.03	44.5 ± 21	0.55 ± 0.15
HSTS26T	5.8 ± 1.1	0.16 ± 0.02	29 ± 5.5	0.80 ± 0.10

Figure 2.5: Interstitial matrix composition of human and murine tumors grown in mouse dorsal chambers (Made by [80] based on data of [70]).

(a)   (b)
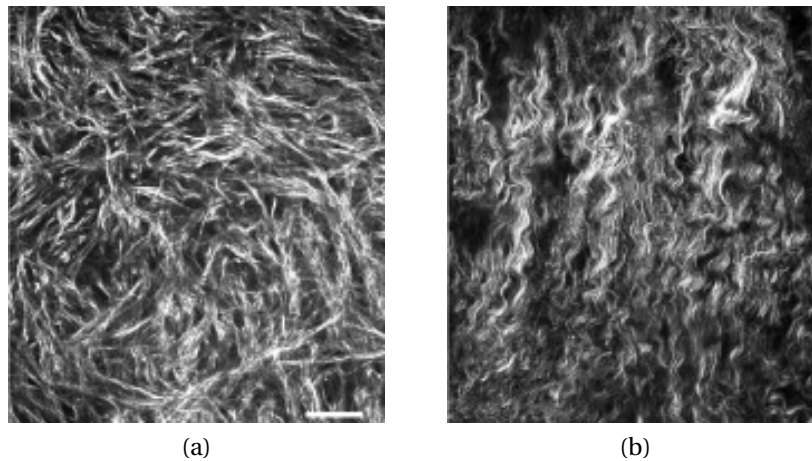
Figure 2.6: Images from [69] that have studied remodeling of ECM ovarian cancer. The collagen fibers in normal ovarian ECM (a) and in cancerous ovarian ECM (b) is imaged with Second Harmonic generation. Scale bar = 25 μm.

2.10 Determinants of interstitial transport

Diffusion coefficient (D) for particles and their dependence on particle radius (r) is described by Stokes-Einstein equation as seen in Equation 2.1. n is the viscosity of the medium, k_B is Boltzman constant and T is the temperature is Kelvin.

$$D = \frac{k_B T}{6\pi n r} \tag{2.1}$$

Transport of nanoparticles through the interstitial matrix is governed by diffusion and convection as seen in equation 2.2 ([47]).

$$\frac{\delta C_i}{\delta t} + v\nabla C = D\nabla^2 C_i + R \tag{2.2}$$

C_i is the nanoparticle concentration, v the interstitial fluid velocity, D the diffusion coefficient of the nanoparticles and R is a term that accounts for binding or degradation of the nanoparticles. The fluid velocity depends on changes in the interstitial fluid pressure and because the latter is uniform in the center of the tumor, it is negligible except at the tumor margin. The diffusion coefficient depends on the properties of the nanoparticles (size, charge and configuration) and the structure of the interstitial matrix [47].

Diffusion is a relatively slow process and drug delivery carriers do not succeed in reaching into the central areas of the tumor. Ultrasound exposures leading to a acoustic radiation force in the tissue, could increase the convection of particles in ECM and possibly increase the displacement, relative to diffusion only.

2.11 Diagnostic ultrasound

US is defined as sound waves with frequencies above what can be registered by human beings, i.e. above 20 kHz. US is convenient for imaging of soft tissue and blood flow, offering the possibility to safely and non-invasively acquire real-time images with low-cost equipment that can easily be transported. Controlled US waves are generated by piezo-electric elements within the transducer, generating longitudinal waves of compression and decompression. The waves propagate through soft tissue, and when they encounter areas where the tissue density changes a different acoustic impedance influence the US. In such interfaces, parts of the US wave is reflected. For diagnostic imaging this is registered by the transducer. The detected signal is processed by the scanner, resulting in an image that is a product of the amount of reflectors in the sonicated area and the location of the reflectors relative to the transducer.

2.12 Ultrasound and drug delivery

As the US waves propagate through tissue, physiological interactions between the waves and objects in the propagation pathway occur, which can be utilized for therapeutic applications. The potential of US as a therapeutic tool has been known for decades. The therapeutic intervention can occur without any invasive procedures, with a high degree of spatial precision and without any effect on the surrounding tissue. Three main biological effects of US have been described. Here, these effects are presented in relation to delivery of nanoparticles.

As a US wave propagate through tissue, it can loose energy by absorbance and reflection from the tissue. Depending on the US properties and the sonicated medium, applying US to a medium could generate heat, or the radiation force could generate an acoustic streaming or with microbubbles present,

an acoustic cavitation could be achieved. The US parameters used in this project was chosen to achieve acoustic radiation force, with minimal heating and below pressures of cavitation.

Hyperthermia

If the ratio of acoustic power relative to the area is large, thermal energy can be absorbed by the sonicated medium. In the case of delivery of nanoparticles, this temperature increase can have an impact on either the delivery system or the tissue itself. In this project, pulsed US waves were applied to tissue at an intensity that is not found to increase temperature.

Acoustic cavitation

The compression and decompression cycles of US can result in the occurrence of acoustic cavitation, which is the formation, oscillation and destruction of gas-filled micron-sized bubbles in the sonicated medium. In this project bubbles will not be added to the sonicated medium and the US pressures and frequency applied should not cause cavitation.

Acoustic radiation force

When applying ultrasound exposures using relatively high amplitudes, conditions of non-linear acoustics will typically arise. US-induced radiation force implies a transfer of momentum from the US beam to the sonicated medium. Radiation forces are proportional to the absorption coefficient of the medium and the rate of energy being applied and inversely proportional to the speed of sound of the ultrasound wave in the medium [90]. If the sonicated medium is liquid, the phenomenon results in a bulk movement of fluid in the propagation direction known as acoustic streaming. Radiation force is proportional to the rate of energy applied, and the direction and amplitude of the radiation force will depend on the elastic properties of the sonicated medium. Under appropriate conditions, radiation force can induce displacement of objects in the sonicated field in the same direction as the propagated beam [31]. If nanoparticles are located in the medium subjected to acoustic streaming, the nanoparticles will follow the fluid movement. Acoustic radiation force has demonstrated an effect on drug delivery systems in the vasulature, where the force was able to change the position of the particles [23]. Theoretical calculations and simulations can show a generation of an acoustic radiation force for the right US exposures applied to a system containing a medium with larger absorption than in water. However there are few studies that directly show the affect of acoustic radiation force alone on penetration of particles into tissue.

2.13 Experimental techniques

The main principles behind experimental techniques crucial for the interpretation of this projects results will be explained in this section.

Fluorescence and Stokes shift

To visualize and track nanoparticles, fluorescence is utilized in this project. Fluorescent molecules, also called fluorophores, respond distinctly to light compared to other molecules. As illustrated in Figure 2.7 (a), a photon of excitation light is absorbed by an electron of a fluorescent particle, which raises the energy level of the electron to an excited state. During this short excitation period, some of the photon energy is dissipated by molecular collisions, and the remaining energy is emitted as a photon to relax the electron back to the ground state. Because the emitted photon usually carries less energy and therefore has a longer wavelength than the excitation photon, the emitted fluorescence can be distinguished from the excitation light. This difference in absorbed and emitted wavelengths is called the *Stokes shift* and is shown in Figure 2.7 (b). The fluorophore can be repeatedly excited until it is reversibly damaged (Photobleached). Fluorescence (FS) is a common labeling technique in a broad range of research applications ([3]).
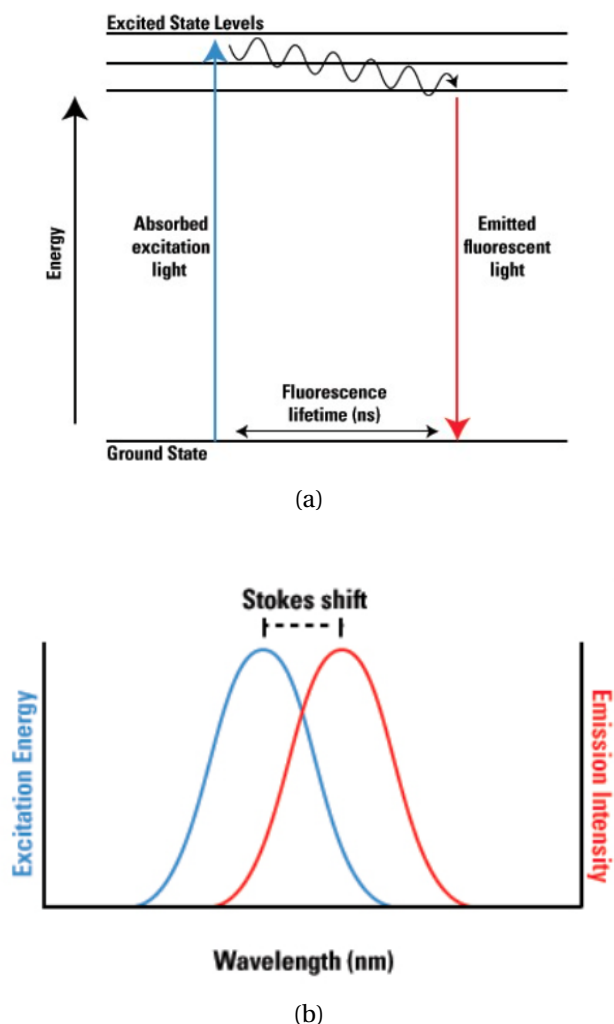

(a)

(b)

Figure 2.7: (a) Jablonski energy diagram of fluorescence. (b) The Stokes shift of the excitation and emission spectra of a fluorophore. Images from [86].

Confocal Scanning Microscopy (CLSM)

Fluorescence microscopy is a technique to visualize distributions of fluorescently labelled molecules within a sample in a non-invasive and specific way and is also compatible with complex biological systems like cells or tissues. However, the resolution is limited by the diffraction limit of light.

By using a pinhole, fluorescence emission from out-of-focus planes is eliminated and the contrast is enhanced in Confocal Laser Scanning Microscopy (CLSM). Compared to conventional wide-field microscopy where the whole sample is illuminated and imaged at once, CLSM is an approach, where a laser focus is moved through the sample while the fluorescence intensity is recorded. By knowing the position of the laser focus and the respective recorded intensity, a confocal image can be reconstructed ([33]). The principle for CLSM is summarized in Figure 2.8.
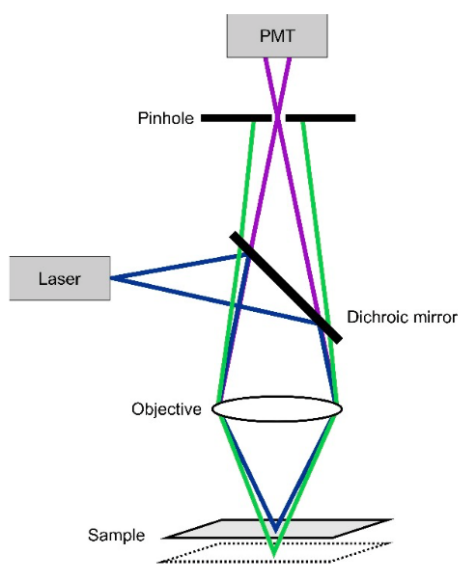
Figure 2.8: The scheme of a confocal laser scanning microscopy. The laser light is focused on the sample. The fluorescence passes the dichroic mirror and is detected by a photomultiplier (PMT). Out-of-focus light is eliminated by a pinhole and by scanning the sample an image is generated ([33]).

Raster Image Correlation Spectroscopy (RICS), RICS MANICS

RICS is a correlation analysis performed on a stack of images that can be used to measure diffusion of typically a molecule or particle. In the commonly used Fluorescence Correlation Spectroscopy (FCS), fluorescence fluctuations arising from the diffusion of labeled particles at a given focal point, are correlated with respect to a certain time delay. In RICS, these fluctuations are correlated between different focal positions separated by the time that the scanner needs to move from one spot to another. In this way, the temporal shift (used in FSC) is translated to a spatial shift. A laser scanner has a fast and a slow scanning axis, and can be used to measure diffusion of particles/molecules on different timescales. The scanning pixel time within a line, between lines and between images allows for correlation of particles on

timescales ranging from tens of microseconds up to seconds ([71]). RICS provides a powerful method to distinguish diffusion from binding and can be done with commercial laser scanning microscopes.

The change in concentration of particles as a function of time due to diffusion in a uniform medium is described by the relationship in Equation 2.3.

$$C(r,t) = \frac{1}{4\pi D t^{\frac{3}{2}}} exp\left(-\frac{r^2}{4Dt}\right), \tag{2.3}$$

where $C(r,t)$, concentration, is proportional to the probability of finding particles characterized by a diffusion coefficient D at position r at time t when the particles were at the origin ($r = 0$) at time $t = 0$. There are two parts of this equation, a temporal part and a spatial Gaussian term.

As different locations in a raster scan image are sampled, the intensity at one point is correlated to the intensity of the adjacent points if there is superposition of the point spread function (PSF) at the adjacent points.

Expressions for the spatial autocorrelation function were derived assuming that the intensity fluctuation is due to diffusion of a particle that is small compared to the PSF. In the temporal domain, the particle performs a random motion with an end-to-end distance that depends on the square root of time. In the spatial domain, the particle has a probability to be found at a distance from the original position that is described by a three-dimensional Gaussian with a variance that is related to the diffusion constant ([27]).

The autocorrelation function (RICS surface is defined in Equation 2.4.

$$G(\xi,\psi) = \langle \delta I(x,y)\delta I(x+\xi, y+\psi)\rangle / \langle I(x,y)\rangle^2, \tag{2.4}$$

where $I(x,y)$ is the matrix of intensities corresponding to an image from the stack and $\delta I(x,y) = I(x,y) - \langle I(x,y)\rangle$. The angle brackets illustrate averaging over all x and y positions. The intensity of each pixel is subtracted the average intensity from the entire stack, allowing a separation of mobile fraction of particles from immobile fraction.

The autocorrelation function for a system where molecules freely diffuse on timescales slower than the diffusion change their brightness. The scanning speed in an image must therefore be adapted to achieve this. At slow enough scanning speeds, RICS data has been demonstrated to correlate well with FCS data, but the speed should also not be too slow, not allowing accurate measurements because the pixels are separated too much relative to PSF.

A spatiotemporal correlation of the fluctuation in fluorescence is calculated for a region of interest in an image and an algorithm is used to solve the resulting non-linear least square problem. The Levenber-Marquardt algorithm (LMA), also known as the damped least-squares (DLS) method is one of these algorithm frequently used in software applications for solving curve-fitting problems, and the one was used for the analysis of particles in this project. [71]

RICS gives data about particles diffusion time, diffusion coefficient and number of particles in the confocal volume, with a few input parameters explained further in section 3.6.2.

3. Materials and methods

3.1 Overview of the experimental design

Detection of the effect of acoustic radiation force on NP penetration of collagen gels was approached with several setups and model designs, and the setup was a subject for continuous modifications and optimization. The main experiments involved a small volume of collagen gel deposited in the center of the bottom of a well, forming a flattened half sphere or droplet adhering to the plate, a cross section illustrated in Figure 3.1. Nanoparticles in suspension were added on top of the resulting collagen gel drops, fully covering the droplet before imaging. The droplets covered by NP solution were imaged before and after being put in a US exposure setup. Treated droplets were exposed to US from the top, perpendicular to the well plate, and control droplets did not receive US.
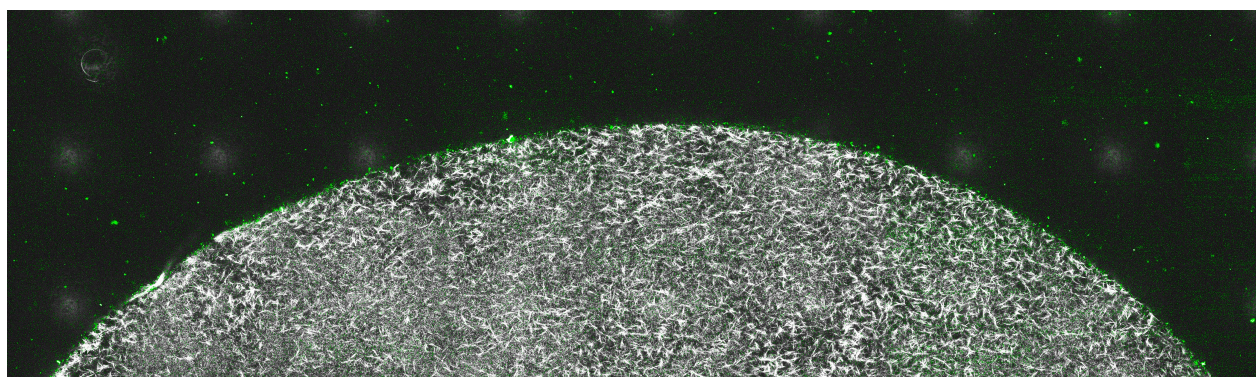

Figure 3.1: A section of a CLSM image of collagen (white) and NPs (green) illustrating the cross section of a collagen gel droplet covered in NP solution.

3.2 Nanoparticles

In this project two types of nanoparticles were used; polystyrene microspheres, 0.1FluoSpheres® yellow-green, provided by Thermo Fisher Scientific, see Appendix A, and one type of poly isohexyl cyanoacrylate (PIHCA) nanoparticle were used, Targ-233, synthesized and provided by SINTEF materials and chemicals. Properties of these particles are listed in Table 3.1. Hydrodynamic diameter and zetapotential determined by dynamic light scattering and laser Doppler velocity using a zetasizer (Malvern, NanoZ5), done by Einar Sulheim (IFY). The polymeric particle has a diameter more than 50 % larger than the polystyrene bead diameter. The surface modification of these two nanoparticles are very different giving rise to different zeta potentials. The polystyrene bead has a carboxylate-modified surface with a high density of pendent carboxylic acids on their surface, resulting in a relatively large negative zeta potential and charge stabilization. The polymeric particle has a high density of two types of PEGmolecules on its surface, resulting in close to neutral, weakly negative zeta potential and steric stabilization.

Table 3.1: NP properties:

The name, material, diameter, Poly Dispersity (PDI), Zetapotential, Fluorescence of the dye in the NP (FS Dye), and the surface modification of the NPs (Stabilization)are listed, along with the names of the PEG molecules of Targ-233.

Name:	Material:	Diameter (nm):	PDI:	Zetapot. (mV):	FS dye:	Stabilization:
FluoSphere01	Polystyrene	100 ±6		-51*	yellow-green	Charge-stabilized
Targ-233	IHCA monomer	177	0.17	-1*	NR688	PEG: Brij35 and Kolliphor

3.2.1 PEGylation of Targ-233

The amount of PEG on the surface for Targ-233 is within the range of $97 - 148$ chains/100 nm^2. These numbers are from unpublished data from Andreas Åslund. The amount of PEG is measured in chains (PEG molecules) per area of NP surface with Nuclear Magnetic Resonance (NMR). Two different PEG molecules are used in the process of making Targ-233. These two PEGmolecules are competing in the process as explained in section 2.6, and the resulting ratio of the two is unknown. Because these molecules cannot be distinguished with NMR, the range of PEG on the surface is calculated by estimating 100 % of each PEG molecule. The actual PEG amount value will be somewhere between those two values. Also the zetapotential is an indication of density of PEGylation as explained in section 2.6. The two different NPs are illustrated in Figure 3.2, along with the PEG molecular structure for Targ-233.

3.2.2 Fluorescent dyes

Encapsulated in the polystyrene bead, is a commercial "yellow-green" fluorescent dye with a excitation maxima at 505 nm and a emission maxima at 515 nm, following the procedures datasheet in Appendix A
.

(a) Polystyrene

(b) Targ-233

(c) PEG initiator: Kolliphore HS 15, M.W.: 961.27g/mol
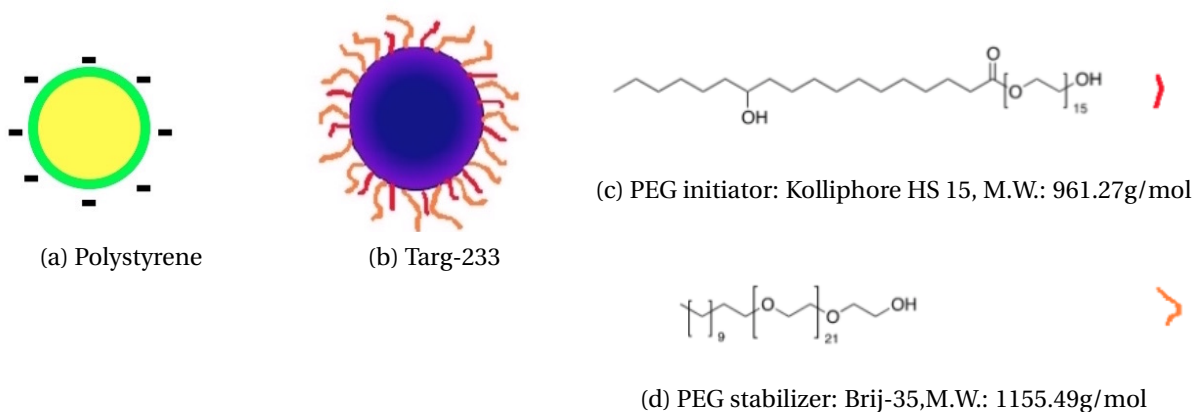
(d) PEG stabilizer: Brij-35,M.W.: 1155.49g/mol

Figure 3.2: Illustration of the nanoparticles and PEGylation of Targ-233 along with the structure of the PEG molecules.

Encapsulated in Targ-233 was a modified Nile red dye, (NR668) [52]. NR688 is highly lipophilic which limits leaking out of the NP [89]. It has excitation and emission maxima at 561 nm and 630 nm.

3.3   Sample preparation: Collagen gels

Collagen gels were made from rat-tail CORNING ® COLLAGEN 1 High Concentration (HC) (8 - 11 mg/mL), provided by BD Biosciences. Collagen gels were prepared following the manufacturer's protocol, which full version is included in Appendix B. In brief, collagen solutions were prepared by mixing solutions of 10X concentrated phosphate-buffered saline (PBS, Sigma-Aldrich), deionized water (DIH_20), 1 M sodium hydroxide, and concentrated collagen on ice. The final concentrations of collagen in these gels were 2.5 mg/mL.

Collagen solutions were vortexed and their final pH was adjusted to 7.2 ± 2 by addition of 0.1 M sodium hydroxide. 10 μL collagen was pipetted into the middle of the μ-slide 8-wells imaging plates (ibidi®), forming flattened droplets, illustrated in Figure 3.3. Small volumes of DIH_20 were placed in the corner of the wells not in contact with the collagen, to hydrate the environment and collagen gels were incubated at 37 °C for 30 min for polymerization, and stored in a fridge before use during the following 24 hours.

The collagen procedure was further optimized by following guidelines on fabrication of collagen gels from ibidi® [43]. These guidelines included minimizing total working time with collagen solution preparation, keeping the temperature of solution as low as possible (reagents on ice at least 10 minutes before mixing) and mixing all reagents thoroughly (the viscous collagen mixture does not mix well by diffusion).

Right before imaging, the DIH_20 in well corners were removed and 450 μL of NP solution of 12 μg/mL was added to each well, on top of the collagen drop, fully covering it. 450 μL of more of the same solution is again added at a later timepoint as explained in 4.3.

To correlate NP intensity in collagen experiments to concentrations, serial dilutions were made for computation of a standard curve. Serial dilutions were made for Targ-233 in 1XPBS and DIH_20, starting from 240 μg/mL and down to 3.25 μg/mL. A volume of 300 μL of concentrations at 240, 60, 15 and 3.25

were pipetted into wells before imaging.

3.3.1 Collagen gel and solution preparation for RICS

To compare the diffusion of the polystyrene NP with data obtained in my project thesis for Targ-233, a collagen gel and a PBS solution was prepared for RICS analysis following the same procedure as for Targ-233 [61].

For the gel experiment polystyrene NPs were mixed in 300 μL of collagen gel prior to the formation of collagen the fibers, resulting in a final collagen concentration of 5 mg/mL and a NP concentration of 120 μg/mL . PH was adjusted as above and 250 mL of the collagen-NP solution was pipetted into a ibidi well, forming a layer.

To measure diffusion of the polystyrene NP in PBS, NPs were mixed with DIH_20) and 10X concentrated PBS making the final concentration of NPs at 120 μg/mL and 1X PBS. 300 μL of this solution was pipetted into a ibidi well.

3.4 US exposure setup

The setup of the US transducer and collagen droplet a in well plate is shown in Figure 3.4 a). The transducer is held in place by a holder, custom made by the Mechnical Workshop at NT-faculty at NTNU, seen in Figure 3.4 a) and b) from the side and top down respectively. The holder has a cylindrical top that holds the transducer, and has a coned shape toward the end with an opening larger than the beamwidth of the FUS. In experiments it is filled with degassed deionized water for minimized attenuation of the propagated waves, and sealed with parafilm at the tip. The coned end fits the centered holes in the well plate lid and insures that the US beam hits the collagen droplet in the well. The length of the holder is 3 mm shorter than the focal distance of the transducers, ensuring that the ultrasound focus is approximately right above the collagen droplet and immersed in the NP-soultion covering the droplet. The well plate is resting in a holder immersed in a water tank with sound absorbing fabric at the bottom to minimize standing waves. To avoid gasbubbles between the sealed tip and the NP solution in the well, the well has to be completely filled with solution. 450 μL of the same NP solution as described in 3.3 of 12 μg/mL is again added before US exposure, but a large volume is pushed out as the transducer holder is submerged into the well immediately after. The solution filled space between the tip of the holder and the collagen surface is approximately 3 mm.
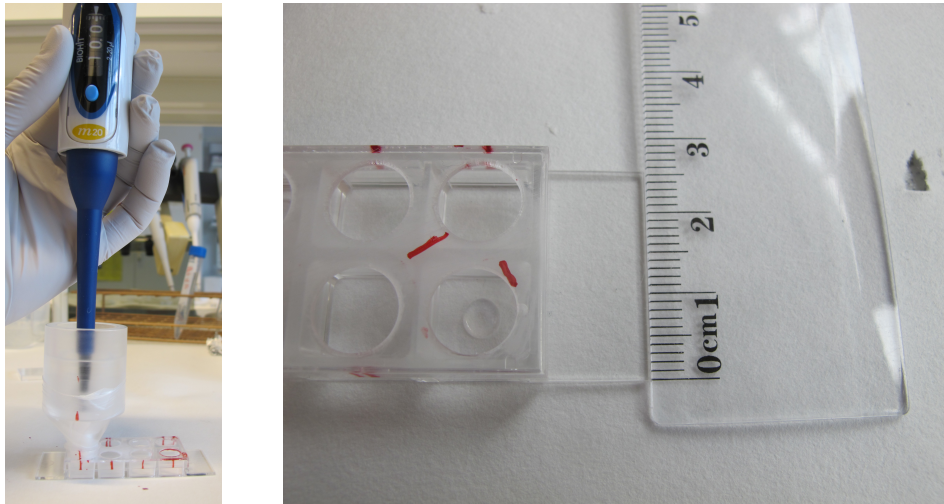
Figure 3.3: The collagen drops are placed in the wells using well plate lids with centered holes that fit the coned tip of the US transducer holder to ensure drops being hit by the FUS.
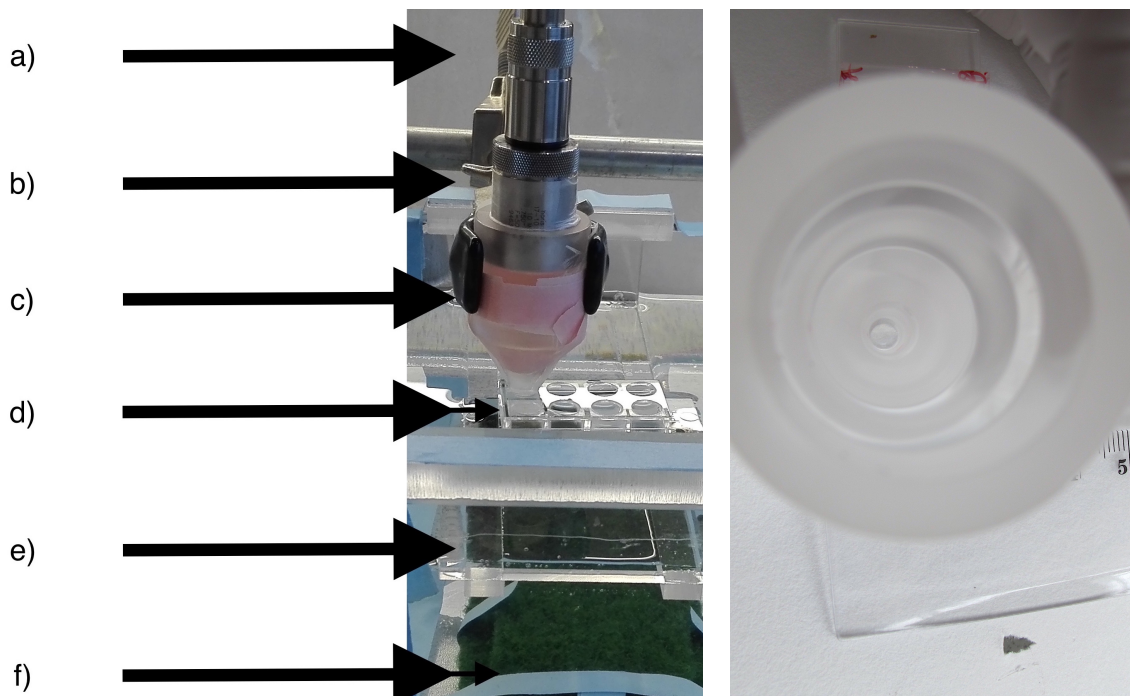
Figure 3.4: Experimental setup to the left: a) Cable connected to the power source, b) Transducer, c) Probe holder, d) Lid with holes leading the probeholder to the center of the well with the collagen drop and NP-solution, e) filled water tank, and f) sound absorbing mats. To the right a drop centered relative to the transducer holder is shown

3.4.1 Characterization of ultrasound transducers

Two focussed immersion transducers from Olympus of 5Mhz and 10Mhz respectively, were characterized in a water tank at Department of Circulation and Medical Imaging (ISB) at NTNU, together with Sigrid Berg. The measurements were performed with a Anglient waveform generator, a ENI 2100L RF Power Amplifier 50 dB, an LeCroy Wavesurfer 44Xs Oscilloscope and a Onda HGL- 0200 hydrophone along with a Onda AH-2010 preamplifier that amplifies the signal with 20 dB to receive the signal.

The data acquisition and data processing was carried out with a Matlab program custom made by ISB.

In this experiment the transducer is placed with the wave generating surface immersed in water, illustrated in Figure A.1 (however, in this illustration, the whole transducer is immersed in the water tank), while the hydrophone is moved around in the tank to sample the generated pressure field emitted by the transducer. This setup allowed for scanning along the x- and y-axis to localize the the maximum pressure at a z-distance around the focus given by the manufacturer. In this way the central axis of the ultrasound beam was found. An axis scan was performed by moving the hydrophone away from the transducer along this found central axis while measuring the pressure. The measurement started 20 mm away from the transducers surfaces and ended 116 and 80 mm away for the 5 and 10 MHz transducers respectively, sampling points separated by 1 mm along the central axis.

While keeping a constant Z-distance at the found focus of the beams, an array of 15 x 15 sample positions with 0.1 mm distance in the XY-plane were measured, to obtain a surface plot of the pressure at focus.
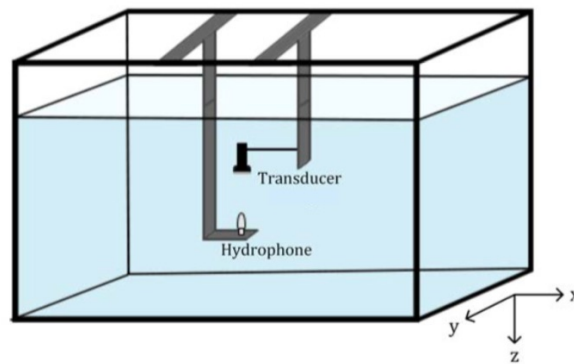
Figure 3.5: The experimental setup for the water tank transducer characterization. The figure is adapted from [44].

3.4.2 FUS transducers

The two transducers of 5Mhz and 10Mhz respectively, were used to apply acoustic energy to the NPs and collagen gel while establishing the experimental setup. Because of practical limitations with beam width size and exposure alignment, the data from the US exposed collagen drops included in the *Result section*, are all carried out with the 5Mhz transducer, with the larger beamwidth, and a few experiments with 10MHz is included in Appendix **??**.Therefore, only the US parameters used with the 5Mhz transducer are

included here. The active surface of the 5Mhz transducer is 19 mm and the distance between transducer surface and focus, the focal distance, is 70 mm specified by the producer.

3.4.3   US parameters

Pulsed ultrasound waves were generated and amplified with the same signalgenerator and amplifier as mentioned in section 3.4.1. The signal wave form was inspected with a LeCroy Waverunner LT262 Oscilloscope. The US was pulsed with one pulse consisting of 10 cycles equals to 2 μs pulselength. The burst period of 1 ms corresponds to a pulse repetition frequency (PRF) of 1 kHz. The total sonication time was 10 minutes, with a duty cycle of 0.2 %, which gives an effective US exposure of 1.2 s. Two amplitudes were used of 0.6 V and 1 V peak to peak (PP). An applied PP voltage of 0.6 V gave rise to a peak negative pressure of -1.05 MPa at focus of the transducer, corresponding to a mechanical index (MI) of 0.47. An applied PP voltage of 1 V gave rise to a peak negative pressure of -1.48 MPa at focus, corresponding to a MI of 0.66. The parameters are summarized in Table 3.2.

Table 3.2: US parameters:

The properties listed in this table are:
Amplitude; the peak to peak amplitude on the transducer in Volt,   **PnP**; the peak negative pressure at focus in Mega Pascals,   **MI**; the Mechanical Index,   **Cycles**; the number of cycles in one pulse,   **PRF**; the Pulse Repetotion Frequency in kilo Herz;   **Duty cycle**; the percentage of active transducer,   **Sonication time**; Total duration of treatment in minutes

Amplitude (V):	PnP (MPa):	MI:	Cycles:	PRF (kHz):	Duty cycle (%):	Insonation (min)
0.6	-1.05	0.47	10	1	0.2	10
1	-1.48	0.66	10	1	0.2	10

3.5   Imaging techniques

In the following section, the experimental techniques used to acquire data and analyze it are described. Imaging the US exposed collagen droplets and NPs and performing RICS analysis were done with two different CLSM microscopes.

3.5.1   CLSM procedure

Confocal images pre US exposure were acquired shortly after the polymerization of the collagen droplet, and again after US exposure or unexposed control. Experiments with the gels were repeated two times for each treatment group for each NP making new gels with NP solutions each time.

The collagen fibers and the distribution of NPs in gels, were observed using a confocal TCS SP8 microscope, Leica DMI 6000 CS AFC Bino inverted microscope with a water immersion objective HCX IRApo L *25X/0.95 NA* and a White Light Laser (WLL) (470-670nm wavelength). Collagen fibers were imaged in one channel with confocal reflection microscopy (CRM) with a laser gain of 539.1 and the light was detected

with a photomultiplier tube (PMT). NP fluorescence was imaged in an other channel. The pinhole aperature was set to 55 μm = 0.98 Airy Units.

Polystyrene

To observe polystyrene NPs in collagen gel, a WLL wavelength of 505 nm was used at a laser power of 10.9 % of 1mW. Collagen fibers were detected using a 499-513 nm band pass filter in front of the PMT detector. NPs were detected using a laser gain of 18.8 with a Hybrid Detector (HyD) and a 529-579 nm band pass filter.

Targ-233

To observe Targ-233 NPs in collagen gel, a WLL wavelength of 471 nm was used at a laser power of 35.6 % of 1mW. Collagen fibers were detected using a 464-477 nm band pass filter in front of the PMT detector. NPs were detected using a laser gain of 107.2 with the HyD detector and a 560-680 nm band pass filter.

PMT Targ-233

Because of technical problems with the HyD detectors, three experiments were repeated for Targ-233 with PMT detectors for both channels. The same settings as described for Targ-233 above were used, except the gain was increased to 714 % for detecting NPs with a second PMT detector.

Collagen droplets with nanoparticle solution were imaged top down in a centered region selected of about 2x2 or 1.5x1.5 mm^2, more than 1.5 times the size of the FUS beamwidth. Every image is a tile, a merged result of 5x5 or 4x4 images of 512x512 pixels and a pixel size of 826 nm. Tiles were acquired along the Z-axis shown in Figure 3.6, with a spacing of 1 μm between tiles, resulting in a tilescan, a Z-stack of tiles. To define a tilescan, the surface of each drop was found and the imaging was started about 30 μm above the surface and down in Z-direction between 140 and 200 μm for the defined area, as seen in Figure 3.6, where both the reflection channel and the FS channel are included.
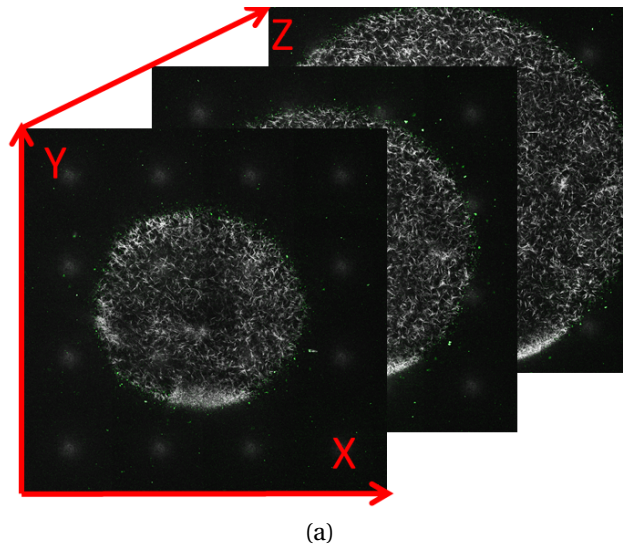

(a)

Figure 3.6: Three images from a tilscan with about 30 microns between each image. Both collagen and NPs are included in the image.

The four serial dilutions from 3.3, were imaged with the same settings for the FS channel as for the PMT Targ-233. The same area was chosen, however, the Z-distance imaged was only 36 microns.

3.5.2   CLSM for RICS analysis

Confocal images for the RICS experiments were acquired shortly after the polymerization of the collagen solutions mixed with NPs, using an inverted LSM 510 microscope (Carl Zeiss) with a water immersion objective C-Apochromat *40X/1.2 NA* and light was detected with a PMT detector with a 500-550 nm band pass IR filter and the pinhole aperature was set to 72 μm. For NPs in PBS solution these were imaged immediately after preparation. Experiments with the gel and in solutions for polystyrene were not repeated.

Collagen fibers were imaged with CRM using a HeNe laser at wavelength 543 nm at a power of 21.8 % of 1mW and a gain of 607 was used. For imaging polystyrene NPs, a Argon laser at wavelength 488 nm at a power of 2 % of 10mW and a gain of 652 was used.

Images for RICS analysis were obtained by taking consecutive images (frames), so called timeseries, of the NPs in the gels and solutions. The confocal volume created by the 488 nm laser focal point was placed randomly in the gel or solution and the nanoparticles were imaged following the same settings as above. For every RICS experiment, 12 and 15 frames at minimum 6 locations in the gel and solution respectively, consisting of 512x512 pixels, were collected. The scanner speed along the fast scanning axis was 51.2 μ s/pixel and the scanner step corresponding to one pixel was 54.9 nm.

3.6   Image analysis of collagen droplets

The image processing program Fiji ImageJ-win64, designed for scientific multidimensional images, was used for image analysis [83, 84]. The collagen CRM channel was used for qualitative analysis. To quantify the intensity of NPs in obtained images, the NP FS channel of each pre and post US tilescan were analyzed. To remove the background, the image threshold was set by Default method to a range from minimum 22 and maximum 255 gray values. The minimum value is found based on measurements of the background values with both Targ-233 and polystyrene. An ImageJ built in stack feature "plot Z-axis profile", that measures set values in a selected area as function of Z, Penetration depth into the collagen drop, was used.

Rectangular ROIs of 95 μm were stepped in a non-overlapping pattern throughout the tile as illustrated in Figure 3.7 a), plotting the Z-axis profile for each ROI, resulting in between 265 and 441 profiles. The Z-axis profile measurements were limited to threshold and the "Area" (the amount of pixels above the threshold) and the "Mean" (the mean intensity of the pixels above threshold) were measured.

Because of the convex surface of the collagen droplet, the surface of the collagen appears at different Z-values throughout an image as shown in Figure 3.7 b) with three Z-axis profiles plotted; one from an ROI in the center and two from an ROI in the periphery. The surface in the center of the droplet is found above the surface of regions towards the periphery of the droplet. Therefore a large area cannot simply me selected and analyzed to obtain a result of intensity versus penetration depth into the droplet.

The same analysis procedure as above was carried out for Targ-233 with the PMT detector. However, because of different imaging settings and detector the threshold was now set to minimum 4 in stead of 22, based on measured background values.
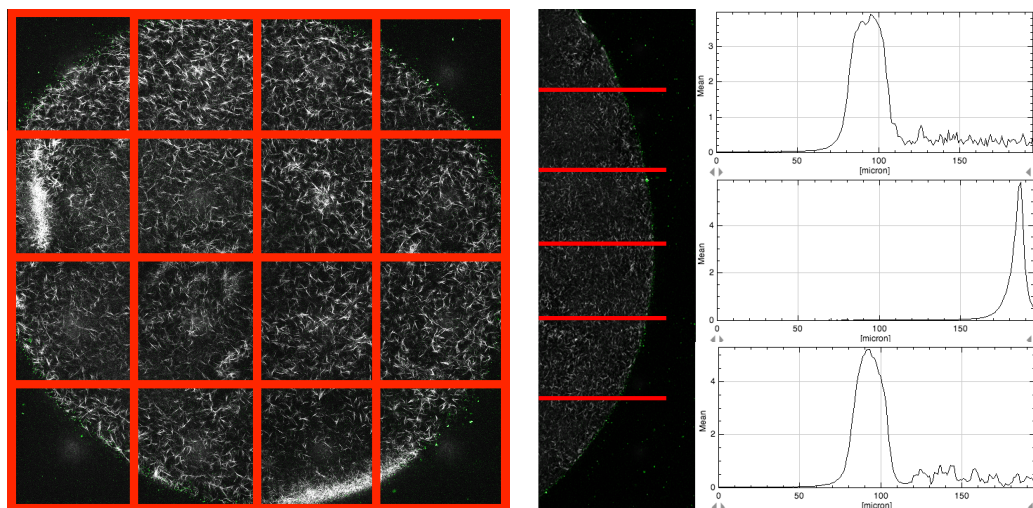
Figure 3.7: a) Tilescan is devided into small ROIs. b) A crossection of a tilescan is showed in this figure, along with The Z-axis profile plotted from ROIs originating in the center and in the periphery respectively.

3.6.1 Matlab analysis

The obtained data from ImageJ was imported to MATLAB R2014a for further calculations and plotting [63]. Some data figures were generated with Matlab and some with SigmaPlot 13.0 [88]. In Matlab each ROI data from pre and post US tilescans were treated separately at first: the number of pixels above threshold was multiplied with their mean intensity, resulting in a total intensity as a function of Z. The fact that NPs accumulate on the collagen surface, made it possible to define the surface for each ROI as the max value of total intensity.

Data from ROIs within a circular selection centered in the tilescan was selected. The selected area has a diameter of about 900 μm, 75 % of the FUS beamwidth. Even if the FUS beam did not hit in the center for all experiments, the same region had to be selected for all, and centering it was necessary to keep the convex surface contributions the same in all experiments. In addition the selected area had to be small enough to only include ROIs with intensity information from the surface and for a substantial depth into the drop.

In this selected centered region surface plots were obtained showing the max values of each ROI pre and post US and the difference between the two.

To find the intensity as a function of penetration depth for this centered region in total, all individual ROIs intensity plots were summed by placing the max values on top of each other for pre and post US separately. The two resulting intensity plots pre and post US were cut in both ends to include only information from Z-values that were mutual in all ROIs datasets, and were plotted on the same axis.

From these two resulting intensity plots pre and post US as a function of penetration into the drop, three main analysis were done:

1. Surface accumulation:
The max values of intensity were found and will be regarded as the accumulation of NPs on the collagen surface.

2. Change in NP distribution inside the collagen:

Because of the high accumulation of NPs on the collagen surface, it is likely that their intensity is leaking into sections in the tilescan before and after the surface. A value of 5 % of the max intensity of pre US peak was used as a limit for where this leakage is not included, and all data after this limit after the surface is regarded as being inside the collagen droplet. From this limit and 30 microns into the drop, the intensity was summed for pre and post US individually. In addition, there was an apparent low level of intensity that was reached inside the drop where the intensity graph flattens out at the very end of imaging. The mean values of the last 20 microns was calculated to correlate this region to amount of NPs at a maximum penetration into the droplet.

3. Change in NP distribution abovecollagen surface

The same index of the 5 % limit of the max intensity of pre US peak as defined above, is assumed symmetric around the peak, and all data before this limit before the surface is regarded as being in front of the collagen droplet. The change in NP distribution in front of the surface was calculated by summing the intensity from 5 microns before this point. In addition, the threshold in front of the droplet was calculated by taking the mean of the first 10 microns.

Based on the surface plots of the max values of intensity, it was possible to localize the coordinates of a hypothesized "max treated" ROI, and the intensity values for this region was also plotted, and analyzed in the same three steps as above.

The same analysis in Matlab was done for PMT Targ-233, but because a lower threshold was set in images, the 5 % limit was increased to 25 %.

Tilescans resulting from imaging the four serial dilutions, were thresholded in ImageJ as described for PMT Targ-233. The Z-axis profile was plotted for two circular, non overlapping ROIs of 900 μm in each tilescan. In matlab, the number of pixels above threshold was multiplied with their mean intensity. The mean value of the two ROIs in each of the four tilescans were found and the resulting standard deviation was computed for the this mean.

3.6.2 RICS Manics analysis

As described in section 2.13, RICS is a correlation analysis performed on a stack of images (timeseries). The autocorrelation functions were calculated with the use of the program RICS MANICS, written by Egor Zindy, School of Pharmacy and Pharmaceutical Sciences, at the University of Manchester.

Before the autocorrelation in MANICS, the mobile fraction and mobile average data were selected for analysis. An average image was calculated from consecutive images, for series of 12 and 15 frames, and the images were pixel-by-pixel subtracted from the particular image used for correlation analysis.

An autocorrelation of a selected region of interest was then calculated based on intensity correlation between pixels (the input data). The curve for the output data was fitted to this autocorrelation curve with four parameters that can be fixed or free; startpoint autocorrelation value (g0), beamwaist (w0), diffusion coefficient (D) and a structure factor (SP). A set structure parameter (SP = 5) was used following guidelines in the LSM Manual [100], and the remaining three parameters were set free. From this fitted curve, a diffusion time, beamwaist (w0), diffusion coefficient and number of particles in the confocal volume were calculated. The input data was clipped in the end (noise) and settings were adjusted to get a high as possible R squared value (R2) for the fit of the curve for each selected region of interest, and with the calculated parameters within reasonable ranges. A RICS map was calculated and exported for each

timeseries. It shows the calculated values for the whole frame divided into preset squares, and based on the fitting parameters for the selected region of interest. The RICS map is used to guide the analysis of selected regions of interest and shows the homogeneity for each sample.

Analyzing a sample of a particles with homogeneous behavior, as NPs freely diffusing in solution, is straight forward with RICS. A relatively large region of interest can be chosen almost anywhere throughout a frame throughout a timeseries. The autocorrelation fitted data plot was checked for every selected area and autocorrelation curves for correlation in x-axis (fast scanning axis) and y-axis (slow scanning axis) were computed. After adjusting the fitting parameters for optimal fit and checking the RICS map, the values for diffusion coefficient, number of particles and beamwaist where obtained.

The straight forward analysis procedure could not be followed for NPs in gels because of a less homogenous sample characteristic with particles diffusing at very different rates within the same region of interest. A smaller selection of interest for analysis of NPs in gel was therefore necessary. The regions of seemingly immobile particles were selected and analyzed in the first frame, and regions of mobile particles were selected and analyzed in frames throughout the sequence of imaging, if found. Examples of analyxing procedures can be found in Appendix C.

4. Results

In this chapter, the results from the project will be presented in four main sections. All experiments were performed with the two NPs, polystyrene (*P*) and Targ-233 (*T*) , with different surface modifications and zeta potential to be able to see how their characteristics influence the result and what characteristics are important for a potential increase in collagen penetration.

First the result from diffusion coefficient analysis of the polystyrene particles in water and in collagen are presented.

In the following section, the US transducers characterization is presented.

The main section includes the results from 5MHz US exposure of collagen droplets and qualitative characterization of the collagen fibers. The setup was modified and optimized continuously, other models with different NP concentrations and different US exposures were tried out in the first few months. This information is summarized in *Establishment of method* in Appendix E. The analysis procedure of the data was approached in various ways, because this experimental setup is new and an established analysis is not available.

4.1 The behavior of the NPs in water and in collagen gel

The two NPs have different surface modifications that can lead to different interactions in various medium. The diffusion of the two particles were measured with RICS in both water/PBS and in collagen gel. The results for Targ-233 are from my project thesis [61], and is reprinted here for comparison.

4.1.1 Diffusion in water

The result of RICS analysis of diffusion coefficients (D) in water for the two NPs are shown in Figure 4.2 a) plotted on a log scale. The result is based on 53 measurements of D for polystyrene and 33 for Targ-233 in one experiment for each particle. The mean and std are weighted by the number of particles for each measurement of D. Polystyrene has a diffusion coefficient of about 10.7 μ^2/s with a std of 5.8. Targ-233 has a diffusion coefficient of about 2.8 μ^2/s with a std of 1.3. These experimental results show a diffusion coefficient about 3.7 times larger for the polystyrene NP, which is about twice as high as you would expect from the relation between the NPs radiuses. Equation (ref th Mia), states that the relation between the radius of the two NPs theoretically should be inversely proportional to the relation between their diffusion coefficients, ($D_p/D_T=R_T/R_p$) = 1.7 Theoretical values calculated from Eintein-Stokes relation, Equation (ref Mia), gives a diffusion coefficient of 4.2 μ^2/s for polystyrene and 2.40 μ^2/s for Targ-233. The experimental result for Targ-233 is in good correlation to its theoretical value. The experimental result for

polystyrene is more than twice its theoretical estimate.

4.1.2 Diffusion of particles in collagen

The difference in distribution of polystyrene and Targ-233 in collagen gel is apparent from images taken from the gels before RICS analysis, as seen in Figure 4.1 a) and b). The collagen fibers in the images are obtained with the same settings and the reflection images of collagen is overlaid with the fluorescence from the NPs and are representative examples of NP distribution in collagen gels. The polystyrene beads have formed large aggregations, whereas Targ-233 is well distributed throughout the gel.
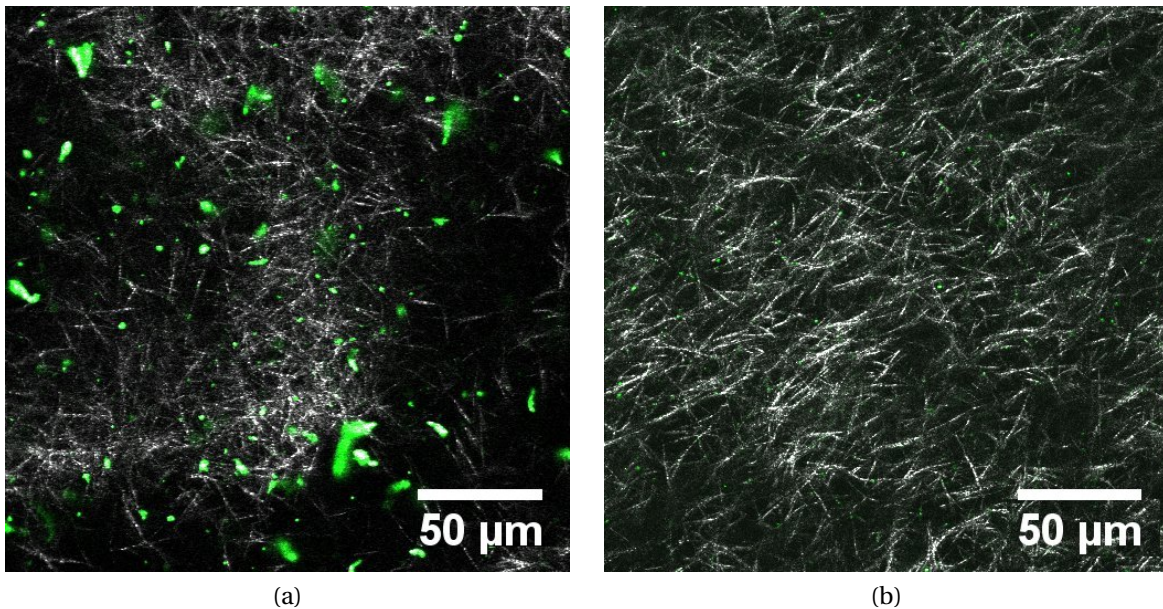

(a)   (b)

Figure 4.1: a) Polystyrene beads and b) polymeric nanoparticles in collagen gel (5 mg/mL).

The result of RICS analysis of diffusion coefficients in collagen gel for the two NPs are shown in Figure 4.2 b) plotted on a log scale. The mean D is weighted by number of particles measured for each D. In the analysis of Targ-233 done in my project thesis along with the analysis of five other PEGylated polymeric NPs, all particles showed a bi- or multimodal distribution of diffusion coefficients in collagen gels. This behavior, in addition to the seemingly freely diffusing particles in solution led to a division of particles into diffusion groups separated by more than two orders of magnitude in their diffusion coefficient; immobile NPs, intermediate NPs and mobile NPs:

Group 1 (Gr. 1): $D < 10^{-4} \mu m^2/s$: "Immobile" particles. These particles are virtually immobile and this group have a diffusion coefficient out of the range of accurate detection by the microscope and RICS analysis software.

Group 2 (Gr. 2): $10^{-4} \mu m^2/s \leq D < 10^{-1} \mu m^2/s$: Particles diffusing at "slow" speed, relative to the other particles. The slowest particles of this group are close to the limit of the speed the RICS software can detect accurately [26].

Group 3 (Gr. 3): $10^{-1} \mu m^2/s \geq D$: "Mobile" particles. All the particles in solution belong to this group, and these are considered the well diffusing particles.

This division into groups makes the calculation of mean diffusion coefficient for a population of particles more accurate. The mean values of D are based on data pooled from these three experiments, so the resulting std shows the variation within one group. The results show that the diffusion of polystyrene and Targ-233 in water is relatively homogeneous, with particles only within the range of the mobile diffusion group. Interestingly, the mobile population of Targ-233 in collagen gel has a diffusion coefficient on the same order of magnitude as in water. For the polystyrene bead, only a few measurements were possible to obtain of diffusing aggregates of NPs and all fall within the range of the intermediate diffusion group were detected in collagen gel, with D two orders of magnitude lower than in water. This is in correspondence to the overlaying images of collagen fibers and NPs in 4.1, where aggregates, not free particles are prominent.

By dividing D into groups, the difference between NPs will also be seen in how large the population is in each diffusion group. This fraction of particles is shown in Figure 4.2 c) on a linear scale. Data are based on one experiment repeated three times in new collagen gels each time for Targ-233. The mean values of fractions of particles are calculated for each experiment individually, and the resulting std shows the variation between experiments. The experiment for polystyrene was not repeated. The three populations of particles were represented in all experiments, however the fraction of them varied substantially between experiment repetitions, hence the large std error.

Diffusion of polystyrene and Targ-233 in water and in collagen gel
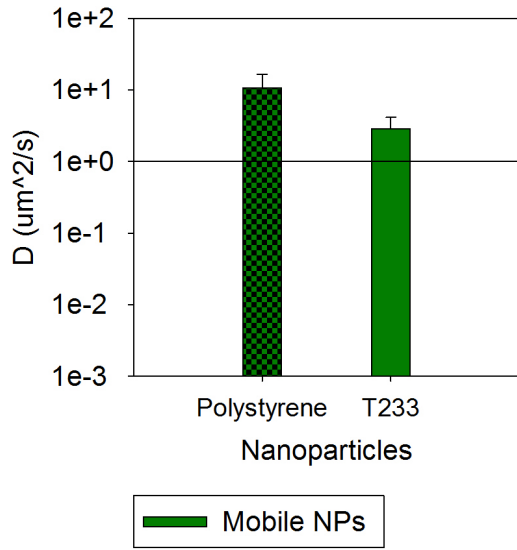
(a) Diffusion in water
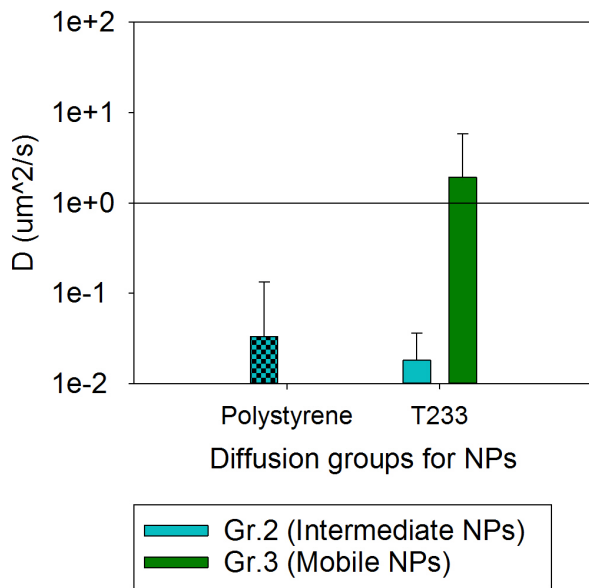
(b) Diffusion in collagen
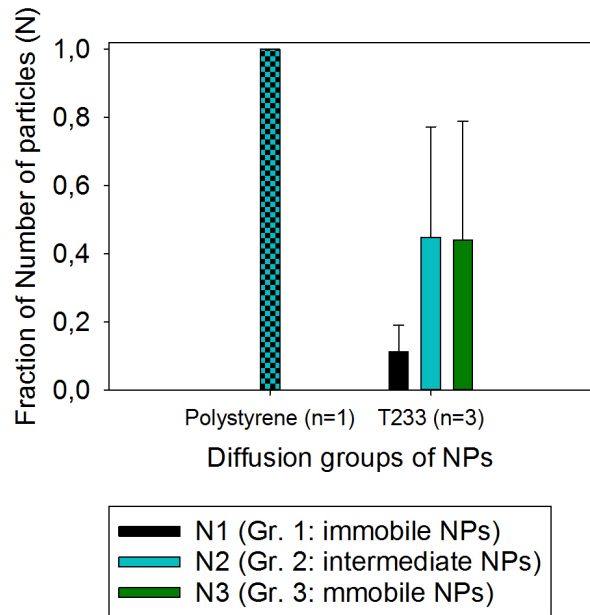
(c) Number fractions of particles in collagen

Figure 4.2: In a) the mean measured diffusion coefficient in water for both particles is plotted on a common log scale, along with the std for all analyzed particles in one experiment. In b) the diffusion coefficient of the two particles in collagen gel is shown. For Targ-233 the mean value and standard deviation are calculated based on pooled data from three experiment repetitions. The fraction of each diffusion group is shown in c) where the standard deviation for Targ-233 is a measure of uncertainty between experiment repetitions (n=3). The experiment with polystyrene was not repeated.

4.2 Characterization of FUS transducers

The main results from the characterization of the 5 and 10 MHz transducers in a water tank are summarized in Figure 4.3 and 4.4. The axis scans are presented in Figure 4.3 with pressure on a dB scale on the y-axis as a function of the distance from the transducer surface (z-axis) in mm. The pressure reaches its highest value (0dB) at about 70 mm from the transducer surface for the 5MHz transducer in a) and at about 50 mm distance from the transducer, both in accordance to the manufacturers data. Important to note, is that the pressure stays quite high before and after the focus, especially for the 5MHz, allowing for reasonable alignment offsets along the z-axis in experimental setups. The -3 dB limit, indicates that the pressure here is halved relative to the highest pressure, found at the focus. To keep a pressure above half of maximum pressure (above -3dB) allows for an alignment offset from focus in the experimental setup of about +10, -20 mm for the 5 MHz transducer and $\pm$ 3.5 mm for the 10 MHz transducer.

In Figure 4.4 a) and b) the contour plots, again in pressure dB scale from the focus scan are presented for 5 and 10 MHz respectively. The first, inner ring in the contour plot, lies at the -3 dB limit. The beamwidth of the transducers at focus, with pressures above -3dB, can be read out as 1.2mm for the 5 MHz, and 0.45mm for the 10 MHz transducer, somewhat lower and higher respectively than the stated beam width from the manufacturer. In c) and d) the focus scans are presented as surface plots to illustrate the beam profile at focus. Within the centered focus area of the 5MHz transducer of 1.2x1.2mm^2, the pressure values for the 10MHz falls below -12 dB.

In Figure 4.4 e) and f), the absolute values of the peak negative pressures in Mega Pascals are plotted as a function of peak to peak amplitude in miliVolt from the signal generator. This voltage is amplified before it is sent to the transducer. The correlation between input voltage and output pressures from the transducer has a more linear regime for low amplitudes and flattens out for high ones, more so for 10 MHz in f) than for 5MHz in e). The last point for 1000 mV for 5Mhz is interpolated, with cubic polynomial regression (R^2=0.999) because it was not obtained during the characterization. Pressures generated with the 10 MHz transducer are in general higher than for the 5 MHz transducer for the same voltages applied.

(a) 5 MHz   (b) 10 MHz

Figure 4.3: Axis scans for 5 and 10 MHz.

(a) 5 MHz

(b) 10 MHz

(c) 5 MHz

(d) 10 MHz

(e) 5 MHz

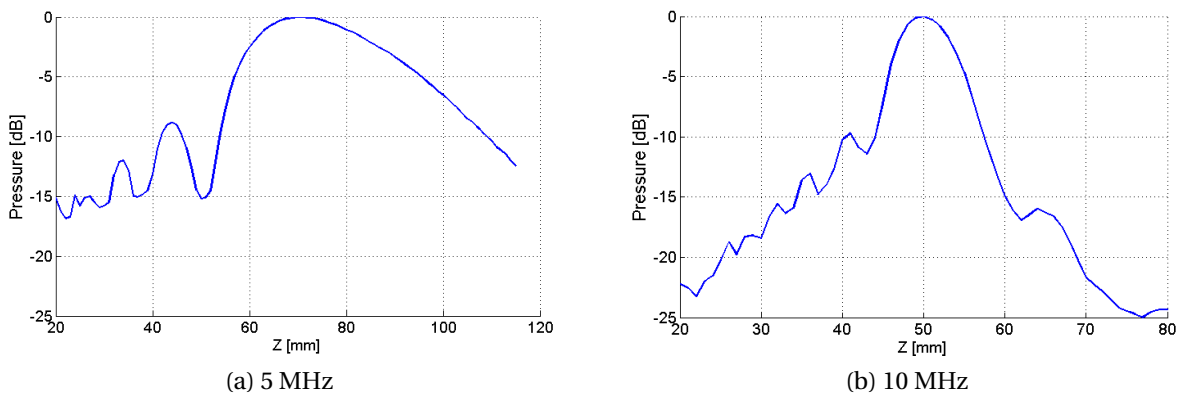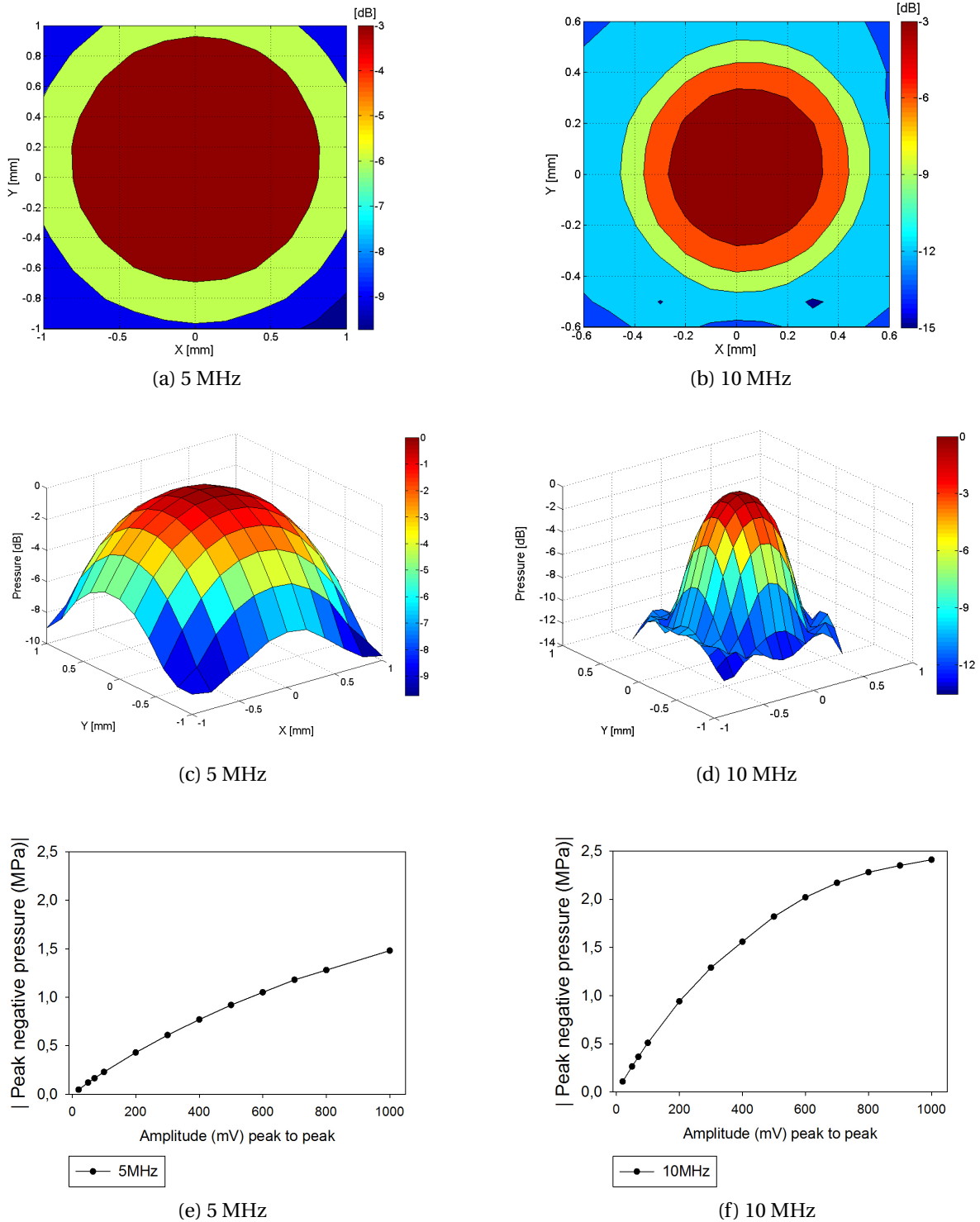(f) 10 MHz

Figure 4.4: Contour plots in a) and b), and surface plots in c) and d) showing the beam profile resulting from focus scans. e) and f) shows the correlation between applied voltage (from signalgenerator) and absolute values of peak negative pressure from the transducers.

4.3 US exposure of collagen droplets in NP solution

As seen from Figure 4.4, the beam width of the 5MHz transducer is larger than for the 10MHz, making the 5MHz more desirable to use to be more sure to expose the collagen droplets to one US exposure. Experiments with polystyrene and the Targ-233 NP were carried out in three treatment groups:

Control: Droplets were placed in US exposure setup between imaging, but did not receive US.

06VPP: Droplets received 5MHz US exposure with an amplitude 0.6V peak to peak.

1VPP: Droplets received 5MHz US exposure with an amplitude 1V peak to peak.

These experiments were repeated two times for each particle, however, the data for each group are not pooled in later analysis because of large variations within each group. While analyzing the images, it was apparent that there were microscope scanning error in some of the images, showing up as stripes or squares of added intensity, as seen in Appendix D. This scanning error would show up to varying degrees throughout an image, and throughout the run of an experiment. This added fluorescence to the images randomly and in some images more than others, largely affecting the result. Especially in one experiment (T06V1), the data should be disregarded, because the pre image has more error than real values. For the other experiments, most of the scanning error might have been excluded in the thresholding done in later image analysis. The error most likely originate from the HyD detector used. Therefore one more experiment with Targ-233 was carried out in each treatment group with PMT detectors to make it easier to verify and discuss any possible trend seen from the results ($PMTT$).

4.3.1 Characterization of collagen fibers

The degree of accumulation of NPs on the collagen surface is likely dependent on the NP characteristic as well as to the polymerization of the collagen. The same concentration of collagen was used in all experiments and was made following the same procedure. However, small variations in fiber length, fiber volume fraction and intensity overall is visible in images, that is likely to influence the interaction with NPs differently in every experiment. The intensity in a collagen reflection image is correlated to the density of collagen, and the structure of it. A well polymerized gel in a hydrated environment would have a greater intensity than a poorly polymerized gel of the same concentration in a less hydrated environment.

In addition to the tilescan images from each drop, higher resolution images were taken at three levels in the gel: at the surface, 100 microns under the surface and 100 microns above the well plate bottom, as seen in image series in Figure 4.5-4.6, for two different treatment groups. Only the reflection channel (white) is included in the image and images are acquired with same zoom (8.10) and settings with no image adjustments. The intensity increases with penetration into the collagen in both image series. The image of the fibers on the surface in Figure 4.6 a) appears to be of lower quality than the image from the surface in Figure 4.5. There could be reflection from an interface containing more air in this image.

One high resolution image from 100 microns under the surface, acquired with the same zoom and settings as above, but with brightness and contrast mutually enhanced, are included along with one image from each tilescan in Figure 4.7-4.11. The tilscan images are from about 20 microns under the collagen surface and with contrast and brightness mutually enhanced to a high level. There are large variations in intensity and fiber volume fraction between experiment repetitions at both 20 and 100 microns into the drop. Deeper into the drop, closer to the well plate and less affected by exposure to air, the fibers were of higher intensity for all collagen drops.
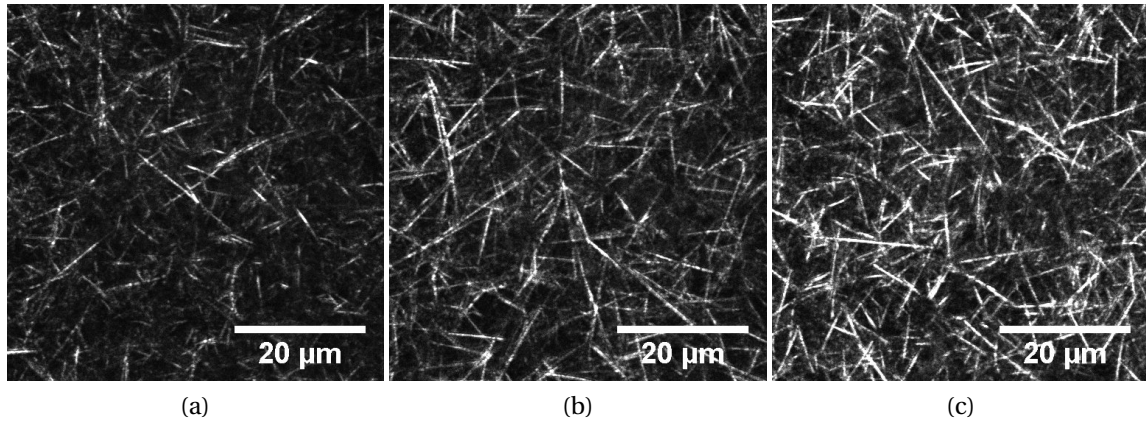
Figure 4.5: Collagen intensity increase as a function of penetration into the collagen droplet. Here for Targ-233 before 1VPP US exposure (T1V1), at a) the surface, b) 100 microns under the surface, c) 100 microns above well plate bottom.
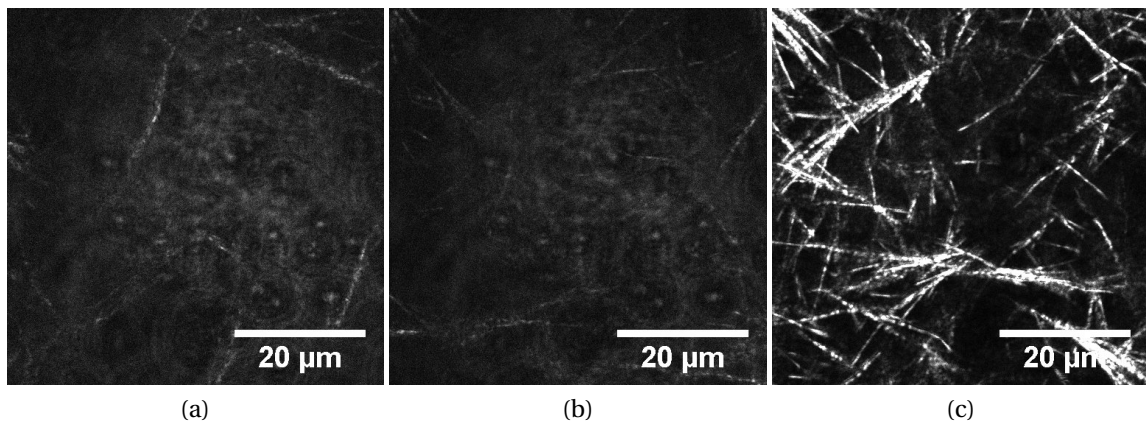
Figure 4.6: Collagen intensity increase with penetration into the collagen droplet. For Targ-233 and 0.6V US exposure (T06V1), the difference between fibers at the surface of the droplet, in a), 100 microns under in b), and 100 microns above the well plate bottom in c), is larger than for the fibers in Figure 4.5.

(a) PC1   (b) PC2

(c) P06V1   (d) P06V2

(e) P1V1   (f) P1V2

Figure 4.7: Collagen droplets used for experiments with polystyrene. a) and b) were used in control experiment 1 and 2. c) and d) were used for 0.6VPP US exposure experiment 1 and 2 and e) and f) were used for 1VPP US exposure experiment 1 and 2.

(a) PC1

(b) PC2

(c) P06V1

(d) P06V2

(e) P1V1

(f) P1V2
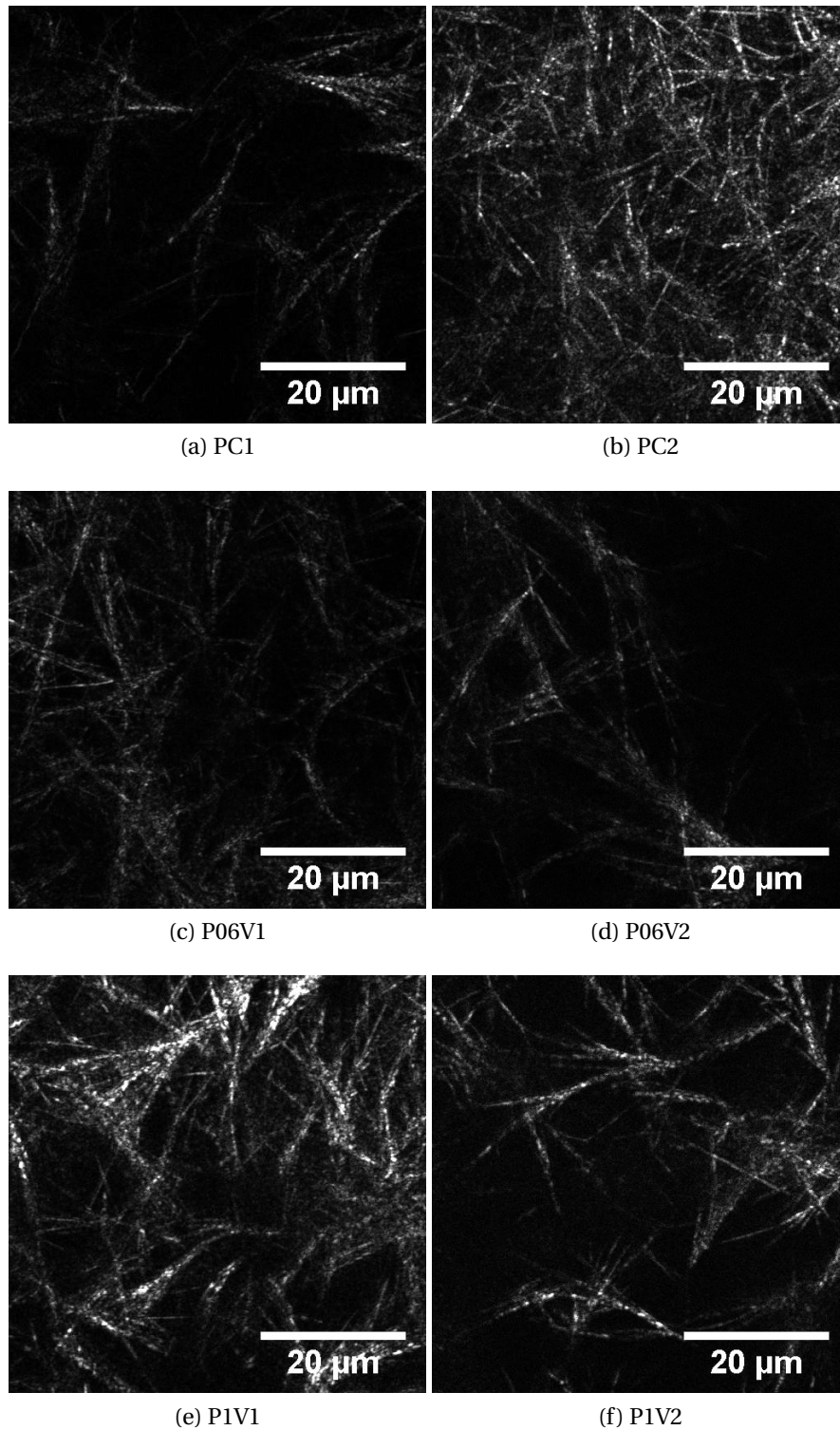
Figure 4.8: High resolution image of collagen fibers in droplets used for experiments with polystyrene. a) and b) were used in control experiment 1 and 2. c) and d) were used for 0.6VPP US exposure experiment 1 and 2 and e) and f) were used for 1VPP US exposure experiment 1 and 2.

(a) TC1   (b) TC2

(c) T06V1   (d) T06V2

(e) T1V1   (f) T1V2
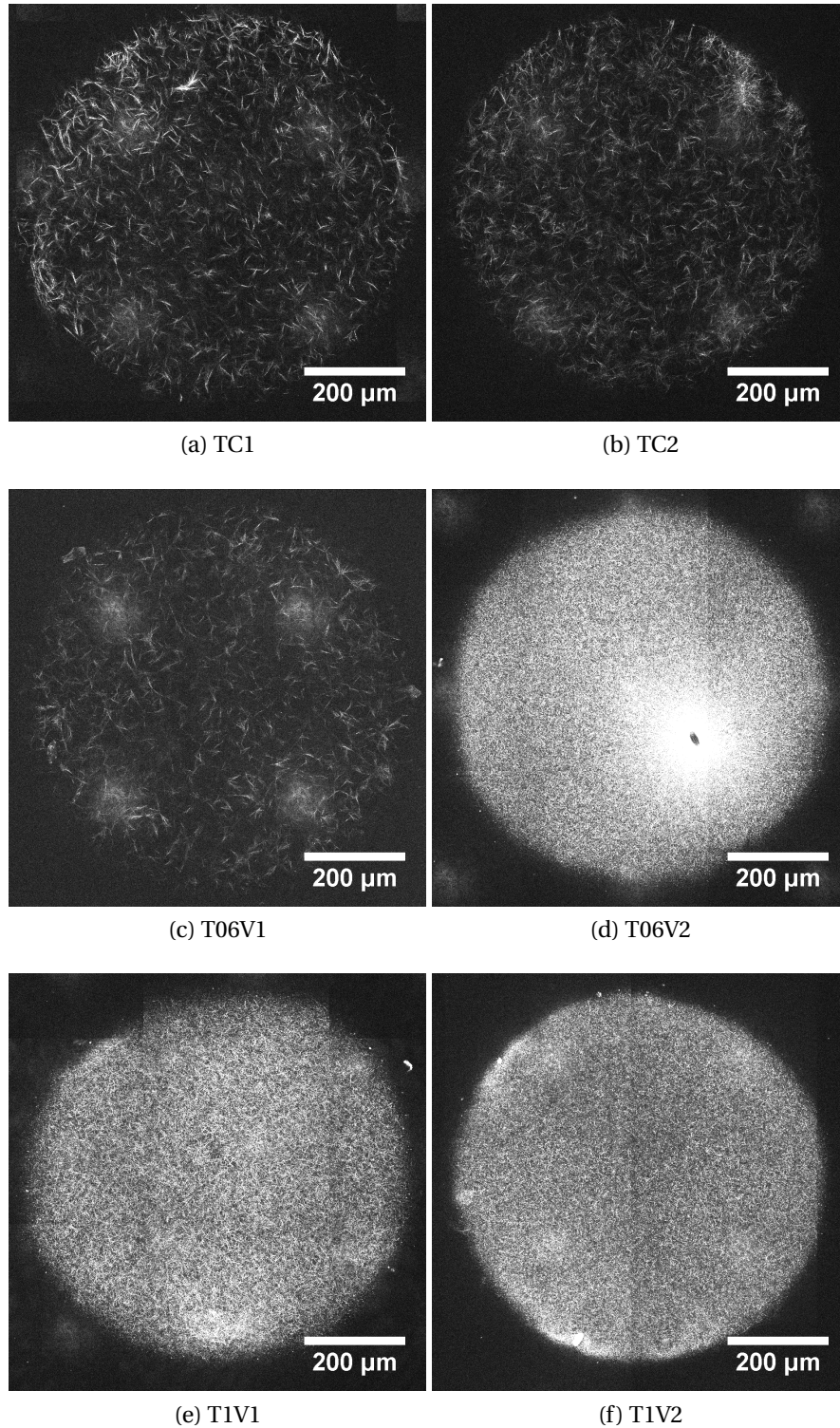
Figure 4.9: Collagen droplets used for experiments with Targ-233. a) and b) were used in control experiment 1 and 2. c) and d) were used for 0.6VPP US exposure experiment 1 and 2 and e) and f) were used for 1VPP US exposure experiment 1 and 2.
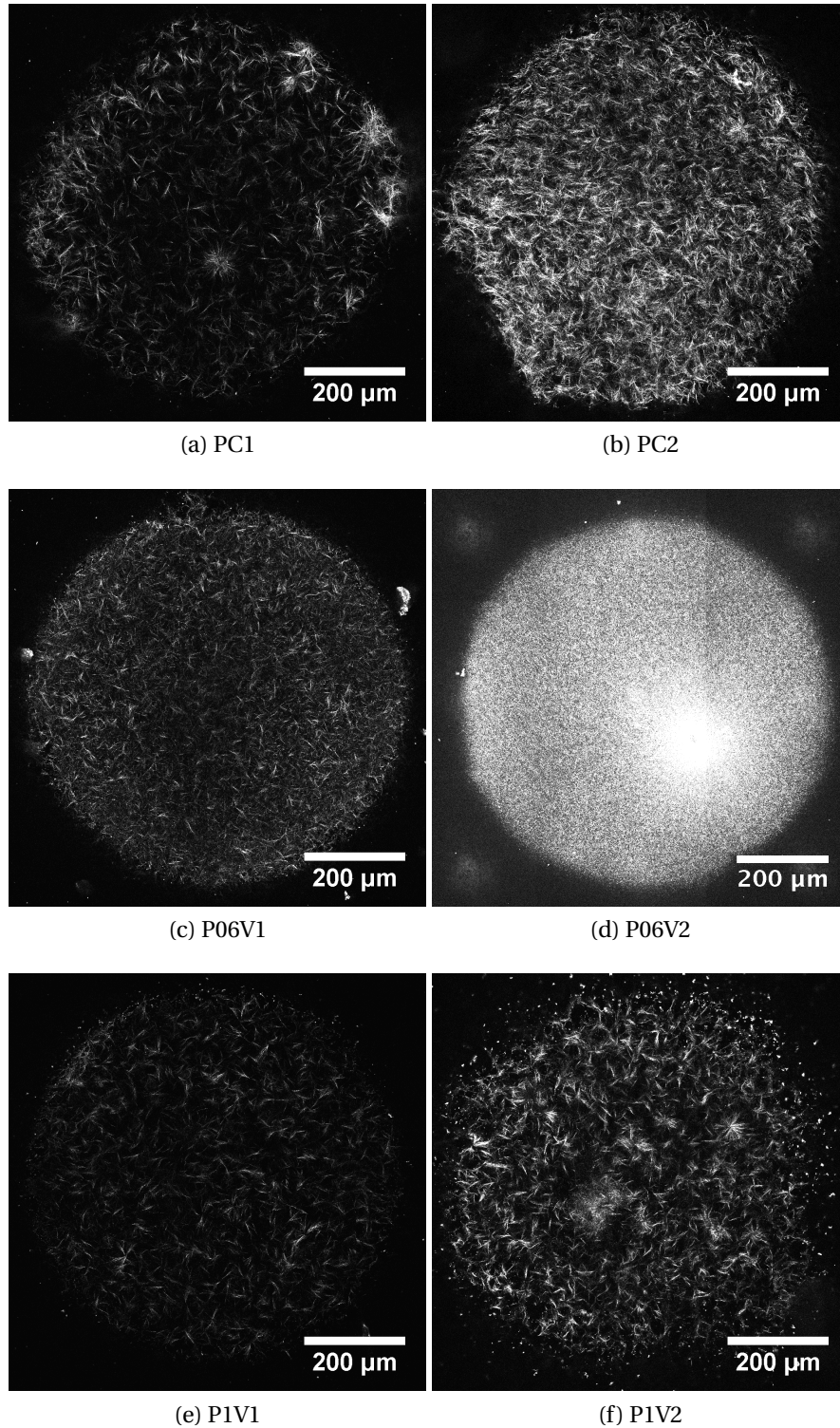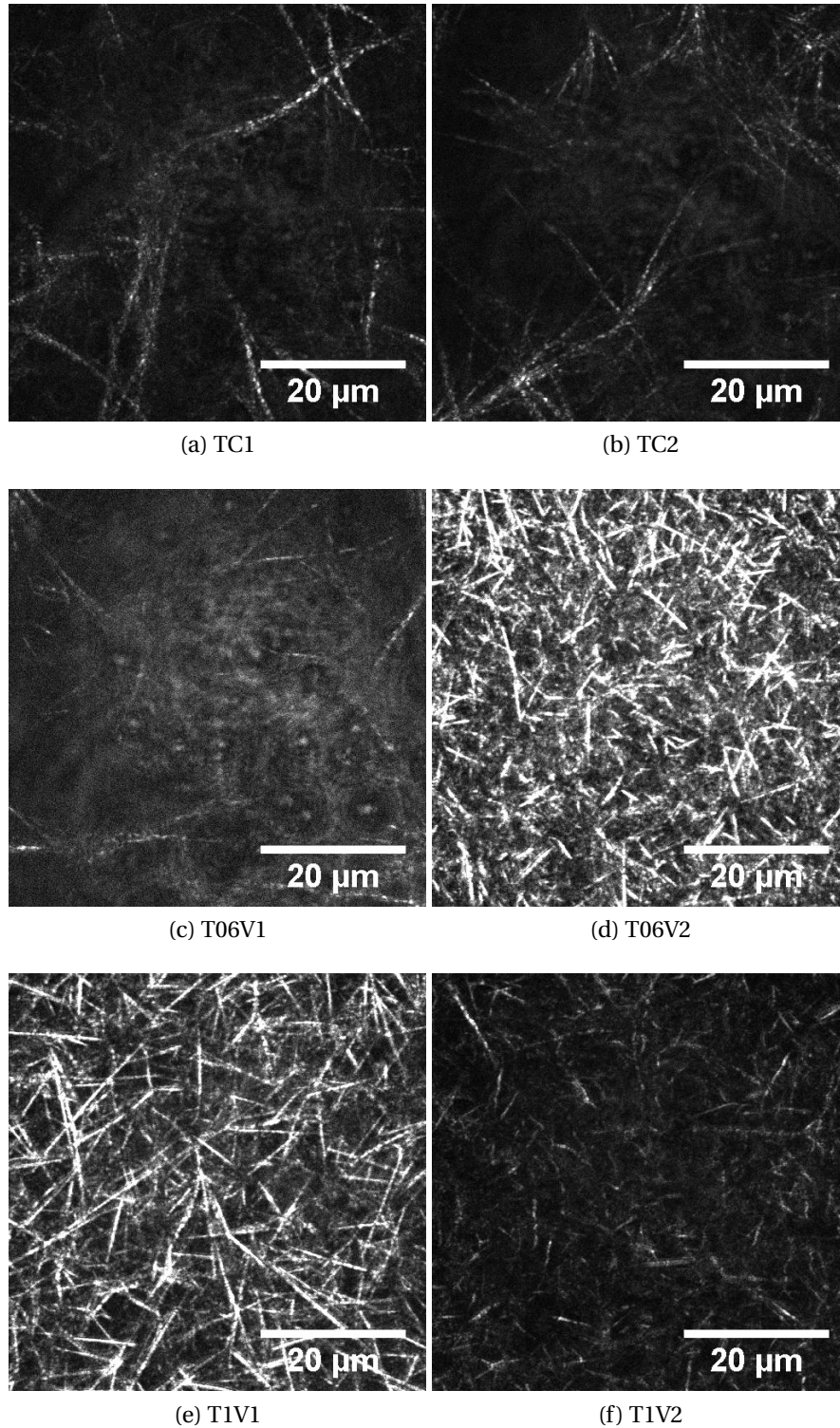
Figure 4.10: Collagen fibers in droplets used for experiments with Targ-233. a) and b) were used in control experiment 1 and 2. c) and d) were used for 0.6VPP US exposure experiment 1 and 2 and e) and f) were used for 1VPP US exposure experiment 1 and 2.

(a) PMTTC

(b) PMTTC

(c) PMTT06V

(d) PMTT06V

(e) PMTTC

(f) PMT1V1

Figure 4.11: Collagen fibers in droplets used for experiments with Targ-233 and PMT detectors. a) and b) was used in the control experiment. c) and d) was used for 0.6VPP US exposure and e) and f) was used for 1VPP US exposure.

4.3.2   Accumulation of NPs on the collagen surface
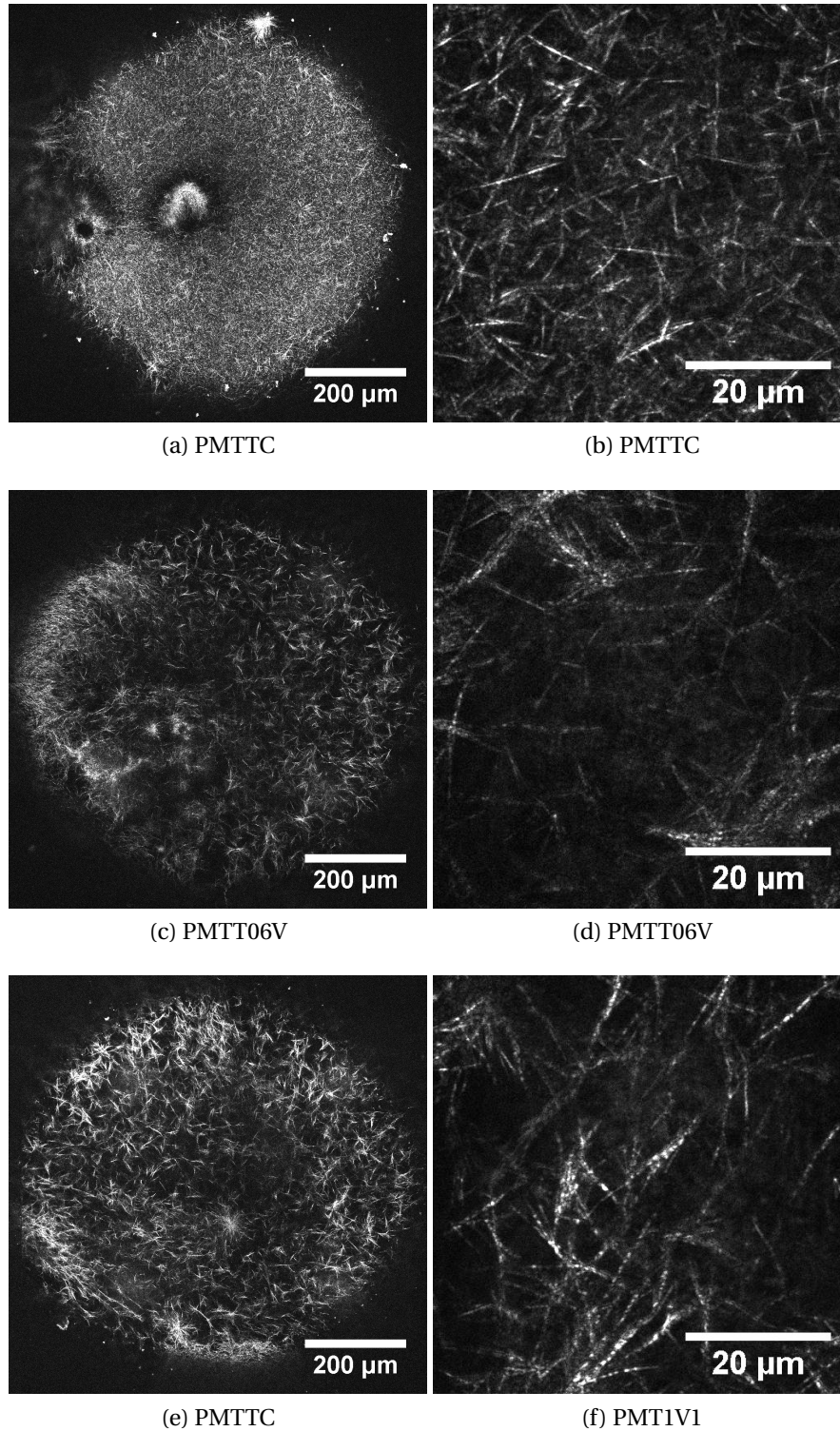
Both NPs accumulated to a large, but varying degree on the collagen surface before the pre image was obtained. The variability in the fiber polymerization as discussed above, is likely to influence both the accumulation before US exposure or control, but also the accumulation of the fibers as a result of US exposure.

In Figure 4.12-4.14, an image from the pre and post tilescans are shown for a control experiment and a 1VPP US exposure for polystyrene, Targ-233 and PMT Targ-233 respectively. The 0.6VPP exposure is also included for PMT Targ-233. The image is taken from a few microns under the very surface of the droplet, and contain both the reflection (white) and fluorescence channel (green), both with brightness and contrast adjusted to the same high level for polystyrene and Targ-233. All PMT Targ-233 images were adjusted different from the this, but to the same high level for all images.

A large accumulation of polystyrene is seen on the collagen fibers in Figure 4.12, and the NPs are covering the fibers completely. The difference in intensity from pre to post image seems to be less for the control in a) to b), than for the US treated droplet in c) to d). Also the degree of aggregation seems to be larger in the US exposed droplet. In the US treated droplet in d), aggregations out of focus are seen outside the periphery of the droplet. These aggregations most likely originate from the collagen surface in a section further down into the droplet, but the aperture of the microscope did not succeed in closing this light out.

The intensity in the images arising from Targ-233, are much lower than for polystyrene, as seen in Figure 4.13. The NPs are distributed among the fibers in the image and are not covering them as for polystyrene. There are smaller aggregations, relative to polystyrene, in both the post image in the control as for the US exposed droplet.

The images in Figure 4.14, show Targ-233 detected with the PMT detector. Targ-233 is well distributed among the collagen fibers relative to polystyrene. However, aggregations can be seen, especially for the control drop both in the pre and post image in a) and b). One large aggregation can be seen on the collagen surface in d) post US exposure.

(a) PC1 pre

(b) PC1 post

(c) P1V2 pre

(d) P1V2 post

Figure 4.12: Images from a under the collagen droplet surface. Collagen is seen in white with CRM, the FS from the NPs in green. a) and b) shows a pre and post control image respectively. In c) and d), an image pre and post 1VPP US exposure is shown.

(a) TC2 pre   (b) TC2 post

(c) T1V2 pre   (d) T1V2 post

Figure 4.13: Images from under the collagen droplet surface. Collagen is seen in white with CRM, FS from the NPs in green. a) and b) shows a pre and post control image respectively. In c) and d), an image pre and post 1VPP US exposure is shown.

(a) PMT TC pre

(b) PMT TC post

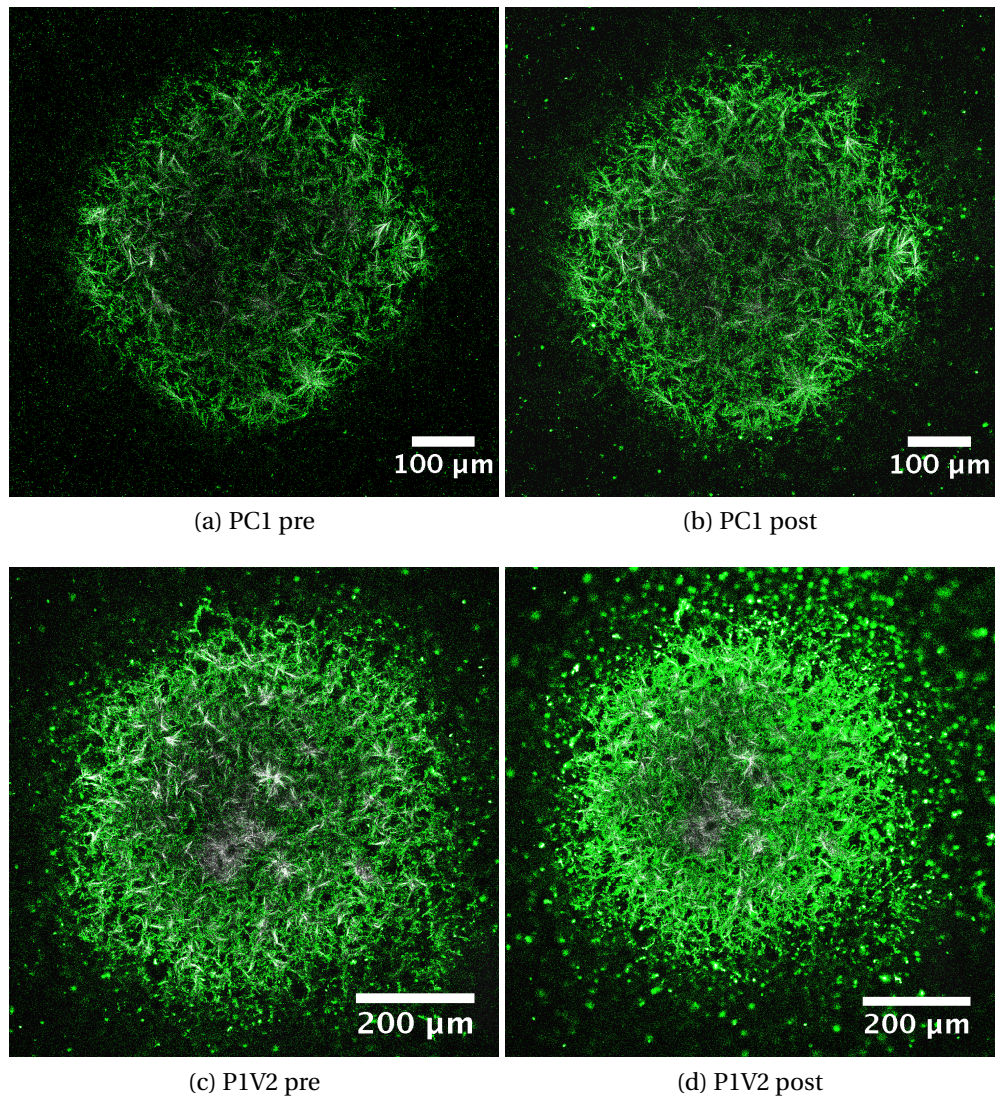(c) PMT T06V pre
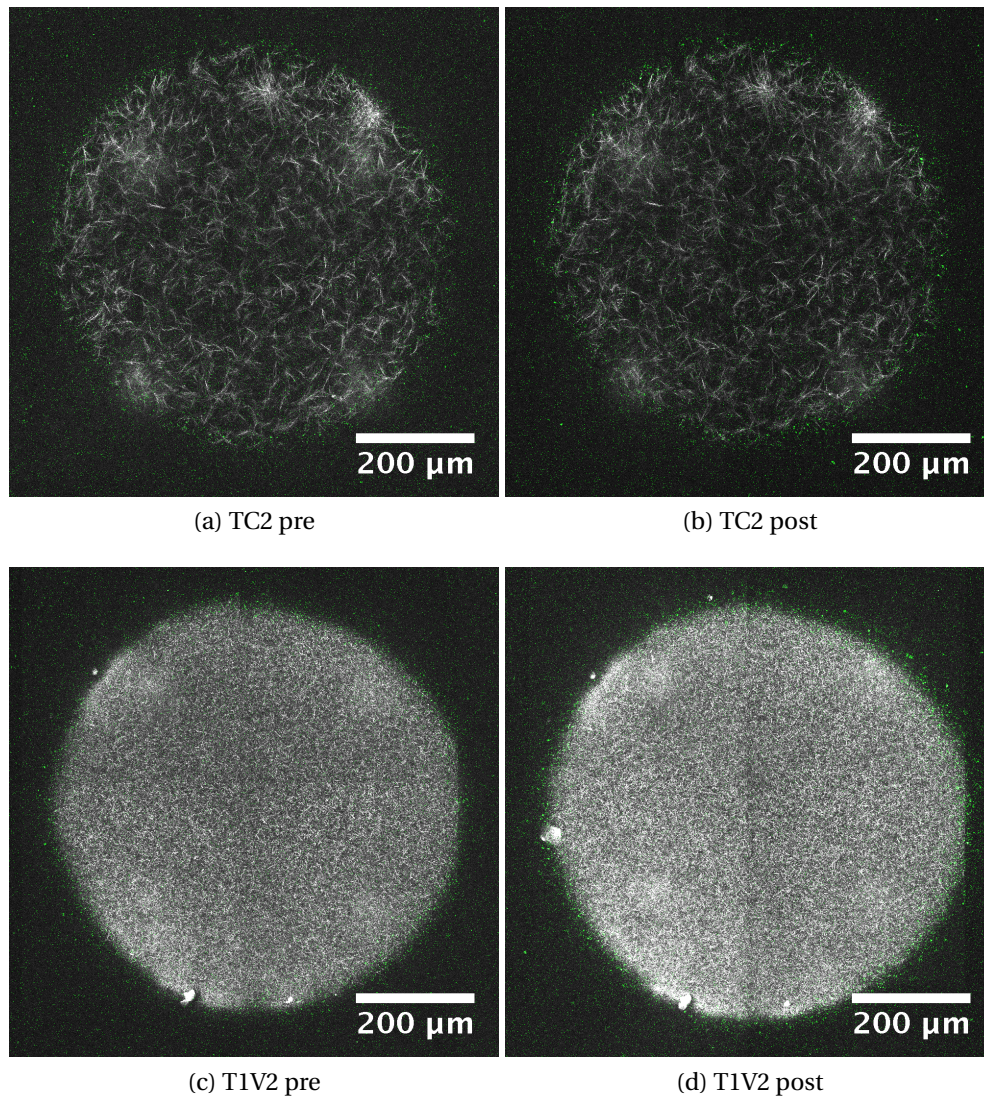
(d) PMT T06V post
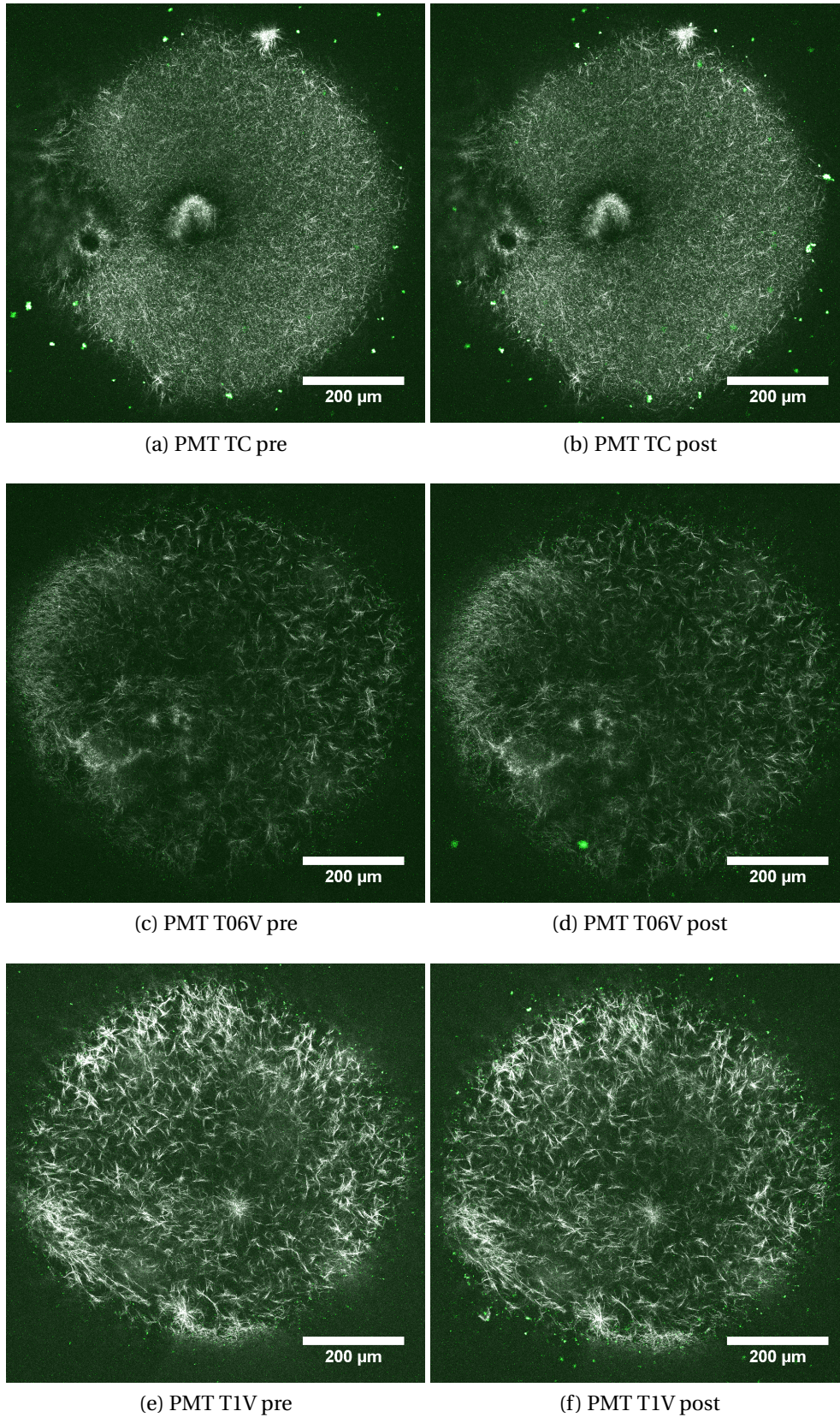
(e) PMT T1V pre

(f) PMT T1V post

Figure 4.14: Images from under the collagen droplet surface. Collagen is seen in white with CRM, FS from the NPs in green. a) and b) show a pre and post control image. In c) and d), an image pre and post 0.6VPP US is shown. e) and f) show pre and post 1VPP US exposure.

4.4 Penetration of NPs into collagen gel

As described in section 3.6.1, further analysis of the intensity change in th ecollagen are based on a circular selection centered relative to the collagen droplet in each tilescan. Across this centered area with a diameter similar to the FUS beamwidth, the intensity of NPs are plotted as a function of penetration depth starting about 30 microns above the collagen surface and continued about 90 microns into the gel, shown for the different particles in Figure 4.15-4.17. The blue plot is the pre US exposure values, and the green plot is post US. The values are normalized to the max pre US intensity to account for the differences in pre US accumulation that might arise.

A prominent peak is apparent in all plots. The max value of intensity is assumed to originate from the collagen surface, or the interface between the NP solution and the collagen. This is verified from inspection of images of collagen overlaid with the fluorescence channel. As explained in section 3.6.1, and seen in Figure 4.12 d), the microscope pinhole might not close out all light originating from large aggregations of NPs from sections out of focus, and fluorescence might "leak" into sections around the the surface. The max value of intensity is regarded as the surface accumulation in later analysis.

The region after the peak, when the intensity of the pre US peak has reached 5 % for polystyrene and Targ-233 or 25 % for PMT Targ-233, is regarded as being inside the drop, not affected by the "leakage" of fluorescence from the surface.

Symmetrically, in the front of the peak, this region before the 5- and 25-%-limits as explained above, is regarded as being above the collagen surface.

There are large variations between experiments and overall the post US intensity values are substantially larger than the pre values. The only exception is T06V1, where the pre image is largely affected by scanning error as explained above in section 4.3, and should be disregarded. The result is included to show how the scanning error could affect the results. In addition the post intensity values can still give valuable information in later analysis. The largest changes pre to post US in intensity is found for the highest amplitude US treatment for both polystyrene and Targ-233 in Figure 4.15 e) and Figure 4.16 e), respectively. However, some of the control experiments have a seemingly larger change in intensity pre to post that some of the US treated drops.

The plots for PMT Targ-233 in Figure 4.17, all show higher intensity values post US relative to pre US. For the 0.6VPP US exposure, two plots are shown from the same experiment, in b) and c). The plot in b) is replotted in c) with values from one ROI excluded. This ROI contained very high intensity values originating from aggregations on the surface. By excluding it, it is possible to see if that affects the values in front of and after the peak.

Intensity as a function of penetration into collagen drop: Pre (blue) and US (green) control or US treatment for Polystyrene

Figure 4.15: Intensity Pre and Post US and control normalized to Pre max intensity are plotted against penetration depth in microns, starting from in front of collagen surface until end of imaging. Treatments are indicated in each subtitle. All figures are plotted with the same axis scales, except Figure f) (P1V2).

Intensity as a function of penetration into collagen drop: Pre (blue) and US (green) control or US treatment for Targ-233

Figure 4.16: Intensity Pre and Post US and control normalized to Pre max intensity, plotted against penetration depth from in front of collagen surface until end of imaging. Treatments are indicated in each subtitle. All figures are plotted with the same axis scales.

Intensity as a function of penetration into collagen drop: Pre (blue) and US (green) control or US treatment for PMT Targ-233
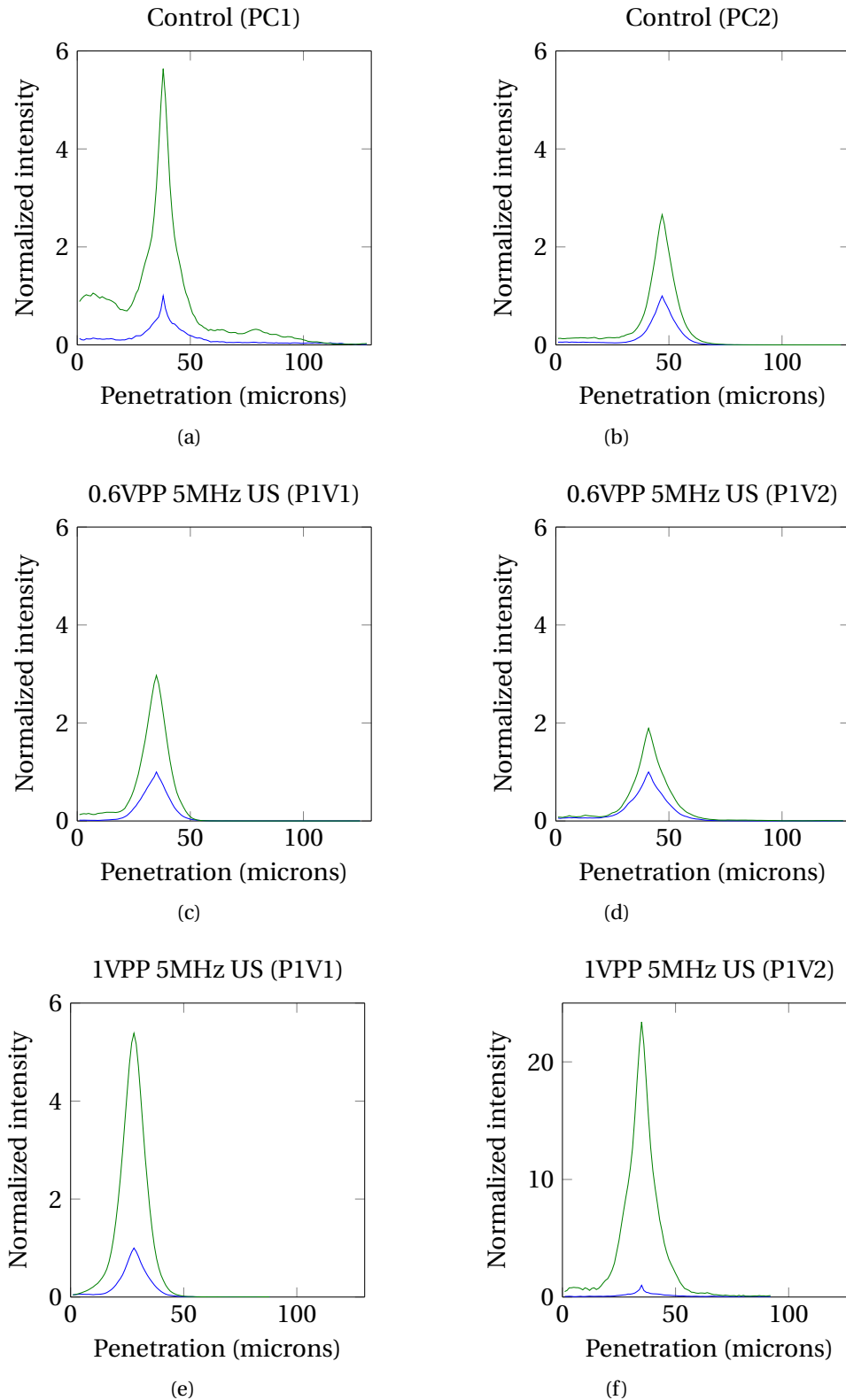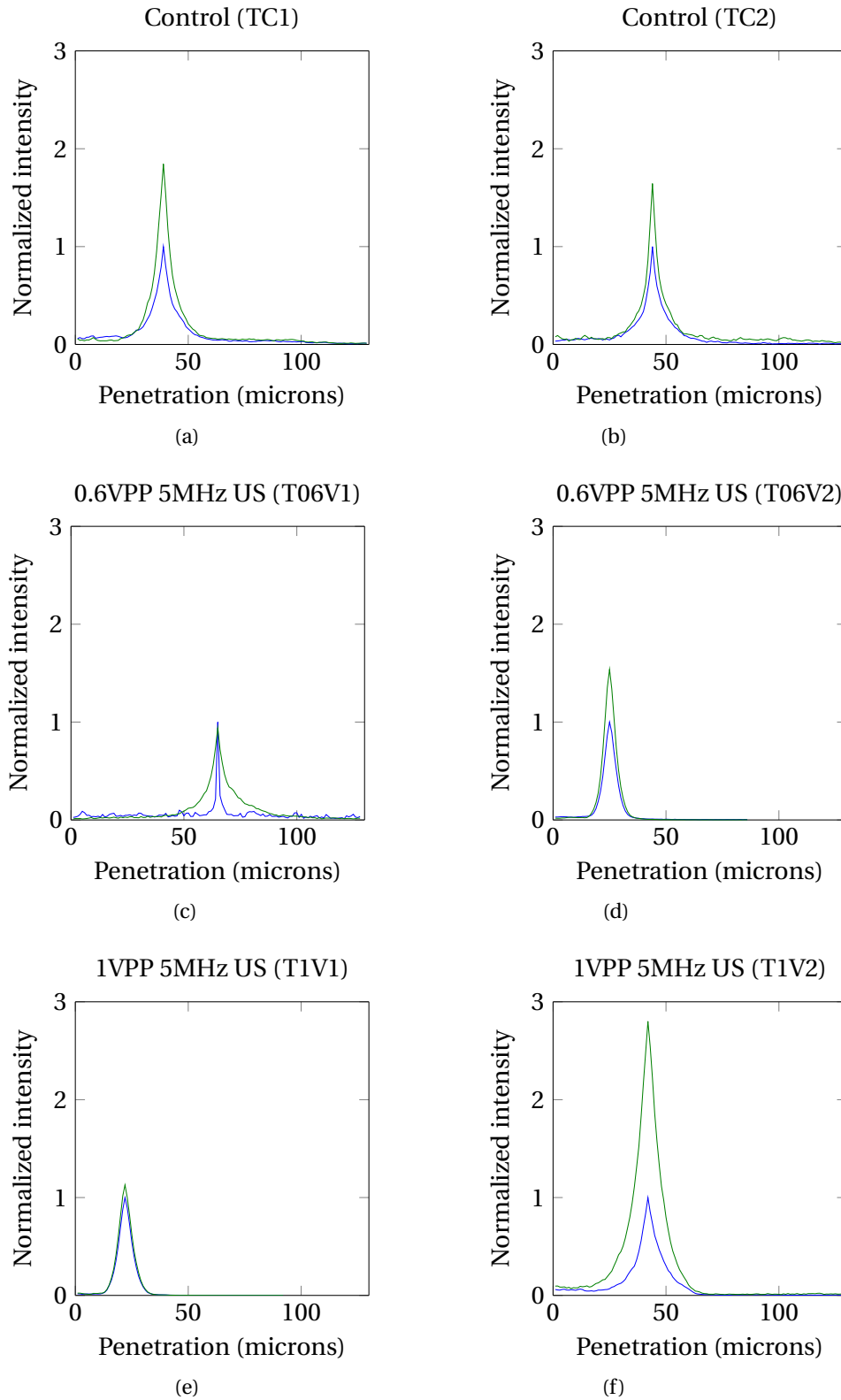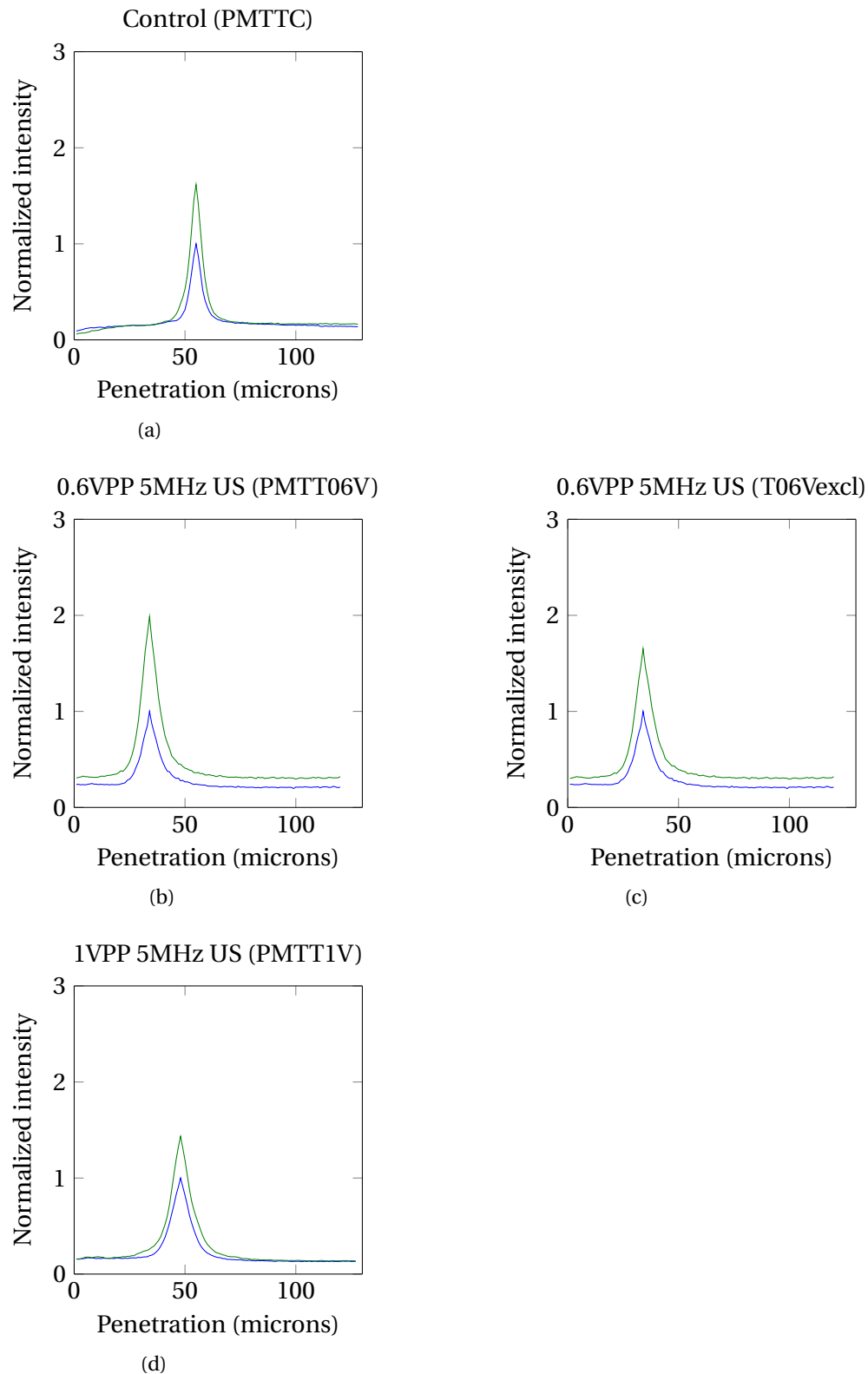

Figure 4.17: Intensity Pre and Post US and control normalized to Pre max intensity, plotted against penetration depth from in front of collagen surface until end of imaging. Treatments are indicated in each subtitle. All figures are plotted with the same axis scales. n=1 for all treatments, but two values were excluded for PMTT06V, hence two figures for this treatment.

4.4.1 Distribution of surface accumulation

To visualize the change in and distribution of NP accumulation on the surface, the max intensity value in the pre US image, is subtracted from the max intensity value in the post image. These plots are not normalized, to visualize the absolute increase in intensity on the surface. Most plots are plotted on the same axis to emphasize the difference between treatments. Because these plots show the absolute NP accumulation, the results can be correlated to both treatment effects as well as NP interactions with collagen of various polymerization. Note that each colormap is different. The accumulation is visualized in surface plots in Figure 4.18 for Polystyrene, in Figure 4.19 for Targ-233 and in Figure 4.20 for the experiment done with Targ-233 with the PMT detector. The surface plots are from the selected centered region from every tilescan that are used in further analysis.

The values seen in the surface plots for polystyrene in Figure 4.18 are positive, implying an accumulation of NPs on the surface in all treatments pre to post image. The one exception for P06V2, might arise from an alignment offset of the pre and post US image. The three US exposed drops in c), e) and f) show a large accumulation of particles, relative to the controls, in ROIs relatively symmetric around the max value. The largest accumulation is seen for the highest amplitude US exposure.

For Targ-233 in Figure 4.19, a very similar interpretation can be done: most plots show an accumulation of NPs. The US treated drops in d) and f) show the higher accumulation at regions relatively symmetric around the max value.

The results for PMT Targ-233 show an opposite result, with more NP accumulation in the control than in the US treated drops. One high value, originating from aggregation of NPs on the surface, seen in Figure 4.14 d), is excluded for the plot for PMTT06V, to visualize variations in the rest of the surface (PMT06Vexcl).

The large variations in surface accumulation among all the controls can be seen in relation to the collagen fiber intensity in Figure 4.5-4.6. Qualitative inspections suggest that PMT TC has the highest fiber intensity, followed by PC2. The other controls have lower fiber intensity. These experiments also show a higher NP surface accumulation. Of the US treated droplets, P06V2, P1V1, T06V2, T1V1, T1V2 are composed of collagen fibers of higher intensity than the rest of the US treated droplets, and have the highest NP surface accumulation.

Surface plots of Change in Max Surface Intensity Between Pre and Post US or control for Polystyrene

Figure 4.18: Surface plots of Max intensity difference between Pre and Post US and control plotted against X and Y coordinates in microns in a centered selection of the collagen drops. Treatments are indicated in each subtitle. All figures have individual colormaps, but the same z-axis except Figure e) (P1V1).

Surface plots of Change in Max Surface Intensity Between Pre and Post US or control for Targ-233

Figure 4.19: Surface plots of Max intensity difference between Pre and Post US and control plotted against X and Y coordinates in microns in a centered selection of the collagen drops. Treatments are indicated in each subtitle. All figures have individual colormaps, but the same z-axis.

Surface plots of Change in Max Surface Intensity Between Pre and Post US or
control for Targ-233 with PMT detector
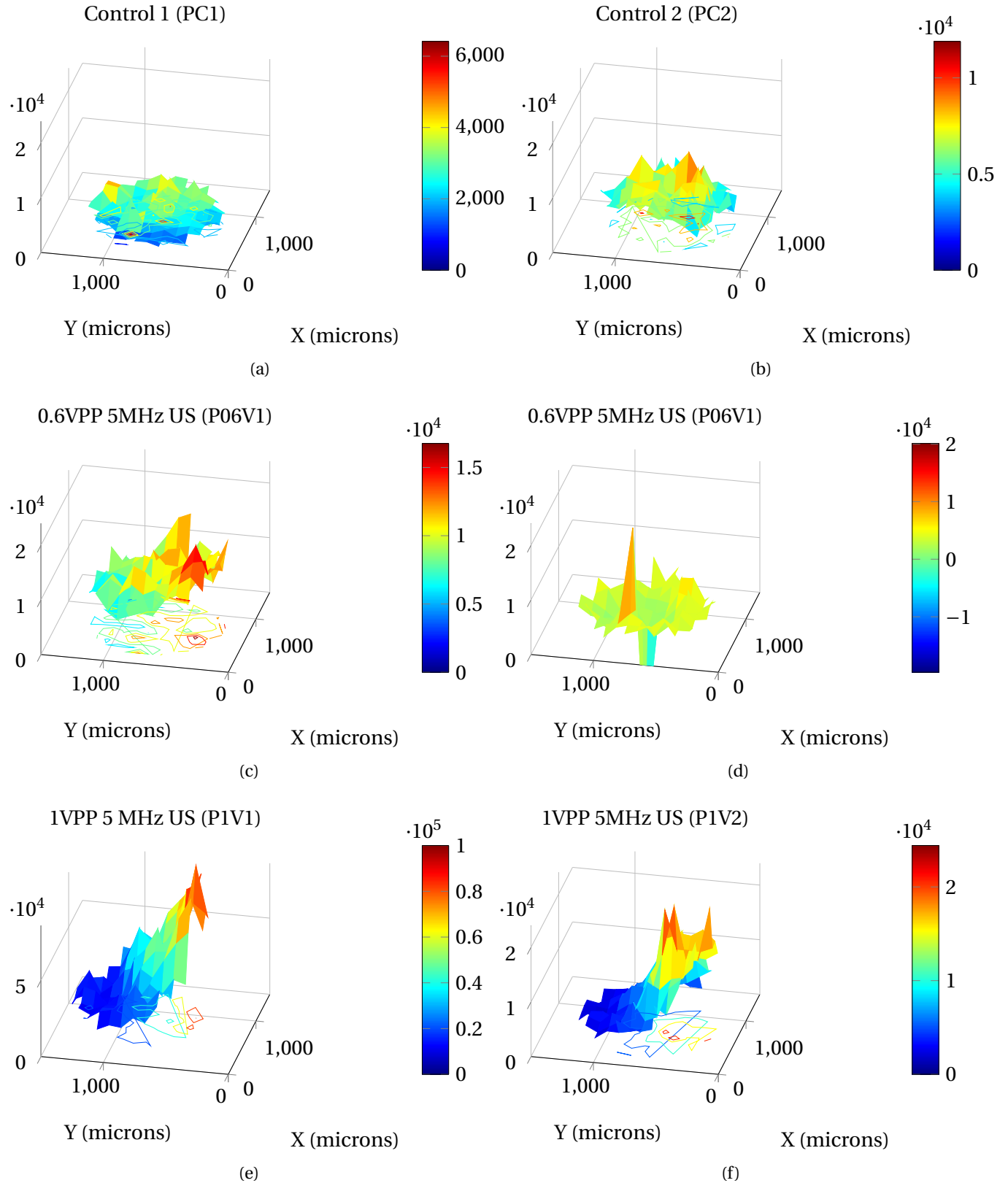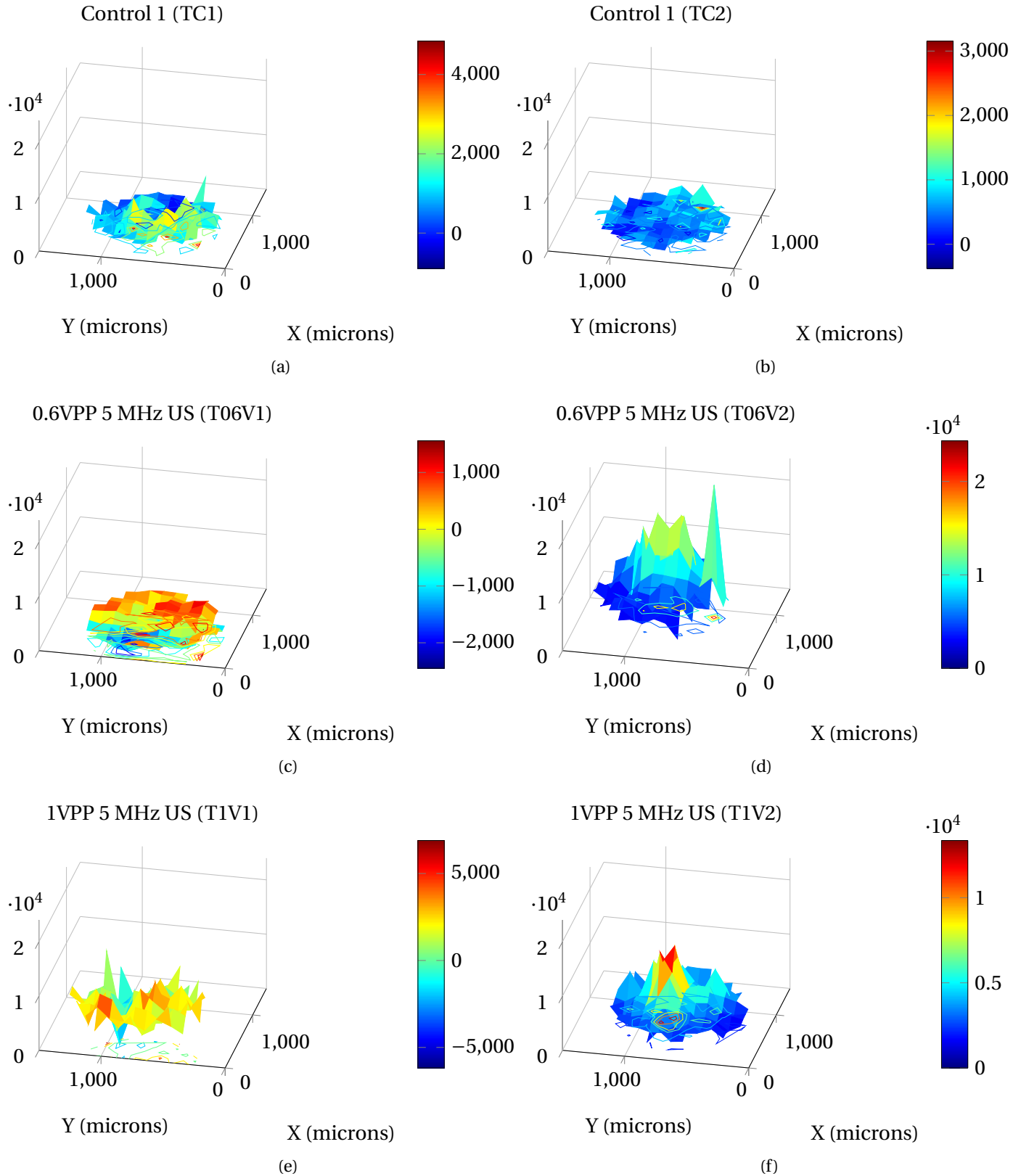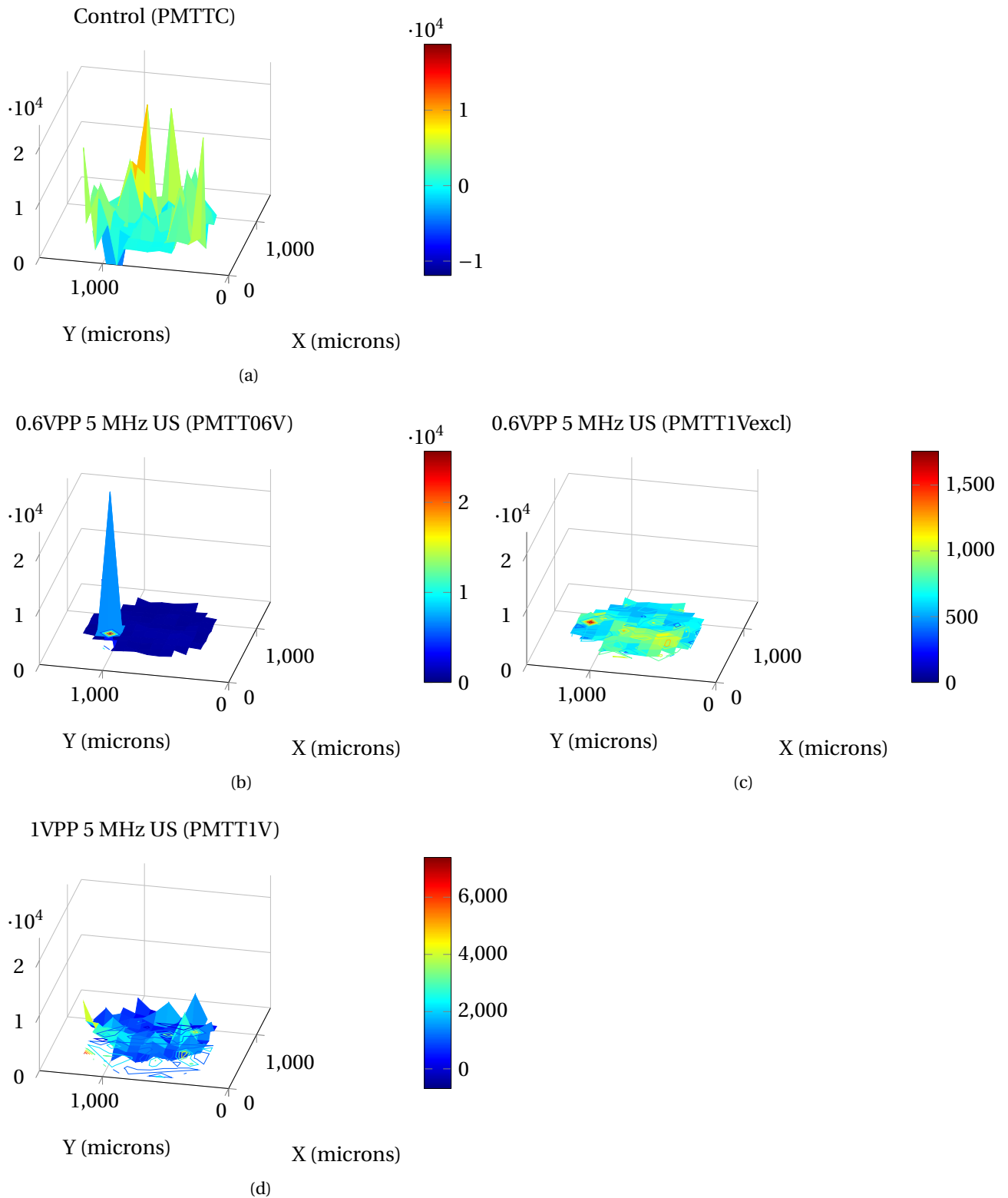

Figure 4.20: Surface plots of Max intensity difference between Pre and Post US and control plotted against X and Y coordinates in microns in a centered selection of the collagen drops. Treatments are indicated in each subtitle. All figures have individual colormaps, but the same z-axis. n=1 for all treatments, but two values were excluded for PMTT06V, hence two figures for this treatment.

4.4.2 Relative change in surface accumulation

The absolute max intensity values post US were normalized to pre US values to calculate the relative change in surface accumulation. These values are plotted on a common log scale in Figure 4.21 a) and b) for both particles.

Disregarding the experiment with scanning error, T06V1, all treatments had a positive surface accumulation for polystyrene and Targ-233. The accumulation of polystyrene is larger than for Targ-233, and especially one treatment has a substantially larger accumulation than the others. P1V2 has above 20 times larger intensity post US relative to pre US accumulation, more than three times the accumulation in the largest control. Looking closer at the obtained data, it came clear that the collagen droplet was pre imaged twice. During the first preimage, the water drop on the objective lens dried and a new pre image was obtained. The time between pre and post image analyzed here is the same as for the others, however the pre accumulation was allowed to happen for a longer time.

The accumulation in the controls are overall higher than for the lower amplitude US exposure for Targ-233. The higher amplitude US exposure has the largest accumulation in one experiment, yet the largest variation between experiment repetitions. The two controls for Targ-233, have a higher accumulation than the lowest 1VPP US treated droplet.

The experiment done with Targ-233 and a PMT detector shows very little difference between treatment groups. The 0.6VPP exposure shows a slightly higher surface accumulation. From image inspection of the PMT06VPP in Figure 4.14 d), in addition to surface plots above in Figure 4.20 b) and c), it is apparent that there is high intensity from one large aggregation on the surface. When this one high value is excluded in Figure 4.17 b) to c), the surface accumulation is substantially lowered. Therefore the small increase in surface accumulation seen for 0.6V PP exposure, and possibly for the other experiments, does not necessarily arise from an even distribution of NPs on the surface.
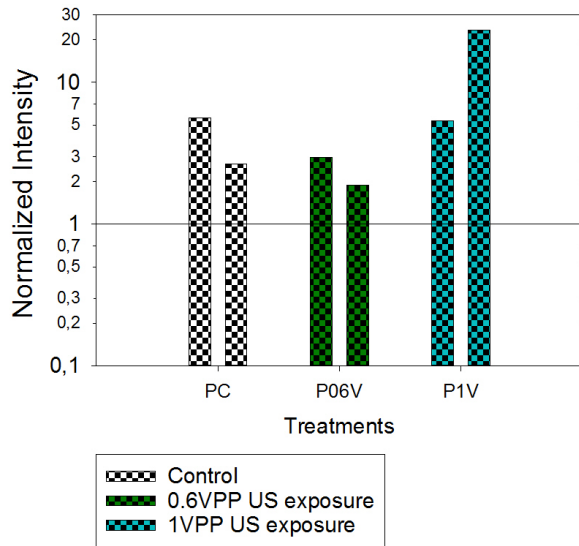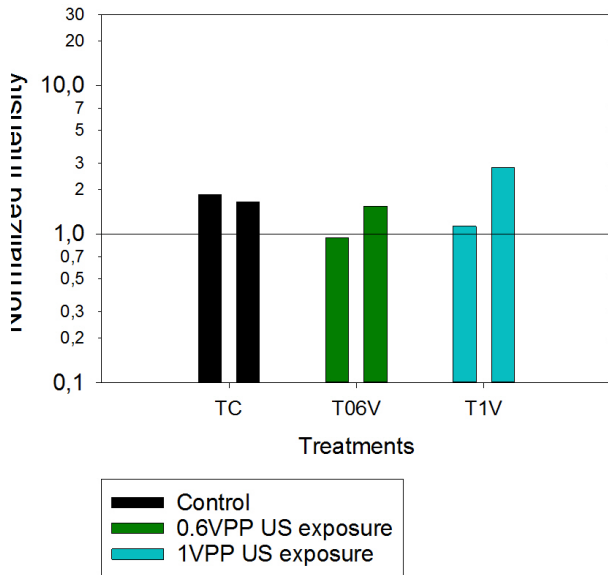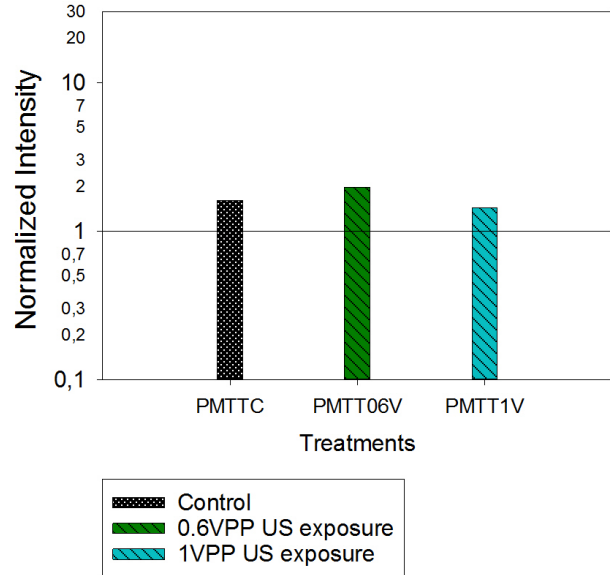
Figure 4.21: The max intensity value post US normalized to pre US is plotted on a common log scale for the two experiments of each treatment group for Polystyrene in a), Targ-233 in b) and for one experiment of each group with Targ-233 and a different detector (PMT). T06V should be disregarded, due to detector complications.

4.4.3   NP penetration inside collagen

Plots of the normalized intensity values as a function of penetration depth, starting from the collagen surface, allows us to focus on the change of intensity inside the collagen drop, as seen in Figure 4.22-4.24. The x-axis now starts from the collagen surface and goes as long imaging was carried out mutually for all ROIs, as explained in section 3.6.1. The plots include the set 5%-limit (red), and it can be seen from the plots that where this line intersects with the pre US plot (blue), is not largely affected by the surface accumulation intensity. Because these plots are normalized to the pre US max value, only the difference between the pre and post plots should be regarded, not the absolute values. The values of intensity reached inside the drop as the graph flattens out are relative to the surface accumulation in the pre US image.

For polystyrene, one experiment in each treatment group shows a rapid decline of intensity both pre and post US right after the 5%-limit in 4.22 b), c) and e). The other experiments have higher intensity values inside the collagen droplet post relative to pre and relative to surface intensity, especially the first control in a).

For Targ-233 in 4.23, the intensity are at a higher level in the post image, relative to the pre for controls in a) and b) than for any of the treatment groups d)-f), again disregarding T06V1 with the scanning error. All US exposed droplets show a relatively rapid decline of intensity inside the drop, and the intensity reach low values at the end of imaging relative to surface accumulation.

The plots that show a difference between pre and post US or control, do look similar to the pre image with scanning error, T06V1, because of their peaked nature. When the thresholded images used for analysis where inspected qualitatively, such scanning error to the same level as T06V1 could not be found. However, some added fluorescence at a lower level was observed in P1V1, P1V2 in both pre and post US images. For the Targ-233 droplets, this added fluorescence was blending in with the background intensity inside the droplet and could not be observed easily. Only for the T1V2 experiment, this added fluorescence could be observed.

For Targ-233 with PMT in Figure in 4.24, the 5%-limit is increased to 25% because images contain a larger threshold of intensity. The pre US plot is intersecting the 25%-limit in a geometrical similar area as for Targ-233 and polystyrene with the 5%-limit, close to where the curve starts to flatten out. The increase in intensity post 0.6VPP US in b) is larger than for the control and the 1VPP US exposure in a) and d) respectively. Importantly, the exclusion of the ROI with the highest surface accumulation, does not affect the values inside the drop to a visible degree, and evaluating this region as unaffected by the fluorescence from the surface is reasonable.

The distance from the collagen surface to the intensity value pre and post US or control reach the 5/25 %-limits, and the difference between them are summarized in Table 4.1. In average, the pre US intensity reach 5/25 % at 20 μm for polystyrene, 15 μm for Targ-233 and 14 μm for PMT Targ-233. In general there are small differences in how far from the collagen surface the pre and post intensity value reach 5/25 %. In two US exposed droplets, P1V2 and PMTT06V, the post intensity values never reach the 5/25 %-limits (denoted +). One of the polystyrene controls, PC1, also have a large difference between pre and post.

Intensity as a function of penetration from the collagen surface: Pre (blue) and US (green) control or US treatment for Polystyrene
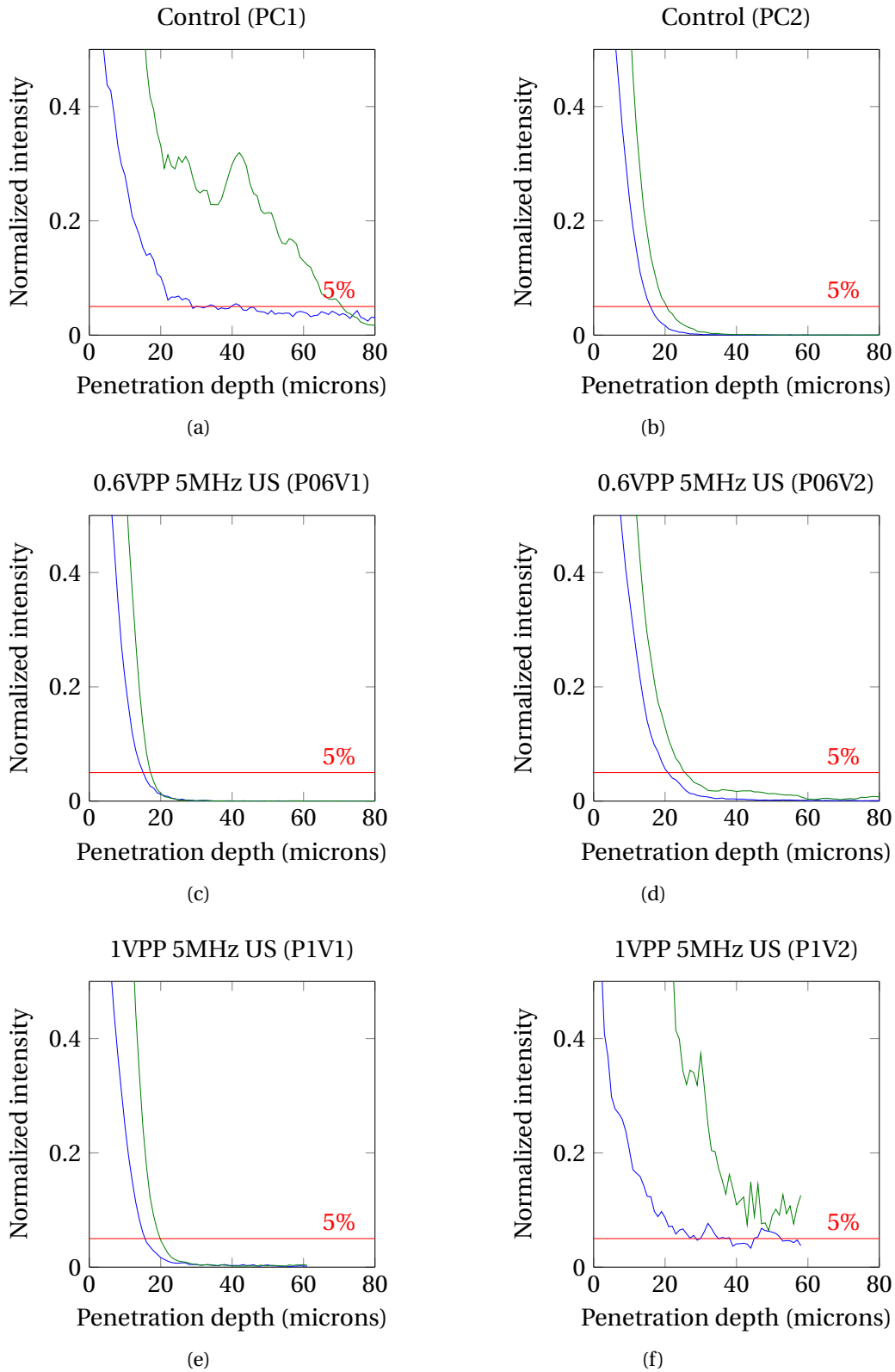
Figure 4.22: Intensity Pre and Post US and control normalized to Pre max intensity, plotted against penetration depth from collagen surface. The red line is 5% intensity of pre peak. Treatments are indicated in each subtitle. All figures are plotted with the same axis scales.

Intensity as a function of penetration from the collagen surface: Pre (blue) and
US (green) control or US treatment for Targ-233
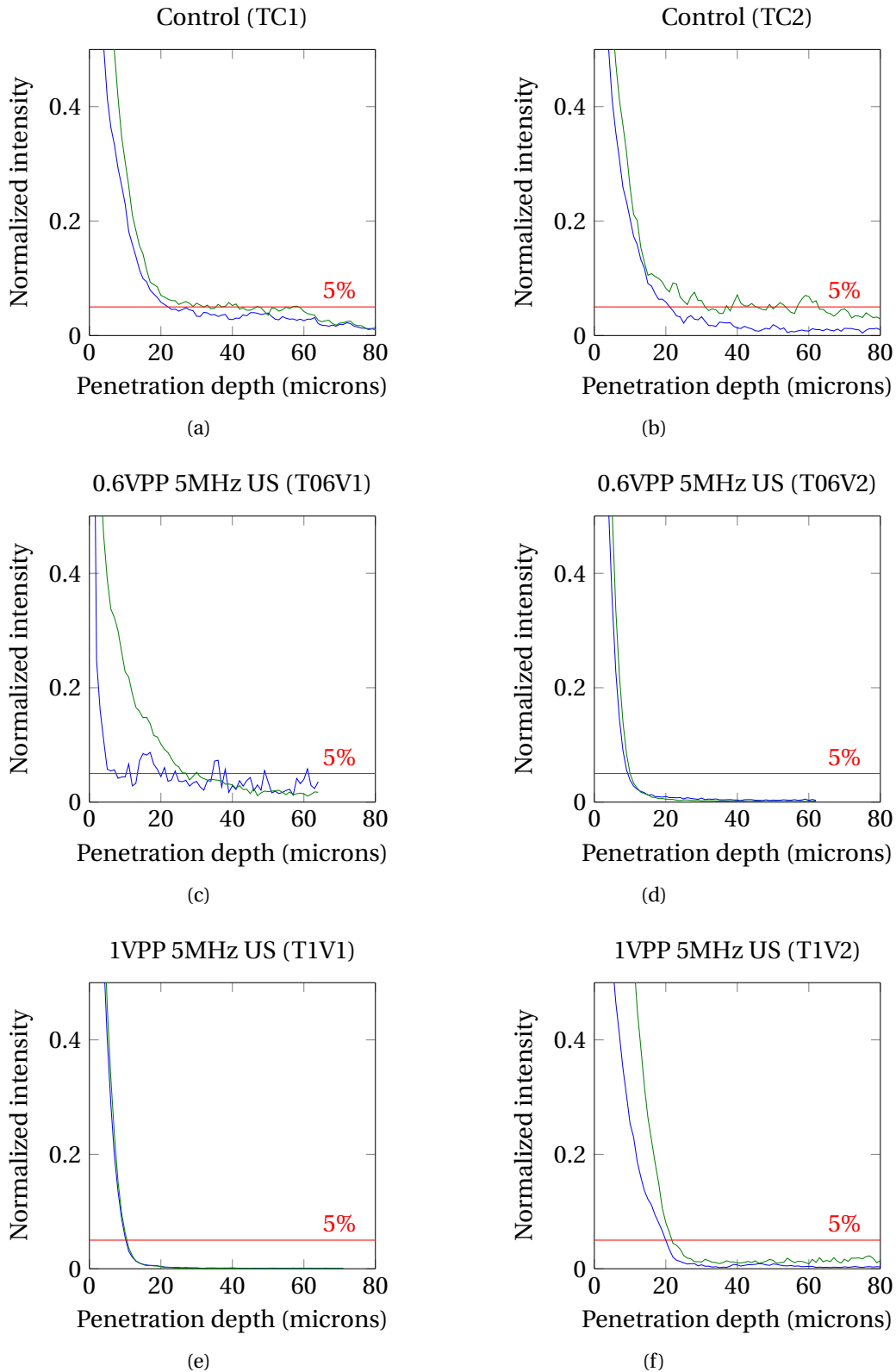
Figure 4.23: Intensity Pre and Post US and control normalized to Pre max intensity, plotted against penetration depth from collagen surface. The red line is 5% intensity of pre peak. Treatments are indicated in each subtitle. All figures are plotted with the same axis scales.

Intensity as a function of penetration from the collagen surface: Pre (blue) and US (green) control or US treatment for PMT Targ-233
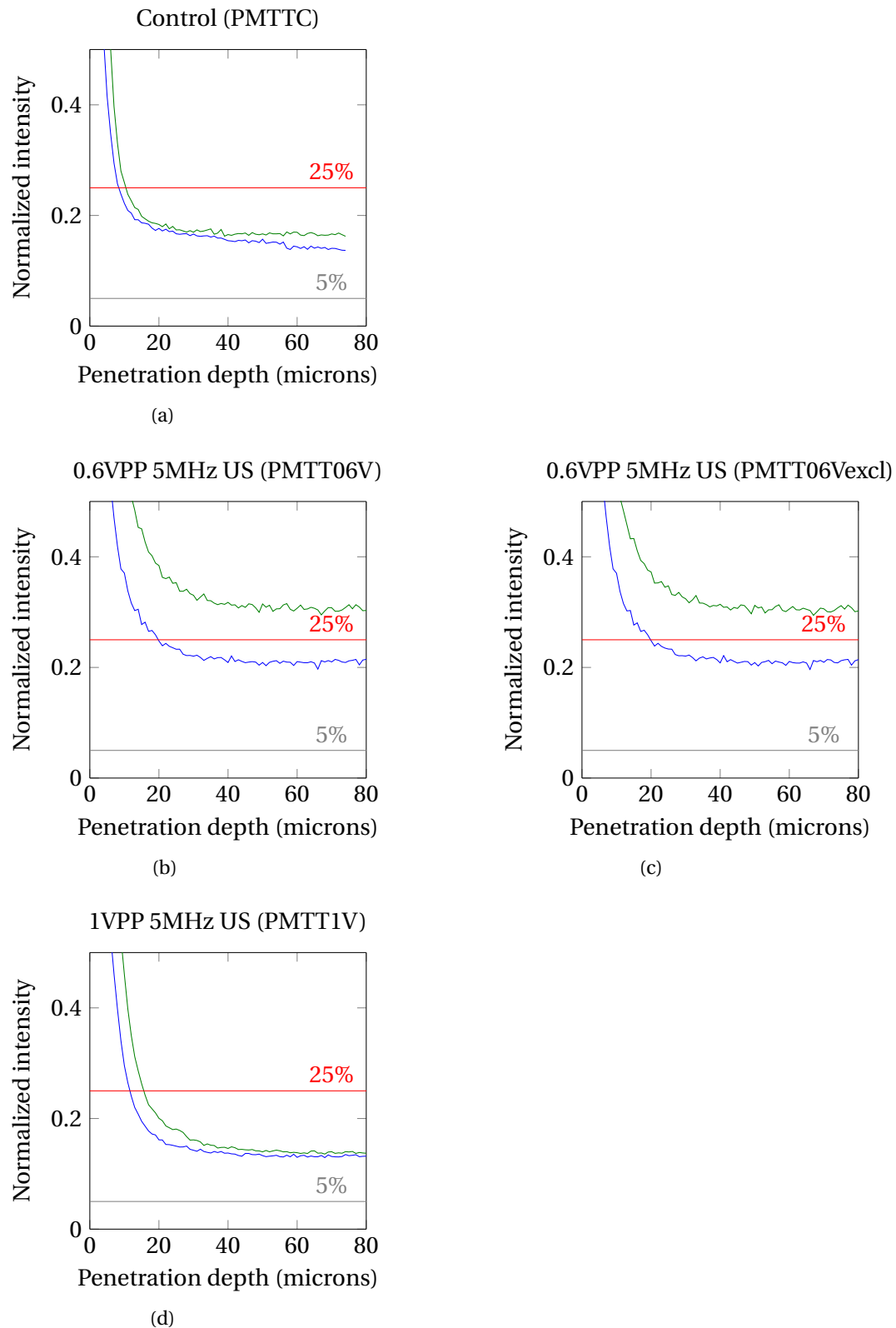
Figure 4.24: Intensity Pre and Post US and control normalized to Pre max intensity, plotted against penetration depth from collagen surface. The red line is 25% intensity of pre peak. Treatments are indicated in each subtitle. All figures are plotted with the same axis scales. n=1 for all treatments, but two values were excluded for PMTT06V, hence two figures for this treatment.

Table 4.1: Distance from surface to 5/25%-limit in μm pre and post US/control and difference

Treatment	P pre	P post	Difference	T pre	T post	Difference	PMTT pre	PMTT post	Difference
C1	30	71	41	20	32	12	9	11	2
C2	16	21	5	21	26	5			
06V1	15	18	3	7	28	21	20	87+	67+
06V2	21	26	5	9	11	2			
1V1	16	20	4	10	11	1	12	16	4
1V2	23	58+	35+	20	22	2			

4.4.4   Relative change in intensity inside collagen

The absolute intensity values pre US and post US were summed separately for 30 microns after intersection between the pre US intensity curve and the 5- and 25-%-limits respectively. The post US sum was normalized to the pre US sum and results are plotted on a common log scale in Figure 4.25.

For both polystyrene and Targ-233, large variations within the same treatment group is apparent, and the relative increase in intensity inside the collagen drop is not larger for any US treated droplet than the largest increase in a control.

PMT Targ-233 in Figure 4.25 c) show vey little difference. The increase in intensity inside the drop is slightly larger for the US treated drops than for the control. The lowest amplitude US exposure shows the larger increase.

Change in summed intensity of nanoparticles inside collagen
post US relative to pre US
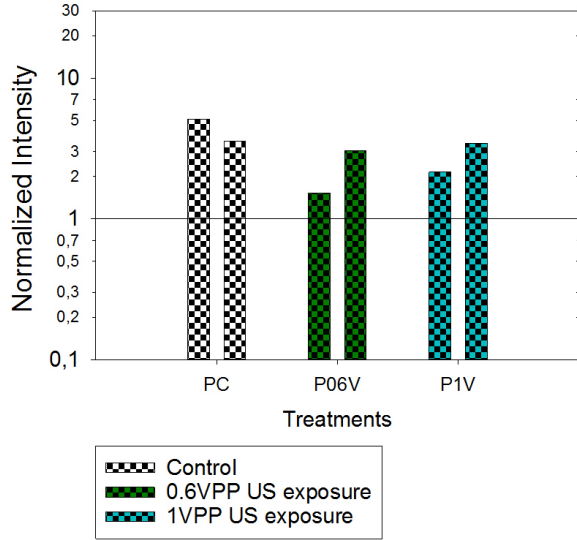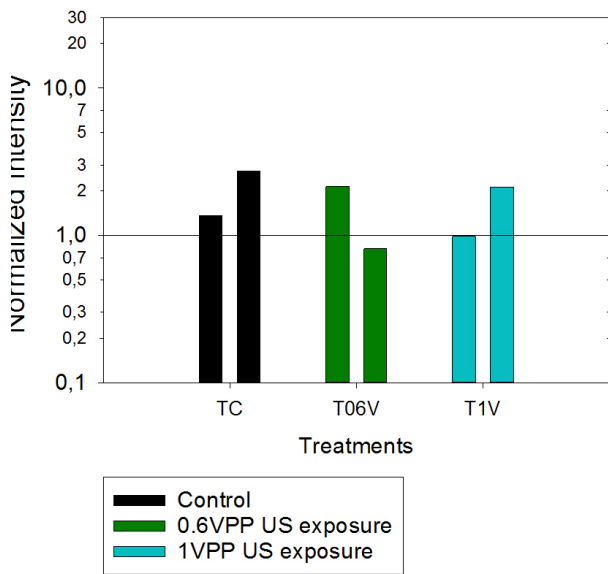
(a) Polystyrene
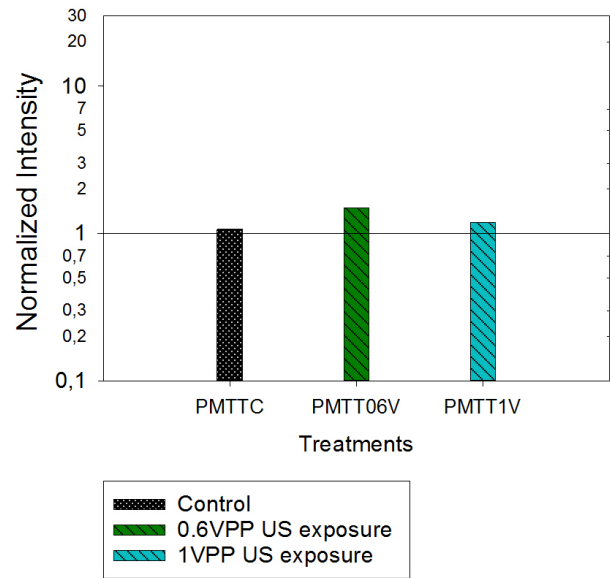
(b) Targ-233

(c) PMT Targ-233

Figure 4.25: The sum of intensity inside the collagen drop post US normalized to pre US value is plotted on a common log scale for the two experiments of each treatment group for Polystyrene in a), Targ-233 in b) and for one experiment of each group with Targ-233 and a different detector (PMT).

4.4.5   Absolute values of intensity inside collagen

The values in the plots above in Figure 4.25 are all relative to the accumulations pre US or control. To be able to compare the absolute values of intensity reached inside the collagen gel, the mean intensity of the last 20 microns of imaging was calculated.

The intensity values reached inside the collagen droplet for Targ-233 and polystyrene are plotted in Figure 4.26. The values of intensity reached inside the collagen for polystyrene are all the same or slightly larger in the post control or US exposure. The intensity is most increased for P06V2 and for P1V2. Both controls show no real change in intensity pre to post image, and the droplet of higher collagen fiber intensity, PC2, has a intensity close to zero. PC1 has a higher intensity. The 0.6V PP exposed droplet with high collagen fiber intensity, P06V2, show a relatively large increase in intensity. However, P06V1 does not show any change.

The intensity reached inside the collagen droplet controls for Targ-233 are larger than for polystyrene and are increased pre to post image. All US exposed droplets, except T1V2, show a decrease in intensity inside the collagen, with post US exposure values lower than for the controls.

(a) Polystyrene   (b) Targ-233
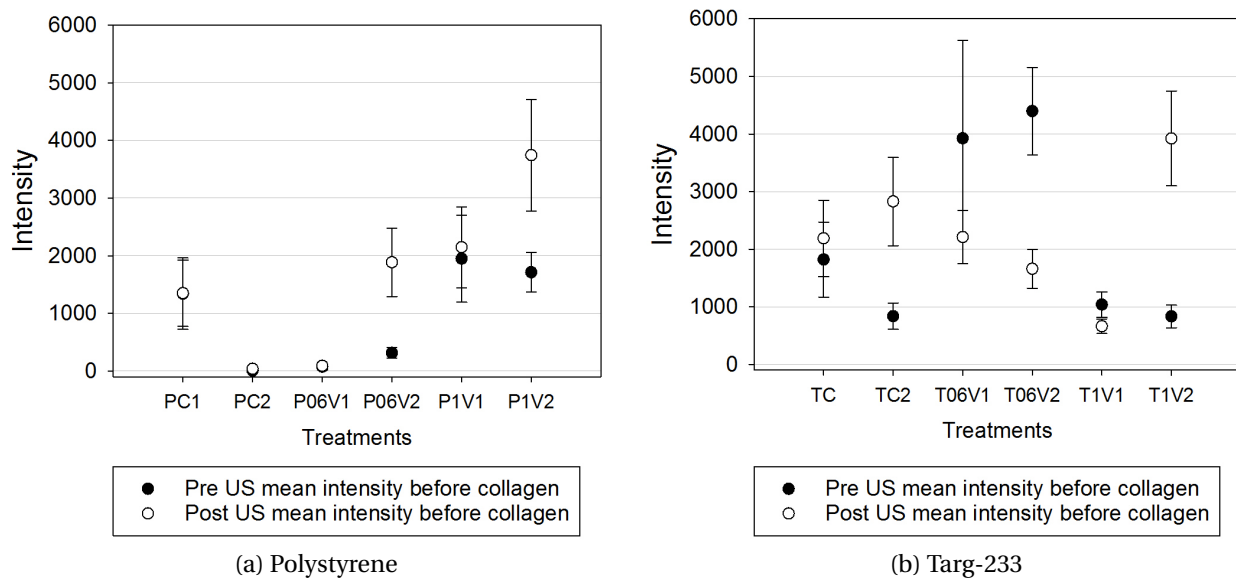
Figure 4.26: Mean values of intensity inside the collagen droplet.

The values reached inside the collagen droplet for PMT Targ-233 at the very end of imaging, were compared to the standard curve generated from serial dilutions imaged and analyzed in the same manner. The mean values of intensity of the last 20 microns were correlated to concentration, as seen in Figure 4.27. In a), the standard curve is plotted by itself, ranging from 3.25 to 240 μg/mL. The lowest value for 1 μg/mL comes from a linear regression between the values for 3.25 and 15 μg/mL ($R^2 = 1$). In b) the section between 1 and 15 μg/mL of the standard curve is replotted next to the values of intensity inside the collagen drop. The concentration correlated to each intensity value are calculated from the linear regression between 1 and 15 μg/mL and are summarized in Table 4.2. This is an estimate of the mean concentration, and the relatively small standard deviations of the mean intensity are disregarded.

Table 4.2: Concentration of PMT Targ-233 inside collagen droplet

The properties listed in this table are concentration pre US, post US and the difference between the two (post-pre).

Treatment:	Pre US concentration (μg/mL):	Post US concentration (μg/mL):	Difference (μg/mL):
PMT Control	5.9	7.7	1.8
PMT 0.6VPP	1.9	4.8	2.9
PMT 1VPP	6.4	6.9	0.5

The highest concentration reached inside the collagen is in the control experiment at a value more than half of the NP-solution the droplet was exposed to (12 μg/mL). The largest change, however is for the 0.6VPP US exposed droplet with a 250 % increase in concentration pre to post US exposure.

Standard curve for Targ-233 with PMT detector and mean values of intensity inside collagen
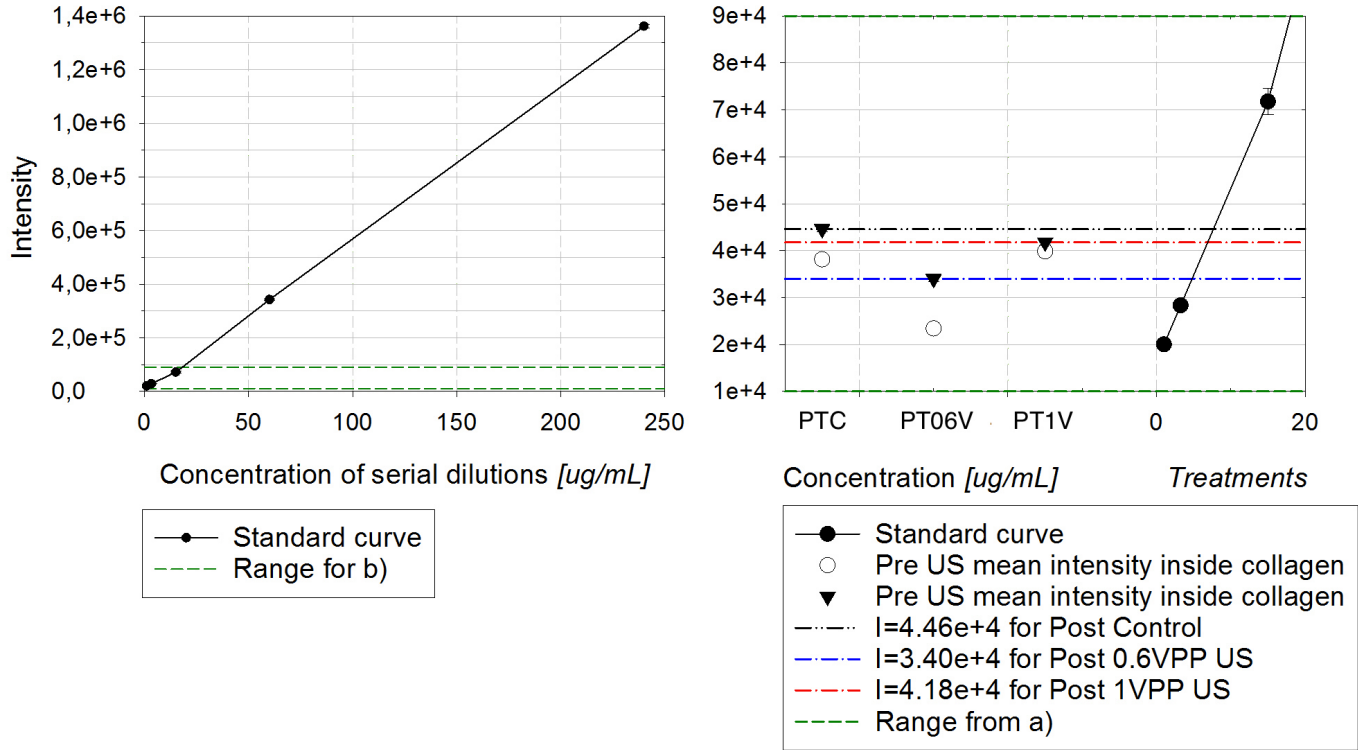
(a) Standard curve

(b) PMT Targ-233 mean values

Figure 4.27: The standard curve in a) shows the correlation between intensity and concentrations of Targ-233 in solution at 240, 60, 15 and 3.25 μg/mL, obtained with the PMT detector. The lowest value in the standard curve in found from linear regression between the 15 and 3.25 concentrations. In b) a section of this curve is replotted next to the mean values of the PMT Targ-233 intensity inside the collagen drop pre US (white circles) and post US (black triangles) for one experiment in each treatment group: TC1: Control, T06V: 0.6VPP 5MHz US exposure, T1V: 1VPP 5MHz US exposure.

4.5   Change in accumulation towards the collagen surface

The sum of intensity from a small section right above the collagen surface post US are normalized to pre US values and plotted on a common log scale in Figure 4.28. The section imaged above the droplets, was very short in a few experiments. To sum the intensity for the same distance in all experiments, a 5 micron section was chosen.

For Polystyrene in a), all experiments had an accumulation of NPs towards the collagen surface, pre US relative to post US. The largest increase is seen for one of the 1V PP US exposure. I general the 0.6 V PP US exposures showed the least accumulation.

For Targ-233, the accumulation in front of the surface is in general slightly lower than for polystyrene. The 1V PP US exposures show the largest accumulation and, disregarding the T06V1 experiment, both the control and the T06V2 PP US exposure show a decrease in NP accumulation relative to pre US values.

For Targ-233 with the PMT detectors, nearly no difference can be seen between treatment groups. They all show a slight increase in accumulation towards the surface after US/control relative to pre.

In the experiments with Targ-233 and the PMT detector, the imaging was started slightly higher above the collagen surface, and the mean values of intensity in the 10 first imaged microns can be computed. They are correlated to concentration with the computed standard curve as in section 4.4.4. The mean concentration values are in general lower than the concentration of NP solution of 12 μg/mL. In the control, the NP concentration decreases in the post image, and the highest increase is seen with the 0.6V PP US exposure.

Table 4.3: Concentration of PMT Targ-233 in front of collagen droplet

The properties listed in this table are mean concentration pre US, post US and the difference between the two (post-pre).

Treatment:	Pre US concentration (μg/mL):	Post US concentration (μg/mL):	Difference (μg/mL):
PMT Control	3.9	1.4	- 2.5
PMT 0.6VPP	2.7	5.1	2.4
PMT 1VPP	8.9	9.4	0.5

Change in summed intensity of nanoparticles in front of collagen surface post US relative to pre US
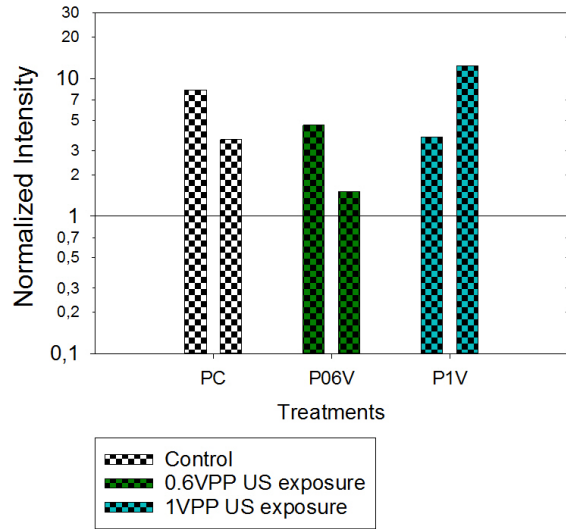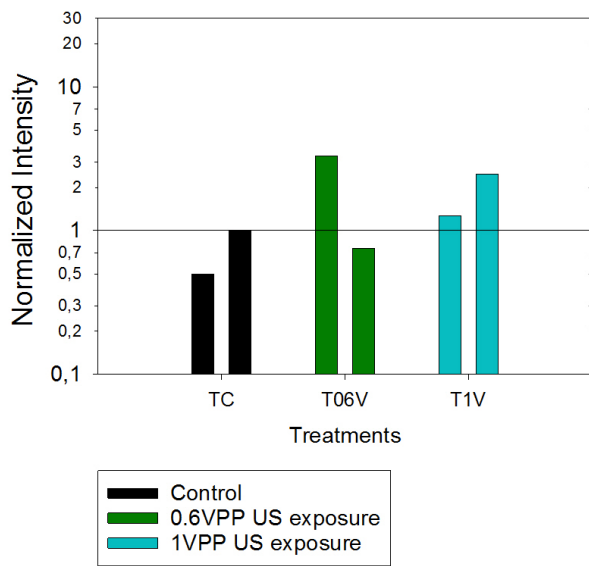
(a) Polystyrene
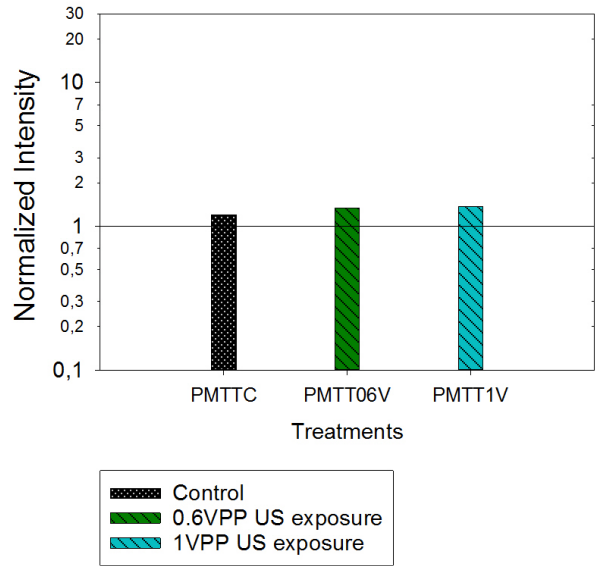
(b) Targ-233

(c) PMT Targ-233

Figure 4.28: The sum of intensity inside the collagen drop post US normalized to pre US value is plotted for the two experiments of each treatment group for Polystyrene in a), Targ-233 in b) and for one experiment of each group with Targ-233 and a different detector (PMT).

5. Discussion

This thesis describes the behavior of two different nanoparticles in relation to their interactions and distribution in collagen gel in two regimes. One regime is limited to diffusion inside collagen gel, and in the other regime a focused US is applied on the nanoparticles to generate an acoustic radiation force and a potential displacement of them. The work with the acoustic radiation force is affected by the lack of previous established experimental setups and analysis methods. The results are characterized by many attempts to analyze the obtained data in various ways to establish a good method for detecting the effect of acoustic radiation force. The methods and results from the diffusion analysis will be discussed in the first section. The next section will discuss the results from the US exposure of the particles. Lastly the concluding remarks will be summarized and the implications of these results will be considered along with improvements of the experimental setup.

5.1 Diffusion of NPs in collagen gel

The RICS diffusion coefficient experiment with polystyrene was performed once for comparison with data obtained in my project thesis [61]. In that project the diffusion of polymeric NPs in collagen gels was correlated to their different PEGylation. Those experiments were repeated three times for each particle. These previous results will be used in correlation to the results for polystyrene in the following subsections.

5.1.1 Gel reproducibility for diffusion coefficient analysis

RICS analysis of polystyrene and Targ-233 in collagen gels gave rise to very different populations of diffusing particles between the two NPs, as well as between the three experiment repetitions for Targ-233. The polymerization of fibers in the collagen gel used for the analysis, were inspected qualitatively and large variations could be seen between experiment repetitions, regards to collagen fiber structure, as length, thickness and intensity overall in the reflection image. To be able to see a potential difference between the diffusion coefficients among NPs with different properties in collagen gels, the effect on diffusion originating from differences in the gels must be negligible.

As explained in section 2.10, the NPs transport in ECM in central areas of a tumor is dominated by diffusion, and the transport in the tumor matrix is limited by binding of particles and degradation. The fraction of particles in a gel that interact with and bind to gel fibers could be affected by the degree of fiber polymerization, more specific; the fiber volume fraction, the structure and orientation as explained in section 2.10. Many experimental studies have examined the dependence of the diffusion coefficient

on the fiber volume fraction both in vitro [48, 80, 77, 9] and in vivo [70, 76, 30, 57]. Studies on the effect of collagen structure have also been done, and these reports are contradictory [57, 92, 30].

Experimental findings have shown that diffusion can be significantly hindered by electrostatic interactions between the diffusing particle and charged components of the extracellular matrix, as positive patches on the collagen fibers, [60, 96, 28]. The effect of charge on the diffusive transport of nanoparticles in the extracellular matrix of biological tissues has been related to the fiber size in the matrix [93]. By using a mathematical model, it was found that when the fiber size is comparable to a charged particles Debye length, electrostatic forces between the fibers and the NPs result in slowed diffusion. However, as the fiber diameter increases the repulsive forces become less important. In contrast, [30] studied the diffusive transport of macromolecules in collagen gels and found no correlation between fiber network structure and macromolecular diffusivity.

Factors like pH and varying NP concentration were found to affect collagen polymerization to a lesser extent in my previous project. Rather gel preparation time, and/or temperature changes related to it, seemed to affect the collagen polymerization more. Longer and thicker fibers were found in gels allowed to polymerize right after solution preparation. This stands in contrast to results of the effect of a prolonged nucleation time at low temperatures (about 4 degrees Celsius) to allow collagen fibers to assemble thicker and longer fibers [95, 64, 99]. Possibly the temperature on ice is to high or not well enough controlled in these experiments. Another possibility is that the collagen preparation solution was not homogeneous even after mixing and the pipetted volumes might contain different total amounts of collagen, that would affect resulting polymerization [1].

The fraction of particles interacting with collagen in this project are therefore likely to be dependent on collagen fiber volume fraction and fiber size between each experiment repetition, in addition to the NP's properties. Because of the highly negative charge of the polystyrene bead, and the corresponding Debye length, it would be expected to interact with collagen fibers of certain diameters differently than Targ-233 with low zeta potential. Even when the collagen gels made in this project look different on the reflection images, observed with the naked eye, they could still be similar enough on molecular level. A further analysis of the fiber volume fraction and the fiber size would be needed to characterize the collagen gels, in addition to more experiment repetitions.

The collagen gels of various polymerization degree were found to present a valid model of in vivo tumor ECM for studying PEGylated NPs in my project thesis [73, 2, 11]. The diffusion of water was found to be slightly higher in collagen gels than in tumor tissue with DW-MRI. This indicates a larger barrier to diffusion in vivo, than in the model. The interactions between collagen and PEGylated NPs present a barrier to diffusion that would increase with more negative NP zeta potential.

5.1.2 Multi-modalities, aggregations and RICS

An inhomogeneous distribution of polystyrene and aggregation was observed in collagen gel. In addition multiple NP mobilities (modalities) were observed in the collagen gels from my project thesis and could be an argument against using RICS as an analysis method because the autocorrelation functions would reflect the complex, non-homogenous dynamics of the multi-modalities and thus are not adequately described by the single component model used to fit the auto correlation function from solution measurements [8]. RICS can detect a relatively wide range of diffusion coefficients as explained in section 2.13, however when these are both represented in the same region of interest, the RICS software cannot

separate between them, although two peaks sometimes are seen in the autocorrelation curve.

At the same time, this result is also an argument supporting the later division of particles into three diffusion groups. A requirement for the analysis is then, that enough smaller regions predominated by one modality at the time are selected and individually autocorrelated. However, the result will be influenced by this selection and to which degree each particle mobility are dominating it. By manually selecting regions to analyze, the "ease of fit" (autocorrelation) for the mobile particles, relative to the immobile and intermediate diffusing particles in gels, will bias the fraction distribution between the diffusion groups towards mobile diffusing particles.

The confocal scanning speed selected for RICS analysis in this project was optimized for detection of particles in collagen gel, and not neccessarliy for the detection of particles diffusing in solution. In addition the diffusion rate of a smaller particle as polystyrene in solution should be higher than for a larger particle as Targ-233. It has been shown that the selection of speed can render the application of RICS more suited to the study of specific particle size ranges [38]; the speed should be selected slightly slower that the speed the particles, as explained in section 2.13. This implicates an optimal speed selection for the mobile particles in gel and solution to be faster than for the "intermediate" diffusing particles, and also a speed selection for polystyrene in solution to be higher than for Targ-233, rather than using the same scanning speed as in this project. By using the same scanning speed however, correlation between experiments can be drawn directly.

The diffusion coefficient of the mobile NPs in the ECM is a results of interest clinically. The mobile particles are the ones that could potentially penetrate tumor ECM and deliver drugs to the tumor cells, and the measurements of other mobilities are necessary to estimate the fraction of them.

5.1.3 Diffusion coefficient of NPs

The highly negative particle without PEGylation, polystyrene, did show a poor diffusion in collagen gel, with no mobile particles detected and a diffusion coefficient largely hindered relative to its diffusion in water. Polystyrene was found to aggregate in the gel, possibly adhering to positive patches on the collagen fibers, fully covering the fibers. Such aggregation makes the RICS analysis method inappropriate as explained above. The experiment was therefore not repeated, and the result obtained from the diffusion in the gel should be regarded as an example where no mobile particles could be detected, rather than using the resulting values directly. This find correspond well to results from my project thesis where it was found that poorly PEGylated particles, with resulting higher negative zeta potential had no or smaller fractions of mobile particles.

The transport of well PEGylated NPs, as Targ-233, in collagen gels gave rise to a two-component diffusion; a mobile fraction associated with the aqueous phase of the collagen network with a diffusion coefficient similar to that in water. The mobile populations of the NPs had a diffusion coefficient between 1 and 3 μm^2/s, and the diffusion coefficient was not significant different from values obtained in solution; (P>0.05) for each particle. The fraction of particles with significantly hindered diffusivity was associated with the viscous phase of the network, supported by similar finds in literature [47, 60, 96, 28]. The heterogeneous distribution of collagen in gels is representative to the heterogeneous distribution of components in the the interstitial matrix (IM) in the tumor that separates the matrix in the two phases [4, 15]. The viscous phase is considered to be in regions of high collagen-fiber concentration and significantly hinders the particle mobility. The aqueous phase is found in low fiber-concentration regions

where the particles diffusivity is less hindered. The volume fraction of collagen therefore plays a major role for the diffusion of nanoparticles. The well PEGylated particles showed the highest diffusion coefficient and the largest fraction of mobile particles, relative to the less PEGylated particles, in correlation to similar studies with PEGylated macromolecules in the literature [21, 58].

Polystyrene has a larger diffusion coefficient in water than Targ-233 as expected for a smaller sized particle. However, in the gel this correspondence between size and diffusion is not found, confirming that the surface modulation of the particles and their resulting charge is more important for diffusivity in the ECM. This result was also seen in my project thesis; The diffusion of the NPs with various PEGylation in collagen gels, showed a correlation between the degree of PEGylation and fraction of mobile particles in the gels and no effect was seen between size and diffusion in gels, contradicting results of diffusion in solution.

One NP in my project thesis, that is known to be less PEGylated resulting in a larger negative zeta potential, was found to interact with collagen to a higher degree in the collagen gels and had basically no mobile fraction of particles. The polystyrene bead has a different surface modulation than the PEGylated particles, but is behaving similarly in the gel adhering to the collagen fibers. The polystyrene bead has a even higher negative zeta potential and would likely adhere even stronger in the gel.

Because diffusion of Targ-233 gave rise to large variations in fraction of mobile particles between experiment repetitions, it is likely a result of the difference in collagen polymerization between the gels. However, even if the fraction of the populations varied in each experiment repetition, the populations were represented in all collagen gels. If the polystyrene beads characteristics allowed for mobile particles in collagen, it should also show a small fraction of mobile particles in a gel consisting of any degree of polymerization of collagen this experimental procedure would allow result in. This is not the fact, and polystyrene is expected to be immobile in any collagen gel matrix of this concentration in experiments where it is mixed with collagen pre polymerization.

5.1.4   Implications of diffusion analysis

The analysis of diffusion of polystyrene and Targ-233 in collagen gels, gives insight to their distribution and interactions in collagen gels. As described in section 2.10, the NP transport in tumor ECM is limited to diffusion, that limits the effect of drug delivery. Based on the diffusion of polystyrene, highly negatively charged unPEGylated particles are not suited for penetration of collagen matrixes. Studies show that both highly positively and negatively charged particles will be effectively filtered out by the ECM [60]. Targ-233 on the other hand, show promising characteristics for ECM penetration. The effect of PEGylation regards to diffusion in the ECM is well supported in the literature, as seen referenced above 5.1.3. A high degree of PEG molecules on the particle surface does reduce the charge of the particles and along with steric hindrance allowing the particles to penetrate further into the tumor ECM and deliver chemotherapeutic agents to cancer cells.

The results of the distribution and diffusion of polystyrene in collagen gel imply that the polystyrene bead would be immobile in a collagen matrix, possibly also when distributed as a solution on top of a collagen as in the next section with the collagen droplet model and US exposure. If the application of FUS exposures to polystyrene in solution above collagen tissue leads to an increased NP penetration into collagen, relative to control, it would most likely originate from an acoustic radiation force large enough to push the NPs into the collagen. This in contrast to an increase in temperature and diffusion that would

only lead to NP deposition on collagen fibers close to the surface. Targ-233 in solution above collagen tissue, would be expected to have populations of mobile particles in the inter fiber spaces between the collagen fiber, as well as populations of NPs adhering to the fibers to varying degrees. The mobile fraction of particles, would potentially be easier to displace with high enough applied force and increase penetration into the collagen tissue.

The zeta potential of Targ-233 is lowered by the addition of PEG molecules on the surface and the PEG molecules reduce steric hindrance in ECM. In addition mobile charge carriers in the collagen solution (eg. from PBS), is able to screen the opposite charges between Targ-233 and positive patches on collagen fibers to a certain degree, resulting in this mobile fraction of NPs diffusing freely in between fibers. This can result in a contrary effect as above; A high force applied on the mobile particles might be able to push the NPs towards collagen fibers and allow for charge interactions that would be shielded at lower NP velocities as in the diffusion regime.

5.2   Acoustic radiation and penetration of NPs into collagen

This section focuses on the establishment of an experimental setup and analysis that would be sensitive to an effect of acoustic radiation force. The imaging before and after US exposure or control, done with CLSM, led to a few challenges as the scanning error in the detectors, as explained. In addition alignment of the well plate on the microscope stage was a contributor to alignment offsets in the XY-plane in the image. The new water droplet placed on the objective lens each time, gave rise to alignment offsets along the Z-axis. The water immersion objective was used because of its long working distance. A large area, at a large penetration with short distance between images was desired to image to be sure of imaging the potentially treated area. As a compromise to time limitations a small zoom was used and an area larger than the FUS beam width was imaged.

5.2.1   The choice of collagen model for FUS exposure

The choice of a collagen model in a small droplet form over a relatively thicker collagen layer was a difficult choice, and the complications, limitations and advantages of both models in relation to the US exposure setup available, are discussed in this subsection. The resulting convex shape of a droplet stand in contrast to the collagen layer covering the bottom of a well plate, resulting in a concave shape because of adhesion interactions between the gel and the well walls. The thickness of the models are limited by the working distance of the confocal microscope.

Research done by Frenkel et al. [32], is among the few publications discussing the effect of US on penetration of NPs in tissue. In one study, US was applied to NPs in solution on top of fish skin and the penetration depth was investigated with electron transmission microscopy. They showed that cavitational US was necessary to get NPs across the first epidermal layers, but once inside, non-cavitational US exposures showed an increased diffusion rate and penetration depth of NPs inside the tissue. Non-cavitational US also increased the flux of NPs towards the surface of fish tissue. Because not much research is done previously within this field, a model similar to the one used in the study by Frekel et al. was desired to develop for comparison. Collagen tissue submerged in NP-solution would be a similar model, but lacking the first epidermal barrier to penetration.

Alignment and precision in the experimental setup while working with FUS exposures and imaging is important, as the treated area from one FUS exposure is expected to be the same size or smaller than the FUS beam width. The experimental setup was developed from supplies at hand, and was improved continuously to minimize alignment offsets between the FUS beam and the gel model. The thin collagen layer was the desired model compared to a small droplet because hitting the layer with the FUS would be certain. In addition, the concavity, would be less than the convexity of a very small volume of collagen deposited in the droplet model, and exposure to air and dehydration would be less as well as it could simplify later analysis.

Because of time limitations, it is not possible to image the whole collagen layer surface, hence it is crucial that the FUS treated area is included in the imaged section, to see a potential effect from FUS exposure. This would be an easy task if the FUS was in fact centered in the very middle of the well plates. However, the alignment lids did not succeed in centering the FUS in the well plate and straight forward centered imaging of the well plates was not possible. A possible solution would be to find the coordinates of where the alignment lids did in fact place the FUS beam. But because these coordinates would be offset from the center, the concavity of the layer would give rise to unsymmetrical contributions of variations in height profile of the collagen layer in an imaged section.

Based on these issues, the collagen droplet model was developed, rather than a collagen layer to be able to place collagen exactly where the FUS would hit it and to later know where to image. The thickness of the collagen droplet vary across the surface, but with imaging centered relative to the center of the droplet, these thickness variations would be of symmetrical contributions. In addition, more experiments could be carried out for smaller volumes of prepared collagen solution. While the droplet model solved some issues as knowing where to image, it also gave rise to new problems. Because the alignments lids did not support the transducer holder well enough, alignment offsets was still an issue, and the uncertainty of knowing wether a drop was in fact hit by the FUS beam or not, was still prominent. Later analysis would also be more accurate if the FUS beam hit in the very middle of the droplet.

5.2.2 Collagen polymerization in droplets

The collagen fibers in the droplets used for US exposure experiments, showed large variations in fiber polymerization and image intensity, that could affect the fraction of mobile particles and charge interactions with the NPs, similar to the collagen gels used for RICS analysis. In addition the collagen surface is important in the droplet model, that leads to an even larger variations within the imaged sections than within a thicker gel. The convex surface of the gel droplet has a large area to volume ratio, relative to a collagen layer. Overall, the collagen fibers at the surface of the collagen droplet were affected by exposure to air, relative to the fibers deeper inside the droplet, seen by an increase in intensity with penetration depth. The time the collagen droplets were stored in the fridge before use, might have led to dehydration of the outer layers of collagen fibers and would vary between experiment repetitions. Possibly the more dehydrated fibers, were damaged and had a disrupted structure, and possibly a lower concentrations of assembled fibers. A dehydration and air content between the fibers might lead to a larger barrier for NP penetration along with US scattering. On the other hand it might lead to an increased absorption of fluid, hence increased flux of fluid and NPs into the droplet. The effect of submerging them in NP solution during the run of an experiment, did however not seem to affect the fibers. It was not possible to keep the droplets in solution over long time because they would loosen from the well plate. The small droplets of

water placed in the well corners to hydrate the environment might or might not have helped.

The accumulation of negatively charged particles on collagen fibers would be expected to be correlated to fiber density, polymerization and fiber diameter as explained above. The diffusion of the NPs into the collagen droplet would be expected to be positively correlated to the fiber volume fraction. Well polymerized collagen fibers with large inter fiber spaces would allow mobile particles to diffuse through the collagen tissue.

A high intensity of fibers in the reflection images of collagen can be correlated to a well polymerized fiber with potentially larger inter fiber spaces. Lower intensity of the fibers made of the same concentration of collagen might imply poor polymerization, smaller fibers and monomers and possibly less inter fiber spaces.

Qualitatively, the droplets of higher intensity of collagen at the surface was ranked from highest to lowest fiber image intensity (T06V1 is excluded here):

Polystyrene: P06V2>PC2>P1V2>P06V1>P1V1>PC1

Targ-233: T06V2>T1V1>T1V2>TC1>TC2

PMT Targ-233: PMTTC>PMTT1V>PMT06V

5.2.3   Accumulation of NPs pre US

The pre US/control images show a high accumulation of NPs on the surface. The degree of accumulation in the pre image varied between experiment repetitions, and is likely dependent on the polymerization of the fibers.

The accumulation on the surface pre US or control is expected to correlate positively with higher concentrations of collagen for polystyrene. For Targ-233 with fractions of particles associated to the inter fiber spaces as well as adhering to collagen, the correlation might be different. When the absolute values of pre surface accumulation is arranged in highest to lowest value, a very similar ranking as above can be seen for Targ-233. Higher intensity of the collagen image relates well to higher pre accumulation on the surface of Targ-233. For polystyrene, on the other hand, the order is almost exactly reversed. The accumulation of polystyrene on the surface is inversely related to collagen fiber intensity:

Polystyrene: P1V1>PC1>P06V1>P1V2>PC2>P06V2

Targ-233: T06V2>T1V1>T1V2>TC1>TC2

PMT Targ-233: PMTT1V>PMTTC>PMTT06V

This qualitative comparison suggest that polystyrene accumulates to a higher degree to poorly polymerized collagen with smaller fibers. Targ-233 on the other hand is present on the surface to a higher degree in collagen that is well polymerized, possibly distributed with the mobile populations in between the fibers in the aqueous spaces as well a population of particles interacting with the fibers.

Both polystyrene and Targ-233 are present to a large degree on the surface, but both particles do not penetrate far into the tissue, relative to the large surface accumulation. 5 % intensity of the surface intensity is in average reached at about 20 and 15 microns into the drop for polystyrene and for Targ-233, and after this the relative intensity drops to low positive values to the end of imaging in most experiments. This suggest a low diffusion or accumulation of both particles all the way through the imaged section. The degree of accumulation in the pre image varied substantially between experiment repetitions, and is likely dependent on the fiber volume fraction and polymerization of the fibers as well.

5.2.4   US exposure and resulting force

The duty cycle of 0.2% used in the in experiments is relatively low and could possibly be too low to apply enough force on the NPs. Out of the 10 minutes of sonication there is an effective treatment of 1.2 seconds only. The resulting acoustic radiation force based on the parameters used in the experiment and obtained from water tank characterization the transducer was simulated for the two voltages used in the experiment, with in house simulation software by Petros Tesfamichael Yemane (IFY). The simulated acoustic radiation force as a function of penetration into the collagen droplet is plotted in Figure F.1 in Appendix F. The peak positive pressure from the transducer generates an acoustic radiation force when the pressure wave reaches a medium of different absorption than water. The acoustic force arising from one FUS cycle at the interface between the solution and the collagen surface reaches maximum values of 8.2 and 32 mmHg/m for 0.6V PP and 1V PP amplitude respectively. In MPa/m, the values are 1.1 and 4.3 MPa/m respectively. During sonication of 10 minutes, $3x10^8$ cycles are sent from the transducer towards the collagen surface, each generating this force at the interface. These max values can be reached at the very surface of the collagen, when the FUS focal distance is perfectly aligned with the interface. Because of absorption and scattering of the energy in the collagen tissue, this force quickly declines into the collagen droplet. The thickness of the collagen droplet is about 1 ± 0.2 mm thick, and an acoustic force could penetrate the droplet and reach the well plate bottom, potentially resulting in standing at this interface.

   Based on simulations, there would be a relatively high force acting on the NP solution and the collagen tissue in the droplet, if the FUS is in fact well aligned with the droplet. The resulting velocities of one NP is correlated to the acoustic force acting on one particle and the drag of the particle resulting from the difference between the fluid streaming velocity and the NP velocity (ref Eq Mia). However, estimations of fluid streaming velocity and acoustic force acting on one NP is not straight forward. Therefore estimations of how far the acoustic force potentially could push a particle were not achieved.

5.2.5   The analysis of acoustic radiation of NPs in collagen gel

The expected distance the acoustic force potentially could push a single NP is unknown, leading to various attempts of analysis methods. In the study done with US and fish skin, an increase from 37 to 53 μm in max penetration depth is found between control experiment and US exposure [32]. In addition an increased flux towards the fish surface and the concentration inside the fish skin was increased with US. The epidermal layer of the fish skin, would constitute a larger barrier to NP penetration than the collagen droplet. Based on this report, the effect of US exposure on flux towards the surface, surface accumulation, accumulation of NPs inside the droplet and values of intensity reached at end of imaging, was attempted. All analysis methods showed large variations within each treatment group and NP distribution in the collagen droplets varied to similar levels for both control experiments as for most US exposed droplets. Because of the large variances in NP accumulation in the pre images, normalized increases in intensity to pre accumulation was necessary to limit the effect of various collagen polymerization. The expected effect of ultrasound applied for 1.2 seconds might not be large enough to encounter the effects of various attractions to the collagen fibers during the post imaging of about 55 minutes. Because the collagen droplet is exposed to a large volume of NP solution of freely diffusing particles, a possible difference in deposition caused by FUS could be overshadowed by overall accumulation.

   In the literature, the penetration of NPs and macromolecules are usually presented as a maximum distance of penetration from a reference point along with intensity or concentration as a function of

penetration depth[85, 32]. Because nanoparticles were detected all the way through an imaged section, this maximum distance of penetration would be the same for all experiments. Both the total intensity directly inside the collagen droplet and the mean values reached inside droplet at the end of imaging were analyzed. Large variations exist within each treatment group for both analyses and it is difficult to see any difference between controls and US treated groups.

The NP intensity plotted as a function of penetration depth into the collagen cannot be correlated to penetration of NPs for the first 15-20 microns starting from the surface because the intensity in this region most likely was overshadowed by the surface intensity for both polystyrene and Targ-233. The choice of a collagen model covered in NP solution might not be suitable to detect an increase of penetration as a result of acoustic radiation force if the displacement of NPs are less than 20 microns.

5.2.6 Surface accumulation

The increase in accumulation on the collagen surface, was larger for the more negatively charged polystyrene than for Targ-233 in all treatment groups. The PEG modification of the surface of Targ-233 shields the charge and do not bind well to the collagen fibers. The carboxylate surface modulation on polystyrene, is allowing it to bind strongly to the fibers.

The one high 1V PP US exposure that shows an especially high surface accumulation of over 20 times larger intensity post US than pre US, was pre imaged twice. Although the time between the second pre image and the post image are the same as for the other experiments, it has more than three times as high accumulation as the largest accumulation in a control. This result shows a non-linear relation between accumulation of polystyrene and time. Polystyrene is charge stabilized and does not aggregate in solution. Therefore the addition of polystyrene to the collagen surface should not attract more negative particles, and it is possible that the deposition rates onto the collagen surfaces are very different for each droplet.

Even if the penetration of NPs were difficult to detect or an acoustic radiation force did not succeed in pushing particles into the collagen at all, the pressure wave applied would be expected to increase the deposition of NPs onto the surface to a larger extent than diffusion only. This is not the case, and there are no clear differences between treatment groups. It is possible that the alignment in the exposure setup was too large for a few of the experiments, but it is not likely that only one droplet was in fact hit by the FUS. Possibly the duty cycle of the US or the pressures were too low to increase deposition of particles to a larger extent than variations in gel polymerization would lead to.

5.2.7 Change in intensity above collagen surface

The calculation of the effect of the change in NPs above the collagen surface was limited to very short regions for certain experiments because the imaging was started close to the collagen surface. For a pressure wave propagating in water, a homogeneous displacement of particles throughout the water propagation would occur. As seen in the acoustic radiation force simulations, a force is generated also in the region directly above the very collagen surface at 67 mm for 5 MHz, that could potentially lead to a concentration gradient towards the surface. Flux of particles towards the surface were slightly larger in controls than in US exposed droplets for polystyrene and Targ-233, contradicting this. For PMT Targ-233, there are no real differences between treatment groups when the intensity in the 5 microns directly

above the surface of the droplet are summed. However, when the mean intensity of the 10 first microns are compared to concentration, a small decrease is seen for the control, and the larger increase is seen with 0.6V PP exposure, followed by 1V PP. Possibly, the deposition of NPs in the control are deposited at a fast enough rate to render the concentration in the solution, whereas the US exposed systems have an increased flux towards the surface.

5.2.8   Intensity inside the collagen droplet

An increased surface accumulation did not directly correlate with the change in intensity directly inside the droplet for Targ-233 and especially not for polystyrene. The droplet with the largest surface accumulation for polystyrene did not show the largest sum of intensity inside the droplet. The accumulation of polystyrene and Targ-233 on the surface is not able to penetrate far into the droplet, during the time of the run of an experiment. For Targ-233, the experiments showed a smaller increase in NP accumulation in this region than for polystyrene. This result is contradicting the results showing less interaction in and higher mobility of Targ-233 in collagen than polystyrene. It is possible that the values summed after the 5/25 %-limits are still affected by the surface accumulation intensity which is larger for polystyrene than Targ-233.

The intensity reached at the end of imaging where the intensity curve flattens out, might be the most promising analysis method, with the analyzed area being unaffected by the fluorescence originating from the collagen surface. However, the low intensity values in this region might be affected more by scanning error for polystyrene and Targ-233 than the surface, but probably most of it is taken away while thresholding the images. The penetration of a particle this far from the surface is also very likely dependent on collagen polymerization.

For polystyrene, two experiments have increased the penetration of polystyrene into collagen, to a larger degree than diffusion only in the two controls that both showed no increase. The two other US exposed droplets showed a low increase in NP penetration similar to controls. Possibly the two experiments with an effect were hit by the FUS beam, and the other ones were poorly aligned, or the gels used in these experiments were easier penetrable.

Interestingly, the intensity values pre US are in general slightly larger for Targ-233 than for polystyrene, in accordance to the distribution of mobile NPs in the gels. The difference is however not as large as in the diffusion analysis. There might be a higher population of mobile polystyrene NPs when the particle is added as solution after collagen polymerization has occurred, rather than mixed in before polymerization.

Targ-233 values show a negative effect of US exposure on NP penetration in three out out four experiments. Only one US exposed droplet has a positive accumulation of NPs relative to pre image. Because the values are so low in this region, relative to potential scanning error added fluorescence, the mean values for PMT Targ-233 should rather be emphasized.

The mean values of intensity reached inside collagen droplets with PMT Targ-233, correspond to concentrations of NPs between 16 and 53 % of the NP solution the collagen is exposed to at the surface. These values were increased in all three experiments, especially for the one 0.6V US exposure with 250 % increase. However, the values of concentration reached after US exposure, did not exceed values occurring because of diffusion only in a control gel.

5.3 Concluding remarks

5.3.1 Diffusion and distribution of NPs in collagen gel

The polystyrene bead is adhering strongly to collagen when it is mixed in prior to the formation of the fibers, and no mobile particles can be found. The multimodal diffusion of well PEGylated Targ-233 gave rise to fractions of mobile particles in all collagen gels of different polymerization when mixed in prior to the formation of the fibers.

5.3.2 The effect of acoustic radiation of NPs in collagen gel

The effect of acoustic radiation force acting on the NPs in this model, is not large enough to show an effect on NP penetration, surface accumulation or flux towards the collagen surface for this droplet model. The variability in the NPs affinity towards the different collagen fibers constituting each gel droplet, gives rise to as large variabilities within each treatment group as between treatment groups.

The effect of acoustic radiation force arising at the interface between the collagen and NP solution was simulated. The simulation show a large maximum force at the very surface of the collagen droplet that potentially can lead to fluid streaming and NP displacement if alignments between the FUS focus and the droplet are made correctly. The FUS exposure in these experiments was either not aligned well with the collagen droplet, of too low pressures and/or duty cycles. Potentially a surface can also be scanned with FUS. However calculations of the effect of one exposure per region will be less straight forward.

The droplet model might not be a suitable model for a proof of principle of acoustic radiation force, but it rather reflects large variations in deposition of NPs in solution as a result of diffusion and charge interactions, unaffected or not by the FUS applied. The large variations for the various analysis methods reflect the strong dependence of collagen fiber structure and NP characteristics.

Both polystyrene and Targ-233, accumulated on the collagen surface of the droplet model to large, but varying degrees, larger for polystyrene than for Targ-233. Diffusion of a low level of both NPs into the collagen did occur all the way to the end of pre imaging.

5.3.3 Future directions

Developing a better model that can be used for proof of principle of an effect of acoustic radiation force in tissue, is of importance to the field of sonication and drug delivery. Research is being carried out in animals with non-cavitational FUS, often in addition to cavitational US to increase the effect of drug delivery. A simple in vitro model that prove the acoustic radiation force to be large enough for displacement of particles, could substantiate the effects claimed to arise from acoustic radiation force in vivo, in addition to guide simulations of it and parameter optimization. On the contrary, such model have the potential to disprove an effect of acoustic radiation force on NPs large enough to displace them, as well. However, many different FUS parameters and exposure settings would have to be tried out before that conclusion can be made.

Developing the model used in this project and drawing any conclusions from the use of it with acoustic radiation force is largely affected by the uncertainty of whether the droplet was in fact exposed to FUS

or not. This problem could easily be avoided by custom fabrication of well plates by the use of nano im-printing, 3D-printing or more complicated models [40]. Circular wells could be imprinted in PDMS that would hold a small volume of collagen and fit the tip of the coned transducer holder perfectly. Because the time at which the alignment issue was apparent, such well fabrication was not achievable within the timeframe.

The collagen model should be as flat as possible to simplify analysis and to limit the penetration of NPs to one plane. Several collagen models were tried out, mainly based on the thin collagen layer and collagen droplet, and combinations of the two. The various models are found in Appendix E. Especially the *NP-collagen covered collagen droplet* in Figure E.3, would be a good model of in vivo drug delivery treatments. NPs can extravasate through the blood vessel wall because of the EPR effect as explained in 2.2, and accumulate in the tissue. This model could also be modified to a collagen-NP covered colla-gen layer, in stead of a droplet. Such model would reduce the large surface accumulation as seen when collagen is covered by a NP solution. In addition, dehydration is reduced by adding the top collagen layer.

Establishment of a simple tissue model would make it possible to correlate FUS parameters to effect of penetration. The use of an in vitro model is advantageous to sacrifice less animals (although collagen is purified from rat tails) and to allow for FUS exposures of very high pressures without worrying about causing pain to an animal. The destruction of the transducer is rather the limiting factor.

6. Conclusion

Diffusion of the polystyrene bead was studied by the use of Raster Scanning Image Correlation Spectroscopy (RICS) of images obtained with a confocal laser scanning microscopy. This result was compared to results obtained in my previous project for polymeric SINTEF particles diffusing in gels.

In the diffusion analysis of polystyrene in collagen gel, no mobile particles could be detected for polystyrene in the collagen matrix. It was found to adhere fully on the collagen fibers. This stands in contrast to the result found for the well PEGylated particle, Targ-233. Its diffusion coefficient gave rise to a two-component diffusion; a mobile fraction associated with the aqueous phase of the collagen network with a diffusion coefficient similar to that in water and a fraction of particles with significantly hindered diffusivity associated with the viscous phase of the network.

The diffusion in the gel is not related to size of the particles, as the diffusion in water is, but is likely to be affected by the NPs surface modulation and charge. Th carboxylate surface modulation on polystyrene allows it to bind to the collagen, whereas the PEGylation on Targ-233 is shielding the charge and sterically limiting the interactions of the particle in the gel.

The effect of acoustic radiation force was likely overshadowed by an excessive accumulation of both NPs on the collagen surface of the droplet model. The deposition rate of NPs onto the surface was likely dependent to a larger degree on the various collagen fiber polymerization and resulting fiber volume fraction between experiments, rather than different effecst from US exposures and controls. The large and varying accumulations on the collagen surfaces suggest a strong correlation between both polystyrene and Targ-233 and fiber structure.

The deposition of polystyrene onto the collagen surface was in general larger than for Targ-233, in accordance to the diffusion analysis and the difference in surface modulation between the two NPs. Even though Targ-233 is expected to have a mobile fraction of particles in the inhomogeneous collagen matrix, the penetration of Targ-233 into the droplet could not be concluded to be larger than for polystyrene. Both particles's intensity rapidly declined right after the collagen surface. The intensity values did never reach zero, and it seems that diffusion of both polystyrene and Targ-233 is occuring all the way through the imaged section. Because no mobile particles could be detected with RICS, it is possible that polystyrene is distributed differently in a gel when applied after polymerization has occurred.

The values reached inside the droplet for Targ-233 detected with PMT detectors, of between 4.8-7.7 μg/mL implies a great diffusivity for Targ-233 in collagen gel.

The droplet model developed did not succeed in being a model for proof of principle of acoustic radiation force. However, if the interface between NP solution and water replaced with a collagen-collagen/NP interface as the collagen covered droplet in in E, it would likely be a better model for detecting acoustic radiation force in addition to being a better model for the in vivo drug delivery picture.

The strong interactions between collagen and polystyrene, suggest that it is poorly suited as a drug delivery carrier. The well PEGylated SINTEF particle, Targ-233 has a population of particles diffusing well in the collagen matrix and constitute a promising drug delivery platform.

A. Datasheet for polystyrene 0.1 yellow-green fluosphere

MOLECULAR PROBES®

CERTIFICATE OF ANALYSIS

Catalog Number	F8803
Product Name	FluoSpheres® carboxylate-modified microspheres, 0.1 µm, yellow-green fluorescent (505/515) *2% solids*
Appearance	yellow suspension
Medium	distilled water, 2 mM azide
Concentration	3.6×10^{13} particles/mL
Lot Number	1588588

SONICATE WELL BEFORE USE. STORE AT 4°C, DO NOT FREEZE

	LOT DATA	SPECIFICATION
FLUORESCENCE		
Emission Maximum	514 nm	515 ± 5 nm
Relative Quantum Yield[1]	0.49	≥ 0.30
MICROSCOPY		
Inspection	meets specification	few or no aggregates detectable after sonication
TECHNICAL DATA[2]		
Actual Particle Size	0.1 ± 0.0063 µm	n.a.
Charge	0.2839 meq/g	n.a.
Density of Polystyrene	1.055 g/cm^3	n.a.
Specific Surface Area	5.7×10^5 cm^2/g	n.a.
MISCELLANEOUS INFORMATION		
Material Lot Number	1567281	n.a.

1. *Relative to a solution in methanol of the dye used to prepare this product.*
2. *Technical data for the unstained microspheres.*

Betty Wood

Betty Wood, Quality Assurance Manager
14-Mar-2014

Life Technologies Corporation, on behalf of its Invitrogen business, Molecular Probes® labeling and detection technologies, certifies on the date above that this is an accurate record of the analysis of the subject lot and that the data conform to the specifications in effect for this product at the time of analysis.

Figure A.1

B. Gel procedure with CORNING $^{\circledR}$ COLLA-GEN1

Two batches of CORNING $^{\circledR}$ COLLAGEN 1 High Concentration (HC), RAT TAIL was used in this project.
LOT NUMBER: 4083001 at CONCENTRATION: $8.35 mg/mL$ and
LOT NUMBER: 5007031 at CONCENTRATION: $8.23 mg/mL$
The "Alternate Gelation Procedure" was followed.

Certificate of Analysis

CORNING® COLLAGEN I High Concentration (HC), RAT TAIL

Collagen I is found in most tissues and organs, but is most plentiful in dermis, tendon and bones. Type I molecule is a heterotrimer [$alpha_1(I)_2$ $alpha_2$ (I)] of 300 nm length being composed of two $alpha_1(I)$ chains and one $alpha_2(I)$ chain.[1] Collagen binding integrin receptors are $alpha_1$ $Beta_1$, $alpha_2$ $Beta_1$, and $alpha_3Beta_1$.[2] When used as a gel, collagen facilitates successful adaptation *in vitro* culture and enhances expression of cell-specific morphology and function. The Collagen HC is used in applications where a sturdy gel provides maximal support to maintain the three dimensional structure.[3-5]

CATALOG NUMBER:	354249	LOT NUMBER: _____

SOURCE: Rat tail tendon

QUANTITY: 100 milligrams protein (measured by Pyrochemiluminescence)

CONCENTRATION: _____ mg/mL

FORMULATION: 0.02 N Acetic Acid

USE: Corning Collagen I HC, rat tail, is used as a three dimensional gel. Please see reverse for gelling procedures. Use these as guidelines only - we recommend that each investigator empirically determine the optimal conditions for their unique applications.

QUALITY CONTROL: ≥ 90 % by SDS PAGE.

This product has been tested for its ability to promote the attachment and spreading of HT-1080 Human Fibrosarcoma cells.

Corning Collagen I HC, rat tail, is a membrane-filtered (0.2 micron) preparation. Tested and found negative for the presence of bacteria, fungi and mycoplasma.

STORAGE: Stable when stored at 2-8°C. **DO NOT FREEZE.**

On release this product has been successfully gelled over a wide range of dilutions and will form a gel up to a concentration of 0.3 mg/mL. Further dilution may decrease the rigidity of the gel as will the time from manufacture.

EXPIRATION DATE: _____

REFERENCES:
1. Linsenmayer, T.F., Collagen, in Cell Biology of Extracellular Matrix (ed., E.D. Hay) pp 5-37, Plenum Press, NY (1991).
2. Chan, B.M., and Hemler, M.E., J. *Cell Biol.,* **120**:537 (1993).
3. Gautreau, A., et.al., *PNAS,* **96**:7300 (1999).
4. Abir, R., et.al., *Hum. Reprod.,* **14**:1299 (1999).
5. Abir, R., et.al., *Fertil. Steril.,* **75**:141 (2001).

Suggested Coating Procedures

Gelling Procedure- Corning Collagen I HC, rat tail, will gel when its pH is brought to alkalinity using the procedure below. Please use this as a guideline for determining the optimum concentration for your application.

1) Prepare ammonia vapor chamber by taping a sterile 2 inch gauze sponge to the inside lid of a 150 mm petri dish. Saturate the gauze with ammonium hydroxide. Place lid on 150 mm dish and set aside.

CORNING

2)   Place an even coating of Corning® Collagen I HC, rat tail, on surface to be coated. Thickness may be varied as desired. 50-100 µl of Corning Collagen I HC, rat tail, is sufficient to coat a 22 mm coverslip. For dishes of 100 mm diameter, add approximately 6.0 mL per dish; for 60 mm dishes add approximately 2.3 mL and for 35 mm dishes add approximately 1.0 mL.

3)   Transfer coated coverslips or dishes with lids off to ammonia vapor chamber and expose for three minutes.

4)   Soak coated coverslip or dishes in sterile dH_2O for 30 minutes (5 mL for 35 mm dishes, 10 mL for 60 mm dishes, etc.). Aspirate and replace with 0.5-1.0 mL of sterile dH_2O and let sit overnight lidded in a laminar flow hood.

5)   Aspirate the dH_2O and replace with serum supplemented balanced salt solution and store at 2-8°C.

Alternate Gelation Procedure for Corning Collagen I HC, Rat tail

1.0   Place on ice the following:
    1.1   Corning Collagen I HC, rat tail
    1.2   Sterile 10X phosphate buffered saline (10X PBS)
    1.3   Sterile dH_2O
    1.4   Sterile 1 N NaOH

2.0   Determine the final volume of Corning Collagen I HC, rat tail, solution to be used and the desired final collagen concentration.

3.0   Place on ice a sterile tube of sufficient capacity to contain the final volume of Corning Collagen I HC, rat tail.

4.0   Perform the following steps using aseptic technique in a Class 100 Hood.

    4.1   Add to the tube the following volume of 10X PBS:

$$\frac{Final\ Volume}{10} = mL\ 10X\ PBS$$

    4.2   Calculate the volume of Corning Collagen I HC, rat tail, to be used (do not add to the tube until step 4.6):

$$\frac{Final\ volume \times Final\ collagen\ concentration\ in\ mg/mL}{Concentration\ in\ bottle\ (see\ lot\ specific\ spec.\ sheet)} = volume\ collagen\ to\ be\ added$$

    4.3   Add to the 10X PBS the following volume of sterile ice cold 1 N NaOH:

(volume collagen to be added) x 0.023 mL = volume 1 N NaOH

    4.4   Add to the 10X PBS/1 N NaOH the following volume of sterile ice-cold dH_2O:

(Final volume) - (Volume collagen) – (Volume 10X PBS) - (Volume 1 N NaOH) = Volume dH_2O to add

CORNING

4.5   Mix the contents of tube and hold in ice.

4.6   Add the calculated volume of Corning® Collagen I HC, rat tail, and mix. Leave on ice until ready for use.

5.0   The Corning Collagen I HC, rat tail, solution can be used immediately or held on ice for 2-3 hours.

6.0   When ready to use, aseptically deliver the solution into the cell culture device and allow to gel at 37°C for 30 minutes.

NOTE: For more details on Corning Collagen products and technical resources please visit support page at www.corning.com/lifesciences

---

Quality Assurance   **Date**

CORNING

C.   RICS analysis example

Analysing procedure for RICS follows and is used for both polystyrene and Targ-233. In the examples that follows, other NPs were used from my project thesis [61].

Analyzing a sample of a particle with homogeneous behavior with RICS is straight forward and more accurate as seen in an analysis example in Figure C.1. This way of analysis was performed for both nanoparticles in PBS. The intensity histogram is checked for a timeseries, and it is seen that it typically vary within small limits between images. If the intensity histogram does not vary too much (changes ± 10 % of average intensity value), all frames of a timeseries can be used for analysis. A relatively large region of interest can be chosen almost anywhere throughout a frame throughout a timeseries. The autocorrelation fitted data plot was checked and autocorrelation curves for correlation in x-axis (fast scanning axis) and y-axis (slow scanning axis) were computed. After adjusting the fitting parameters for optimal fit and checking the RICS map, the values for diffusion coefficient, number of particles and beamwaist where obtained.

For both NPs in gel, this simple analysis procedure could not be followed because of a less homogenous sample characteristic with particles diffusing at very different rates within the same region of interest. Two peaks in the autocorrelation curve would show up as a result of this inhomogeneity within the same region as seen in Figure C.2.

A smaller selection of regions for analysis of for both NPs in gel was therefore necessary. The regions of seemingly immobile particles were selected and analyzed in the first frame, and regions of mobile particles were selected and analyzed in frames throughout the sequence of images as illustrated in Figure C.3. The region of seemingly mobile character typically have stronger x-correlation (fast axis) than y-correlation (slow axis) as seen in the difference between (d) and (e). The region of seemingly immobile character have more symmetric autocorrelation. In (f) a histogram showing the intensity (y-axis) per frame (x-axis) is plotted for the whole timeseries.
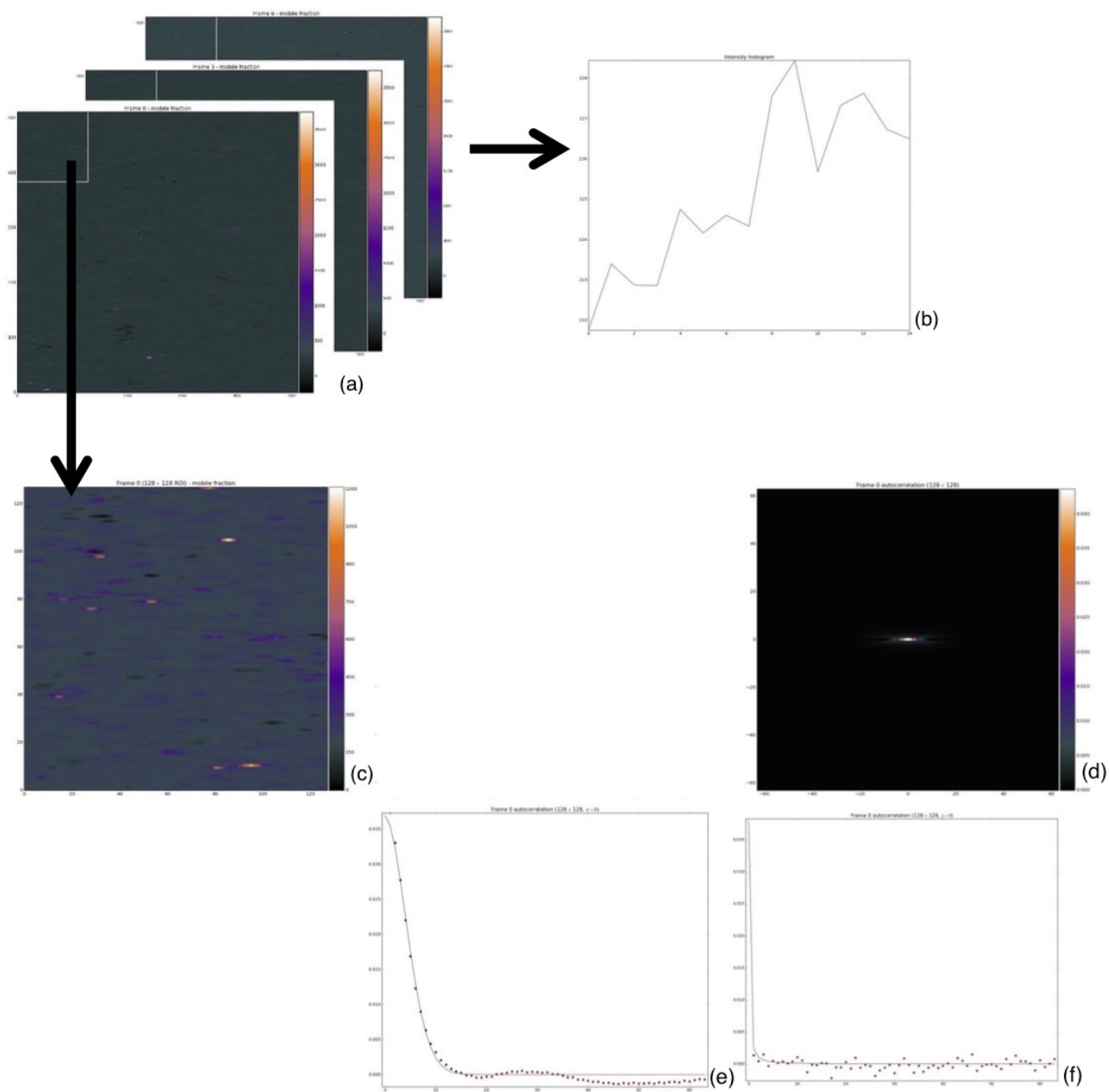
RICS analysis of NPs in solution

Figure C.1: An example of RICS MANICS analysis procedure of homogeneous samples followed in most solution samples. In (a) three frames out of a timeseries are shown. In (b) a histogram showing the intensity (y-axis) per frame (x-axis) is plotted for the whole timeseries. (c) is a selected region of interest from one frame. The fitted data for the intensity autocorrelation of particles in this region is plotted in (d). (e) and (f) shows the autocorrelation curves in x- and y-axis respectively.
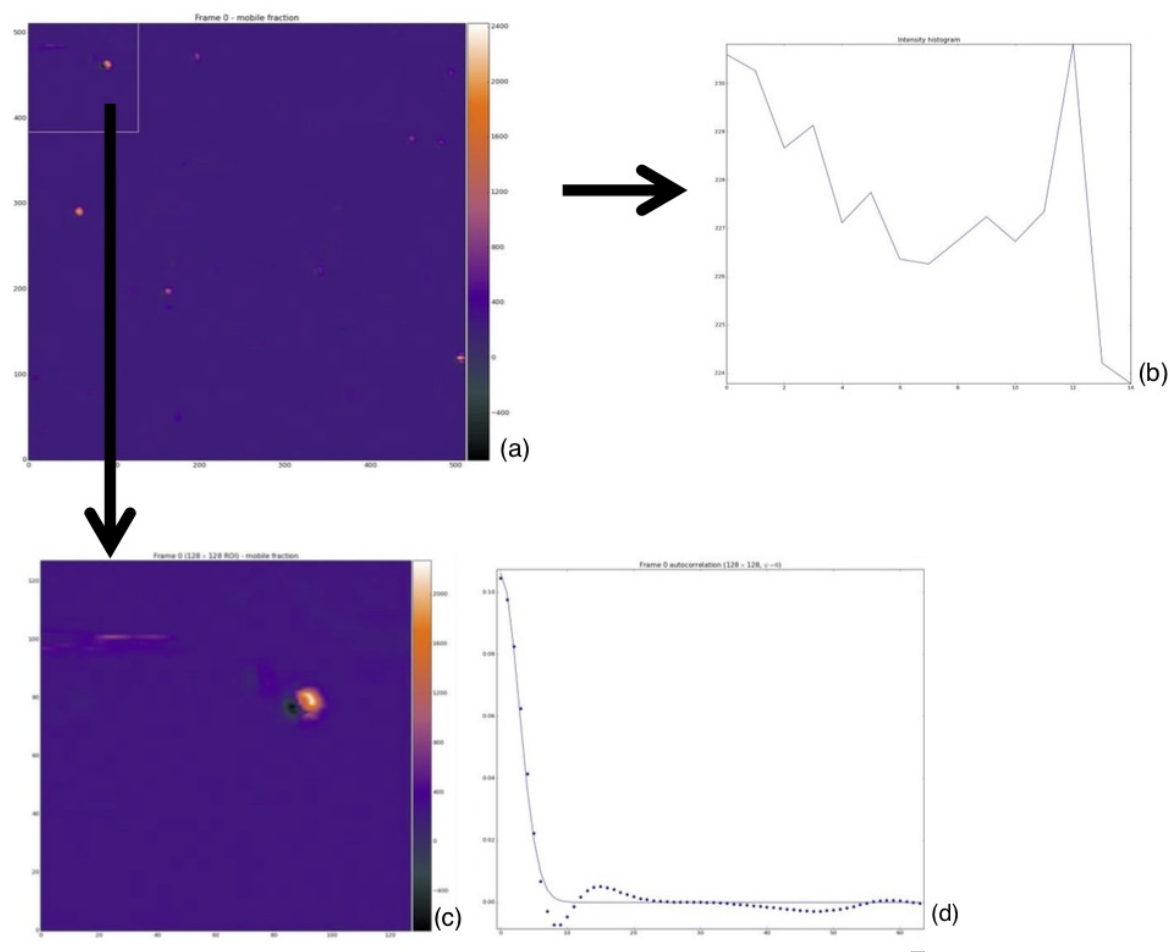
RICS analysis of NPs in collagen gel

Figure C.2: An example of a inaccurate RICS MANICS analysis procedure on inhomogeneous samples, not followed. In (a) one frame out of a timeseries is shown. In (b) a histogram showing the intensity (y-axis) per frame (x-axis) is plotted for the whole timeseries. (c) is a selected region of interest from one frame. (d) shows the autocorrelation curve in x-axis with two peaks visible indicating inhomogeneity.
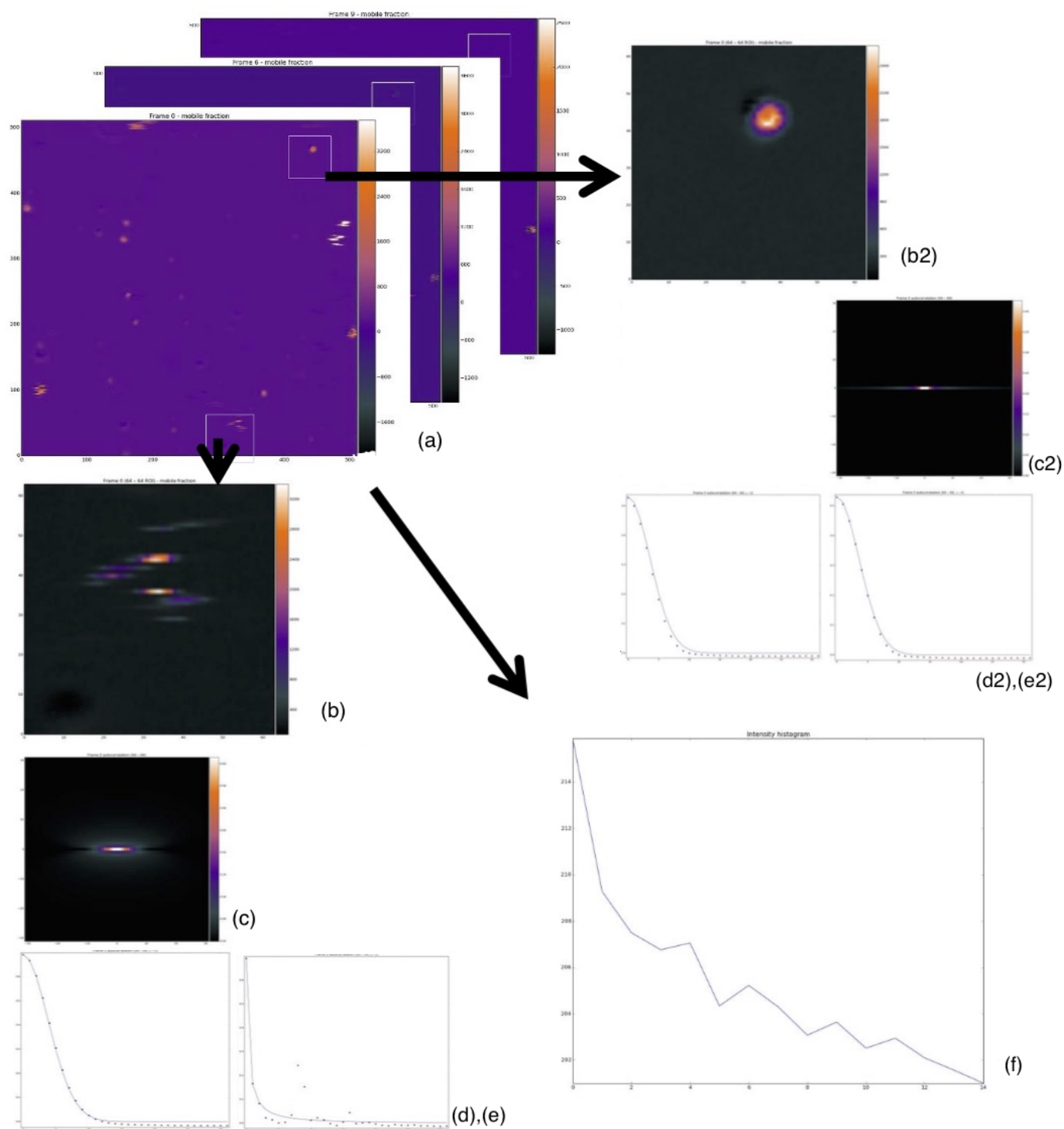
RICS analysis of NPs in collagen gel

Figure C.3: An example of RICS MANICS analysis procedure of inhomogeneous samples followed for analysis in gels. In (a) three frames out of a timeseries are shown. In (b) and (b2), two smaller selected regions of interest from one frame are chosen; one seemingly dominated by mobile particles and one by more immobile particles. The fitted data for the intensity autocorrelation of particles in this region is plotted in (c) and (c2). (d),(d2) and (e),(e2) shows the autocorrelation curves in x- and y-axis respectively for the two regions.

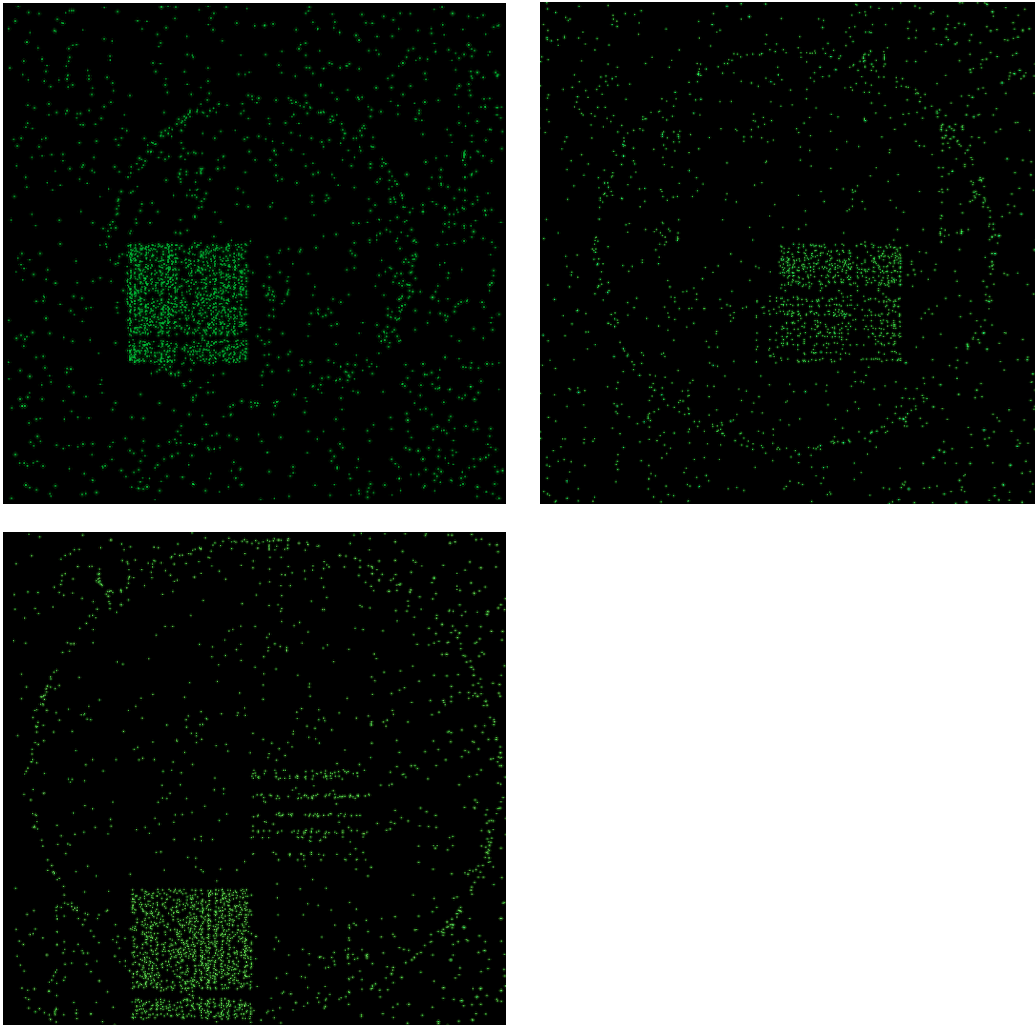# D.   Scanning error in HyD detector

Figure D.1: Three images from the fluorescence channel in the pre US tilescan for 0.6VPP US exposed Targ-233 (T06VPP). The images are highly adjusted to show the effect. This added FS has high intensity values relative to the rest of the inside of the collagen droplet.

E. Establishing method

E.0.1 Transducer on a chip

A setup by Jonas M. Ribe at NTNY (IFY), generates focussed US on a chip. A drop of collagen with polystyrene mixed in was deposited in the middle of the focus. Live video monitoring and FS was possible. However, the collagen crystalized after less than a minute, and NPs were immobile for all applied voltages.

The use of transducers on a chip or collagen in small volumes would have to be carried out in a channel or an other confined setup to avoid crystallization. This might not be straight forward to achieve with the viscous collagen solution. In addition, the FUS generated here is not the same as achieved with the Olympus transducers used in the main project.
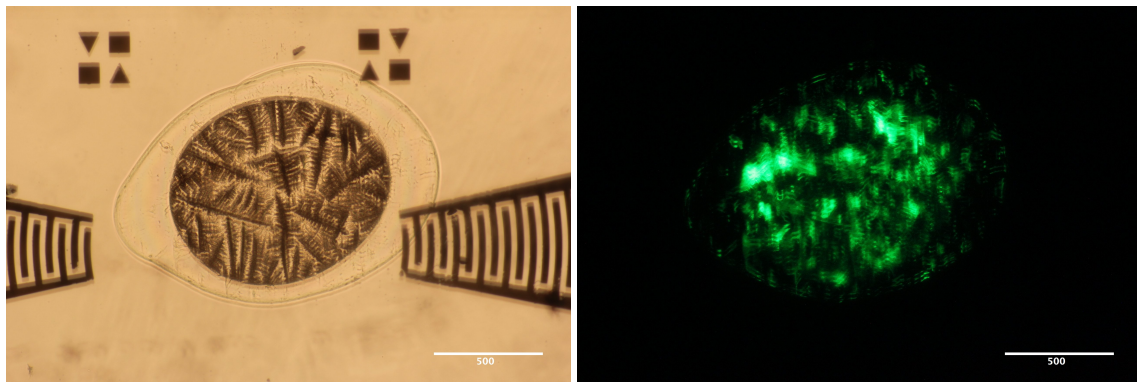
Collagen drop and transducer on a chip

Figure E.1: Transducer on a chip. Collagen-NP is placed on the chip, but is already crystalized when FUS is applied. High resolution image in a) shows the crystallization. FS image in b) shows the NPs with applied FUS, seemingly immobile.

E.0.2   Collagen layer with NPs between

This model was developed by placing a small volume of concentrated polystyrene NPs on top of a polymerized thin layer of collagen, and then covering it with a second layer of collagen. Three images from two different experiment repetitions in Figure E.2 a)-c) and d)-f) respectively, illustrates the issues of making this NP drop the same from time to time. Also, it can be seen that the concavity of the first collagen layer influence the shape of the deposited droplet.

It was difficult to place the droplet in the very middle, and be certain of hitting it with the FUS. Such models where therefore not used in later experiments.
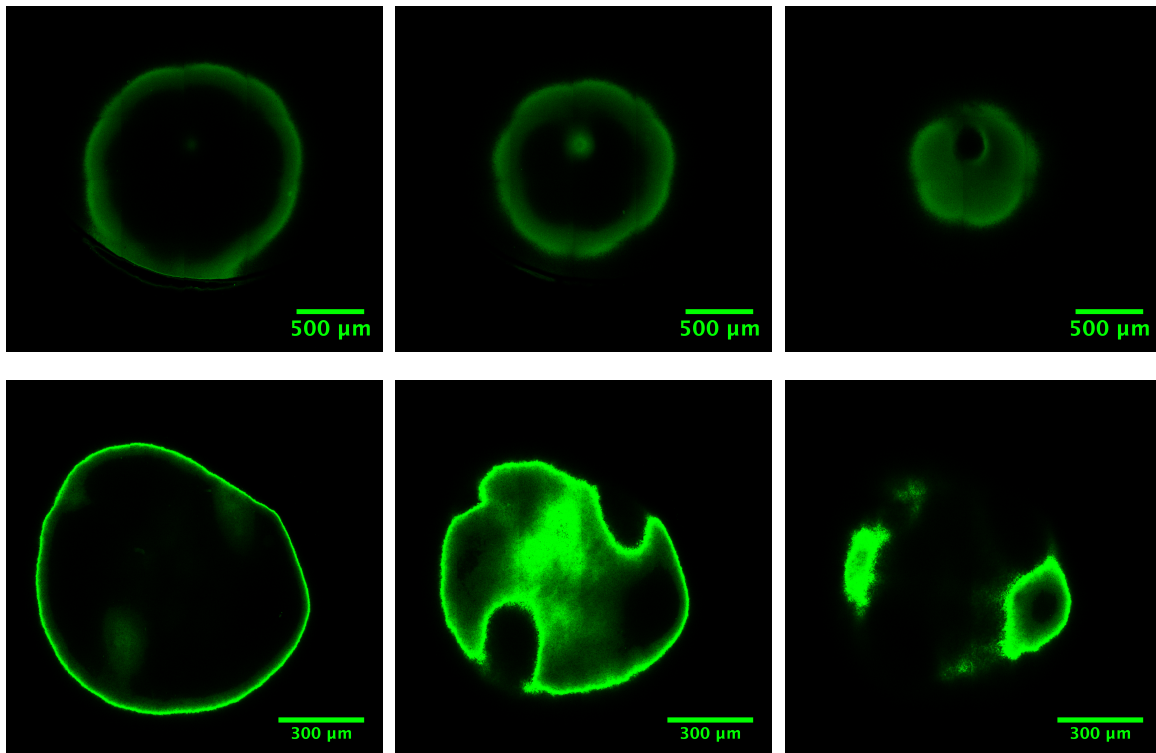
Collagen layer with NPs between

Figure E.2: a)-c) and d)-f) show FS images as a function of penetration down into the model of two separate experiment repetitions. The difference between these two image series illustrate that making the NP drop the same between experiment repetitions is difficult.

E.0.3 NP-collagen covered collagen droplet

This model contain a collagen droplet covered with a collagen layer mixed with 120 μg/mL Targ-233 NPs. This model could be a better resemble of extracellular matrix with NPs extravasated into tissue from a nearby vessel by the EPR effect. This model could also be modified into a collagen layer, in stead of a droplet, covered by a collagen-NP layer.

Experiments in this project were not using this model. This is a promising model for future experiments.

NP-collagen covered collagen droplet
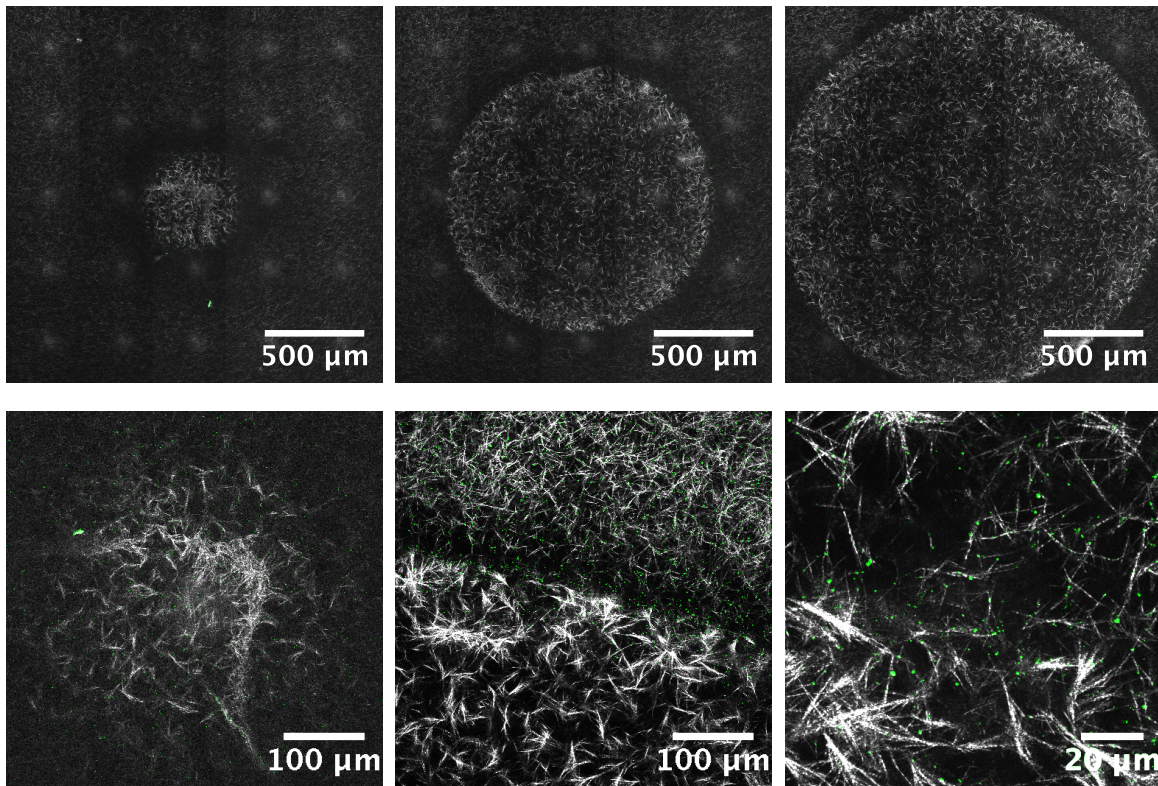
Figure E.3: a)-c) shows overlaid images of collagen (CRM) and NPs (FS) from the surface of the collagen covered droplet and deeper down into the model. d) shows the very surface of the droplet. e) and f) shows the border between the collagen droplet and the surrounding collagen layer with NPs. There seems to be an fluid filled interface between the layers, that allows for diffusion from the NP-collagen layer into the collagen only droplet.

E.0.4   10MHz US exposure and 120 μg/mL polystyrene NP solution

Ultrasound treatment of a high concentration of polystyrene beads (120 $\mu g/mL$ on top of collagen gel drops of 2.5mg/mL concentration, lead to a high accumulation of nanoparticles on top of the droplet as seen in Figure E.4, from the pre ultrasound exposure in a) to the post exposure in b). At first sight, it seemed like there also was an increased penetration of NPs into the drop. However, at these high fluorescence (FS) intensities, the aperture of the microscope can de faulty in closing all light out from other optical sections. The accumulation on top of the drop stands in contrast to the control drop that received the same handling in the experimental setup, but with no US applied. The post image in d) still has a higher intensity than the pre image in c). Aggregation seems to have occurred in both treatments, however to a larger extent for the US treated gel.

Important to note is that the total imaging time, hence the time between pre and post image was longer for the US treated drop, allowing more time for accumulation. This was avoided in later experiments, in addition to reducing the NP concentration in applied solution.

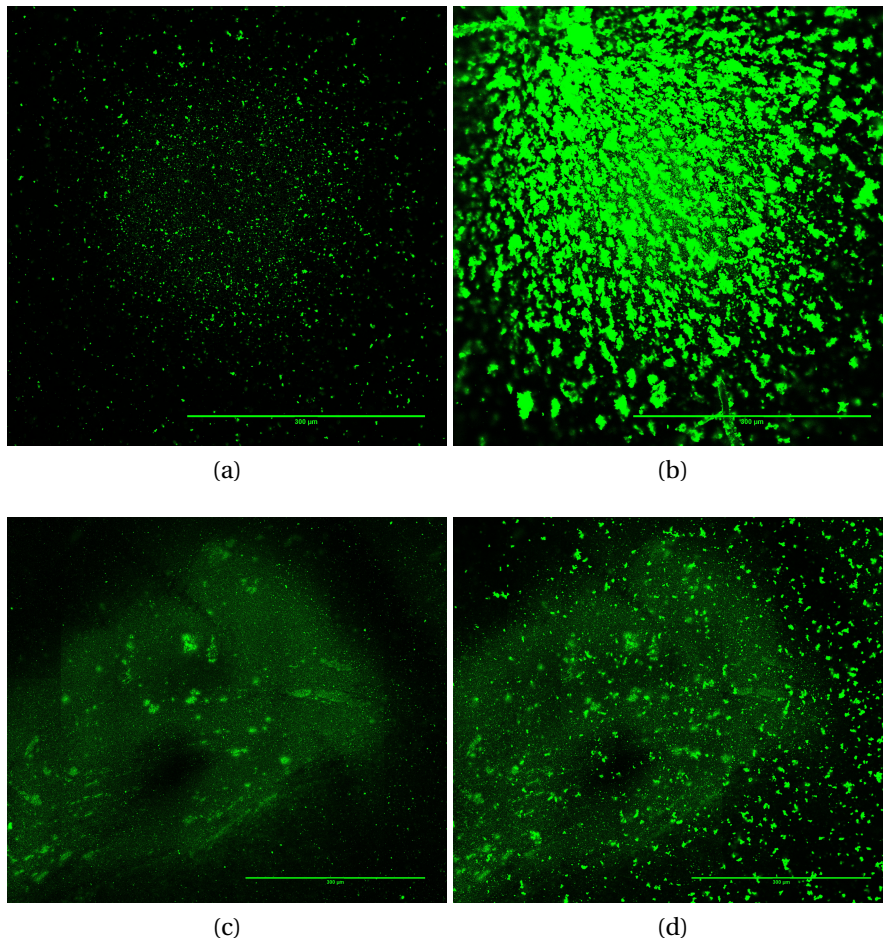(a)   (b)

(c)   (d)

Figure E.4: Collagen gels with a high concentration of NP solution is preimaged in (a) before exposed to US and the postimage is seen in (b). A control experiment is shown with preimage in (c) and postimage in (d). Scalebar: 300 μm. All images contain both collagen (CRM) and NPs (FS), although the collagen fibers are overshadowed by the FS on the surface.

E.1 Mean intensity analysis of images

The same area (450 μm)^2 and location in tile images were selected and the mean FS intensity was plotted against the penetration into the drop (z-distance in tilescans).

In Figure E.5, the resulting intensity plots for the high concentration of polystyrene is shown; a) US treated polystyrene beads, along with the control experiment in b). The difference in peak intensity between pre and post images are much larger for US treated polystyrene than the control.

This analysis method of selecting a rather large area of the convex droplet surface and plotting the mean intensity as a function of penetration, was improved later in the project. Because the surface of the collagen surface appear at a range of penetration depth values, this method overshadows most of the intensity values right inside the collagen surface, and is rather an visualization of over what range of penetration depths the surface appears in the droplet.

(a)   (b)
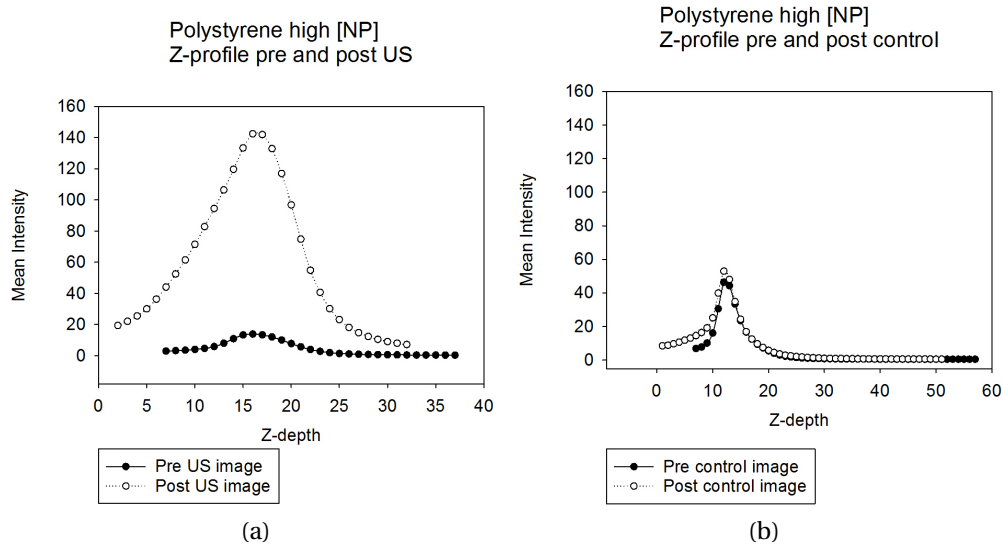
Figure E.5: Intensity plotted against penetration depth into collagen drop with high concentration of NPs. a) Polystyrene beads of high concentration treated with US, along with the control experiment in b).

For all later experiments, the NP concentration was reduced 10x before application to the collagen droplet. Imaging was done exactly the same way and for the same time for both controls and US exposed droplets. In addition an improved analysis was developed.

F. Simulation of acoustic radiation force

Based on the parameters for the FUS transducers characterization in the watertank, in house simulations were carried out by Petros Tesfamichael Yemane (IFY).

Acoustic radiation force simulates using the HIFU (High intensity focused ultrasound) propagation simulation software. In this simulation, we have used a non-linear propagation model with power law model of the extinction cross section (both absorption and scattering) for simulating incident acoustic field in medium. We have used water and tissue as propagation mediums.

The interactions of acoustic waves with medium results a transfer of momentum to the medium. This momentum can be caused by the partial absorption of the beam's energy, partial reflection of the ultrasound beam at the tissue interface, or both. Hence, the acoustic radiation force due to absorption and scattering

To calculate the acoustic radiation force in an irradiated medium, the pattern of the beam intensity, I, and the extinction cross section of the intensity must first be found. The beam propagation simulation is this study uses angular spectrum technique.

Simulations are performed over the parameter shown in table F.1. The pressure amplitude on the surface of the transducer was found experimentally in water tank measurement. The pressure waveforms, spatial distribution of the peak pressures, intensity, ultrasound (acoustic) radiation force, impulses, and heat deposition (mainly due to absorption of the wave energy) are simulated. The result obtains from this work can be used for estimating the amount of urf used on the experiment that can be used to displace the NPs.

Table F.1: US transducer parameters used in simulations

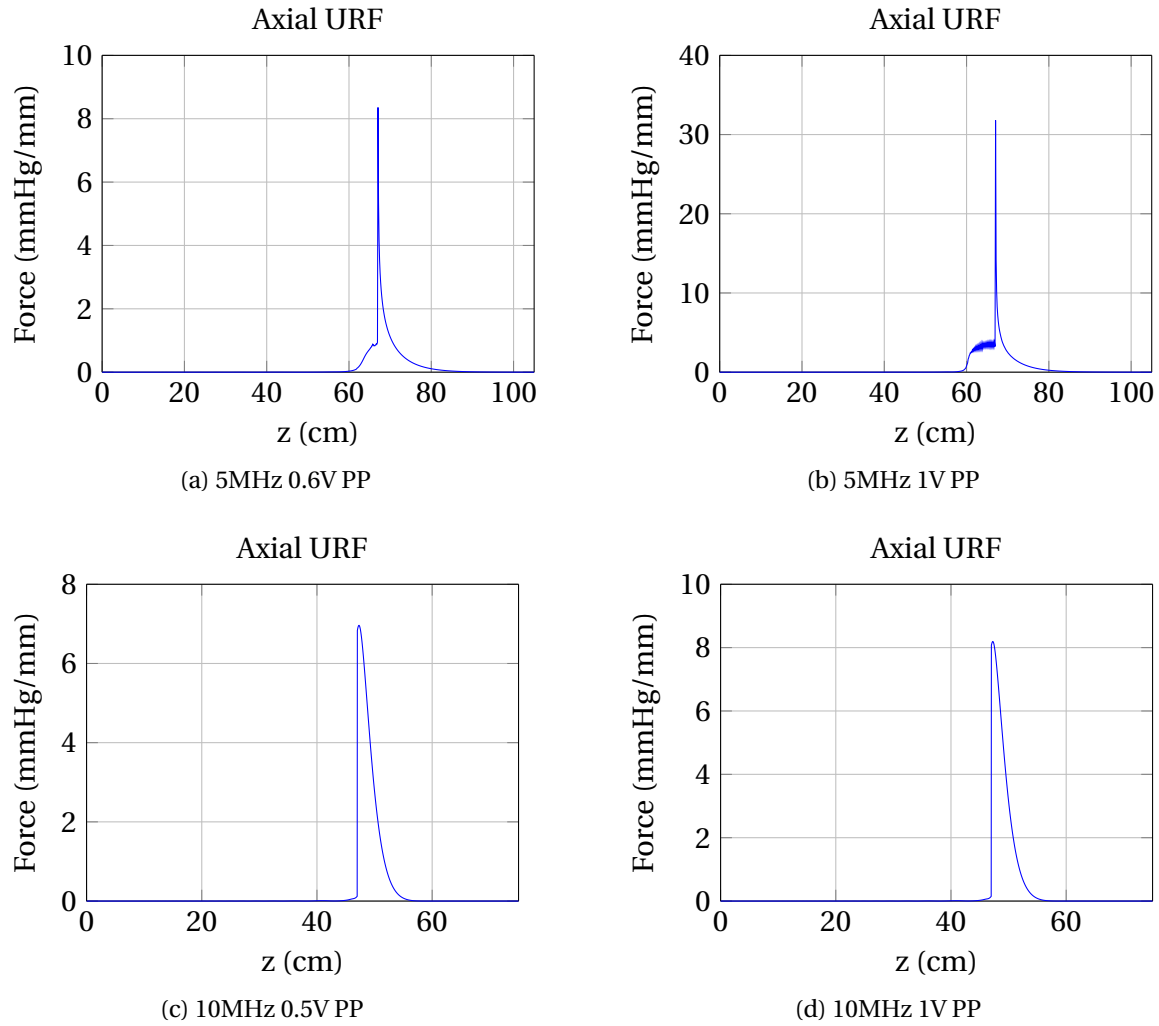| Parameters	10MHz	5MHz:
Aperature	Circular	Circular
Aperature width (mm)	19	19
Pulse length	0.5 microsec	1 microsec
Focus (mm)	50	70
Water propagation (mm)	47	67
Number of cycles	10	10
Initial surface pressure 1 (MPa)	0.1192	0.3015
Initial surface pressure 2 (MPa)	0.1040	0.1807

Acoustic radiation force

(a) 5MHz 0.6V PP

(b) 5MHz 1V PP

(c) 10MHz 0.5V PP

(d) 10MHz 1V PP

Figure F.1: .

Max streaming velocity

(a) 5MHz 0.6V PP

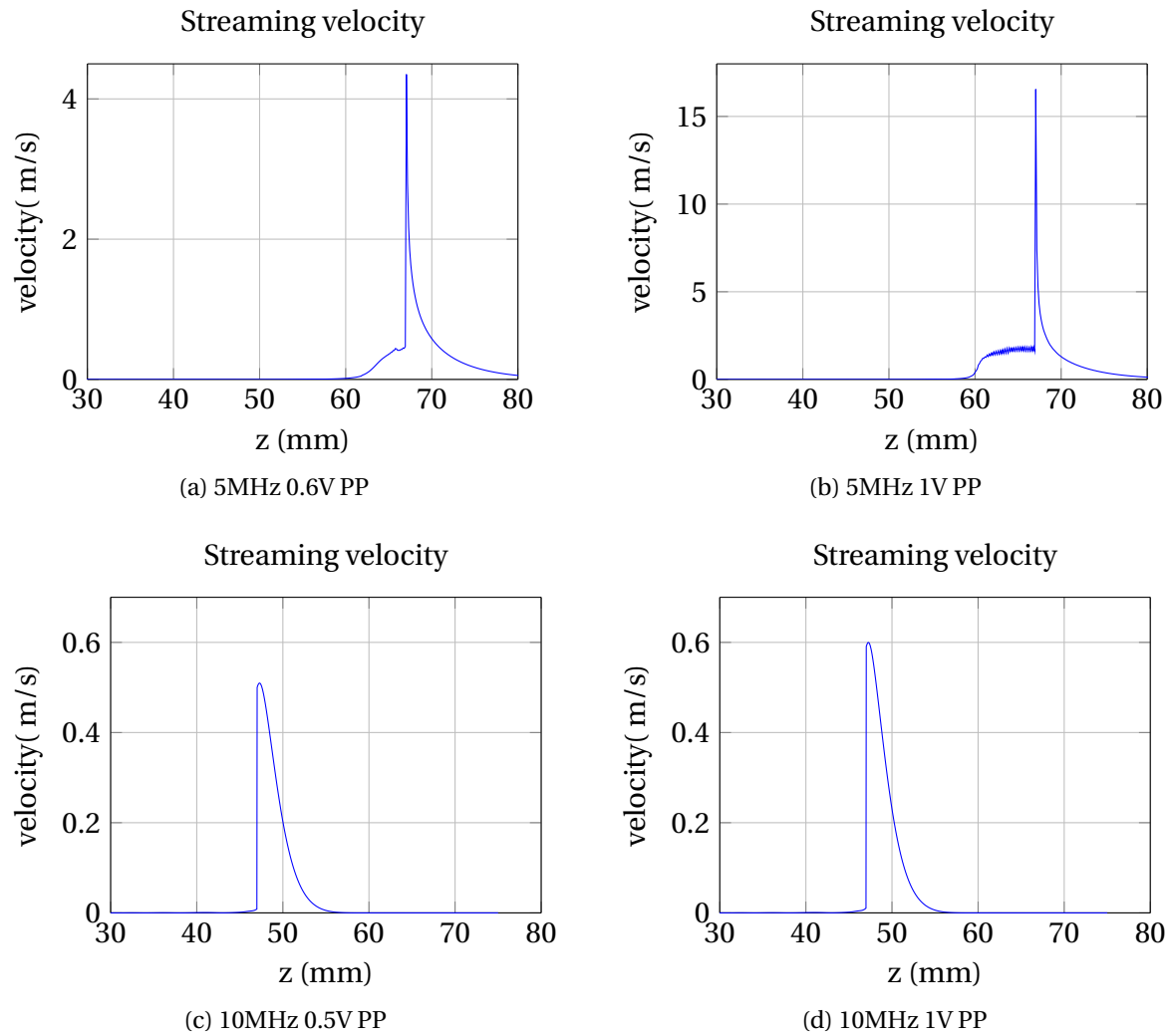(b) 5MHz 1V PP

(c) 10MHz 0.5V PP

(d) 10MHz 1V PP

Figure F.2: .

Bibliography

[1] Ahmed, E. M. (2015). Hydrogel: Preparation, characterization, and applications: A review. *Journal of Advanced Research*, 6(2):105 – 121.

[2] Aitken, K. J. and Bagli, D. J. (2009). The bladder extracellular matrix. part i: architecture, development and disease. *Nat Rev Urol*, 6(11):596–611.

[3] Albani, J. (2011). *Structure and Dynamics of Macromolecules: Absorption and Fluorescence Studies: Absorption and Fluorescence Studies*. Elsevier.

[4] Alexandrakis, G., Brown, E. B., Tong, R. T., McKee, T. D., Campbell, R. B., Boucher, Y., and Jain, R. K. (2004). Two-photon fluorescence correlation microscopy reveals the two-phase nature of transport in tumors. *Nat Med*, 10(2):203–207.

[5] Behr, T. M., Becker, W. S., Sharkey, R. M., Juweid, M. E., Dunn, R. M., Bair, H. J., Wolf, F. G., and Goldenberg, D. M. (1996). Reduction of renal uptake of monoclonal antibody fragments by amino acid infusion. *J Nucl Med*, 37(5):829–833.

[6] Boles, M. A., Ling, D., Hyeon, T., and Talapin, D. V. (2016). The surface science of nanocrystals. *Nat Mater*, 15(2):141–153.

[7] Boucher, Y., Baxter, L. T., and Jain, R. K. (1990). Interstitial pressure gradients in tissue-isolated and subcutaneous tumors: implications for therapy. *Cancer Res*, 50(15):4478–4484.

[8] Brown, C. M., Dalal, R. B., Hebert, B., Digman, M. A., Horwitz, A. R., and Gratton, E. (2008). Raster image correlation spectroscopy (rics) for measuring fast protein dynamics and concentrations with a commercial laser scanning confocal microscope. *J Microsc*, 229(Pt 1):78–91.

[9] Brown, E. B., Boucher, Y., Nasser, S., and Jain, R. K. (2004). Measurement of macromolecular diffusion coefficients in human tumors. *Microvasc Res*, 67(3):231–236.

[10] Bruce Alberts, Alexander Johnson, J. L. M. R. K. R. and Walter., P. (2002). *Molecular Biology of the Cell, 4th edition*. New York: Garland Science.

[11] Cechowska-Pasko, M., Palka, J., and Wojtukiewicz, M. Z. (2006). Enhanced prolidase activity and decreased collagen content in breast cancer tissue. *Int J Exp Pathol*, 87(4):289–296.

[12] Chandra, B., Subramaniam, R., Mallik, S., and Srivastava, D. K. (2006). Formulation of photocleavable liposomes and the mechanism of their content release. *Org Biomol Chem*, 4(9):1730–1740.

[13] Chaudhari, K. R., Ukawala, M., Manjappa, A. S., Kumar, A., Mundada, P. K., Mishra, A. K., Mathur, R., Monkkonen, J., and Murthy, R. S. R. (2012). Opsonization, biodistribution, cellular uptake and apoptosis study of pegylated pbca nanoparticle as potential drug delivery carrier. *Pharm Res*, 29(1):53–68.

[14] Chauhan, V. P. and Jain, R. K. (2013). Strategies for advancing cancer nanomedicine. *Nat Mater*, 12(11):958–962.

[15] Chauhan, V. P., Lanning, R. M., Diop-Frimpong, B., Mok, W., Brown, E. B., and Padera (2009). Multiscale measurements distinguish cellular and interstitial hindrances to diffusion in vivo. *Biophys J*, 97(1):330–336.

[16] Clague, David S.; Phillips, R. J. (1997). A numerical calculation of the hydraulic permeability of three-dimensional disordered fibrous media. *Physics of Fluids*.

[17] Corrie, P. G. Cytotoxic chemotherapy: clinical aspects. *Medicine*, 36(1):24–28.

[18] Couvreur, P., Kante, B., Lenaerts, V., Scailteur, V., Roland, M., and Speiser, P. (1980). Tissue distribution of antitumor drugs associated with polyalkylcyanoacrylate nanoparticles. *J Pharm Sci*, 69(2):199–202.

[19] Cowman, M. K., Li, M., and Balazs, E. A. (1998). Tapping mode atomic force microscopy of hyaluronan: extended and intramolecularly interacting chains. *Biophys J*, 75(4):2030–2037.

[20] Cox, T. R. and Erler, J. T. (2011). Remodeling and homeostasis of the extracellular matrix: implications for fibrotic diseases and cancer. *Dis Model Mech*, 4(2):165–178.

[21] Cu, Y. and Saltzman, W. M. (2009). Controlled surface modification with poly(ethylene)glycol enhances diffusion of plga nanoparticles in human cervical mucus. *Mol Pharm*, 6(1):173–181.

[22] Davies, C. d. L., Lundstrom, L. M., Frengen, J., Eikenes, L., Bruland S, O. S., Kaalhus, O., Hjelstuen, M. H. B., and Brekken, C. (2004). Radiation improves the distribution and uptake of liposomal doxorubicin (caelyx) in human osteosarcoma xenografts. *Cancer Res*, 64(2):547–553.

[23] Dayton, P. A., Allen, J. S., and Ferrara, K. W. (2002). The magnitude of radiation force on ultrasound contrast agents. *J Acoust Soc Am*, 112(5 Pt 1):2183–2192.

[24] Deen, W. M., Satvat, B., and Jamieson, J. M. (1980). Theoretical model for glomerular filtration of charged solutes. *Am J Physiol*, 238(2):F126–39.

[25] Dellian, M., Yuan, F., Trubetskoy, V. S., Torchilin, V. P., and Jain, R. K. (2000). Vascular permeability in a human tumour xenograft: molecular charge dependence. *Br J Cancer*, 82(9):1513–1518.

[26] Digman, M. A., Brown, C. M., Sengupta, P., Wiseman, P. W., Horwitz, A. R., and Gratton, E. (2005a). Measuring fast dynamics in solutions and cells with a laser scanning microscope. *Biophys J*, 89(2):1317–1327.

[27] Digman, M. A., Sengupta, P., Wiseman, P. W., Brown, C. M., Horwitz, A. R., and Gratton, E. (2005b). Fluctuation correlation spectroscopy with a laser-scanning microscope: exploiting the hidden time structure. *Biophys J*, 88(5):L33–6.

[28] Dowd, C. J., Cooney, C. L., and Nugent, M. A. (1999). Heparan sulfate mediates bfgf transport through basement membrane by diffusion with rapid reversible binding. *J Biol Chem*, 274(8):5236–5244.

[29] Eikenes, L., Tari, M., Tufto, I., Bruland, O. S., and de Lange Davies, C. (2005). Hyaluronidase induces a transcapillary pressure gradient and improves the distribution and uptake of liposomal doxorubicin (caelyx) in human osteosarcoma xenografts. *Br J Cancer*, 93(1):81–88.

[30] Erikson, A., Andersen, H. N., Naess, S. N., Sikorski, P., and Davies, C. d. L. (2008). Physical and chemical modifications of collagen gels: impact on diffusion. *Biopolymers*, 89(2):135–143.

[31] Frenkel, V. (2008). Ultrasound mediated delivery of drugs and genes to solid tumors. *Adv Drug Deliv Rev*, 60(10):1193–1208.

[32] Frenkel, V., Kimmel, E., and Iger, Y. (2000). Ultrasound-facilitated transport of silver chloride (agcl) particles in fish skin. *J Control Release*, 68(2):251–261.

[33] Friedrich, F., Klehs, K., Fichte, M. A. H., Junek, S., Heilemann, M., and Heckel, A. (2015). A two-photon activatable amino acid linker for the induction of fluorescence. *Chem. Commun.*, 51:15382–15385.

[34] Frohlich, E. and Roblegg, E. (2014). Mucus as barrier for drug delivery by nanoparticles. *J Nanosci Nanotechnol*, 14(1):126–136.

[35] Garcia-Fuentes, M., Torres, D., Martín-Pastor, M., , and Alonso, M. J. (2004). Application of nmr spectroscopy to the characterization of peg-stabilized lipid nanoparticles. *Langmuir*, 20(20):8839–8845. PMID: 15379515.

[36] Graf, A., McDowell, A., and Rades, T. (2009). Poly(alkylcyanoacrylate) nanoparticles for enhanced delivery of therapeutics - is there real potential? *Expert Opin Drug Deliv*, 6(4):371–387.

[37] Griffiths, G., Nystrom, B., Sable, S. B., and Khuller, G. K. (2010). Nanobead-based interventions for the treatment and prevention of tuberculosis. *Nat Rev Microbiol*, 8(11):827–834.

[38] Groner, N., Capoulade, J., Cremer, C., and Wachsmuth, M. (2010). Measuring and imaging diffusion with multiple scan speed image correlation spectroscopy. *Opt Express*, 18(20):21225–21237.

[39] Halper, J. and Kjaer, M. (2014). Basic components of connective tissues and extracellular matrix: elastin, fibrillin, fibulins, fibrinogen, fibronectin, laminin, tenascins and thrombospondins. *Adv Exp Med Biol*, 802:31–47.

[40] Herland, A., van der Meer, A. D., FitzGerald, E. A., Park, T.-E., Sleeboom, J. J. F., and Ingber, D. E. (2016). Distinct contributions of astrocytes and pericytes to neuroinflammation identified in a 3d human blood-brain barrier on a chip. *PLoS One*, 11(3):e0150360.

[41] Hobbs, S. K., Monsky, W. L., Yuan, F., Roberts, W. G., Griffith, L., Torchilin, V. P., and Jain, R. K. (1998). Regulation of transport pathways in tumor vessels: role of tumor type and microenvironment. *Proc Natl Acad Sci U S A*, 95(8):4607–4612.

[42] Howard, L. (2006). Wikimedia commons (public domain).

[43] ibidi GmbH. *Application Note 26: Fabrication of Collagen 1 Gels.*

[44] Iborra, H. R. (2014). Characterization of ultrasound transducers. Master's thesis, Universidad Autónoma de Madrid.

[45] Issa, B., Obaidat, I. M., Albiss, B. A., and Haik, Y. (2013). Magnetic nanoparticles: surface effects and properties related to biomedicine applications. *Int J Mol Sci*, 14(11):21266–21305.

[46] Jain, R. K. (1987). Transport of molecules in the tumor interstitium: a review. *Cancer Res*, 47(12):3039–3051.

[47] Jain, R. K. and Stylianopoulos, T. (2010). Delivering nanomedicine to solid tumors. *Nat Rev Clin Oncol*, 7(11):653–664.

[48] Johnson, E. M., Berk, D. A., Jain, R. K., and Deen, W. M. (1996). Hindered diffusion in agarose gels: test of effective medium model. *Biophys J*, 70(2):1017–1023.

[49] Jokerst JV, Lobovkina T, Z. R. G. S. (2011). Nanoparticle pegylation for imaging and therapy. *Nanomedicine (London, England).*

[50] Karp, G. (2010). *Cell and Molecular Biology Concepts and Experiments 6th edition.*

[51] Kim, K.-P., Cha, J.-D., Jang, E.-H., Klumpp, J., Hagens, S., Hardt, W.-D., Lee, K.-Y., and Loessner, M. J. (2008). Pegylation of bacteriophages increases blood circulation time and reduces t-helper type 1 immune response. *Microb Biotechnol*, 1(3):247–257.

[52] Klymchenko, A. S., Roger, E., Anton, N., Anton, H., Shulov, I., Vermot, J., Mely, Y., and Vandamme, T. F. (2012). Highly lipophilic fluorescent dyes in nano-emulsions: towards bright non-leaking nano-droplets. *RSC Adv.*, 2:11876–11886.

[53] Kong, G. and Dewhirst, M. (1999). Hyperthermia and liposomes. *International journal of hyperthermia : the official journal of European Society for Hyperthermic Oncology, North American Hyperthermia Group*, 15(5):345—370.

[54] Kratz, F., Drevs, J., Bing, G., Stockmar, C., Scheuermann, K., Lazar, P., and Unger, C. (2001). Development and in vitro efficacy of novel mmp2 and mmp9 specific doxorubicin albumin conjugates. *Bioorg Med Chem Lett*, 11(15):2001–2006.

[55] Kumari, A., Yadav, S. K., and Yadav, S. C. (2010). Biodegradable polymeric nanoparticles based drug delivery systems. *Colloids and Surfaces B: Biointerfaces*, 75(1):1 – 18.

[56] Lacava, L. M., Lacava, Z. G., Da Silva, M. F., Silva, O., Chaves, S. B., Azevedo, R. B., Pelegrini, F., Gansau, C., Buske, N., Sabolovic, D., and Morais, P. C. (2001). Magnetic resonance of a dextran-coated magnetic fluid intravenously administered in mice. *Biophys J*, 80(5):2483–2486.

[57] Leddy, H. A., Haider, M. A., and Guilak, F. (2006). Diffusional anisotropy in collagenous tissues: fluorescence imaging of continuous point photobleaching. *Biophys J*, 91(1):311–316.

[58] Lelu, S., Strand, S. P., Steine, J., and Davies, C. d. L. (2011). Effect of pegylation on the diffusion and stability of chitosan-dna polyplexes in collagen gels. *Biomacromolecules*, 12(10):3656–3665.

[59] Levik, K. V. (2015). Intracellular localization of polymeric nanoparticles and the effect of encapsulated drug in vitro. Master's thesis, Institutt for fysikk, NTNU.

[60] Lieleg, O., Baumgartel, R. M., and Bausch, A. R. (2009). Selective filtering of particles by the extracellular matrix: an electrostatic bandpass. *Biophys J*, 97(6):1569–1577.

[61] Løvmo, M. K. (2015). Diffusion of nanoparticles in extra cellular matrix - resembled by collagen gels. Project thesis, NTNU.

[62] MacEwan, S. R., Callahan, D. J., and Chilkoti, A. (2010). Stimulus-responsive macromolecules and nanoparticles for cancer drug delivery. *Nanomedicine (Lond)*, 5(5):793–806.

[63] MATLAB (2014). *version 8.3.0.532 (R2014a)*. The MathWorks Inc., Natic, Massachusetts.

[64] McPherson, J. M., Wallace, D. G., Sawamura, S. J., Conti, A., Condell, R. A., Wade, S., and Piez, K. A. (1985). Collagen fibrillogenesis in vitro: a characterization of fibril quality as a function of assembly conditions. *Coll Relat Res*, 5(2):119–135.

[65] Milla, P., Dosio, F., and Cattel, L. (2012). Pegylation of proteins and liposomes: a powerful and flexible strategy to improve the drug delivery. *Curr Drug Metab*, 13(1):105–119.

[66] Mo, S., Coussios, C.-C., Seymour, L., and Carlisle, R. (2012). Ultrasound-enhanced drug delivery for cancer. *Expert Opin Drug Deliv*, 9(12):1525–1538.

[67] Moghimi, S. M., Hunter, A. C., and Murray, J. C. (2001). Long-circulating and target-specific nanoparticles: theory to practice. *Pharmacol Rev*, 53(2):283–318.

[68] Morch, Y., Hansen, R., Berg, S., Aslund, A. K. O., Glomm, W. R., Eggen, S., Schmid, R., Johnsen, H., Kubowicz, S., Snipstad, S., Sulheim, E., Hak, S., Singh, G., McDonagh, B. H., Blom, H., de Lange Davies, C., and Stenstad, P. M. (2015). Nanoparticle-stabilized microbubbles for multimodal imaging and drug delivery. *Contrast Media Mol Imaging*.

[69] Nadiarnykh, O., LaComb, R. B., Brewer, M. A., and Campagnola, P. J. (2010). Alterations of the extracellular matrix in ovarian cancer studied by second harmonic generation imaging microscopy. *BMC Cancer*, 10:94.

[70] Netti, P. A., Berk, D. A., Swartz, M. A., Grodzinsky, A. J., and Jain, R. K. (2000). Role of extracellular matrix assembly in interstitial transport in solid tumors. *Cancer Res*, 60(9):2497–2503.

[71] Norris, S. C. P., Humpolickova, J., Amler, E., Huranova, M., Buzgo, M., Machan, R., Lukas, D., and Hof, M. (2011). Raster image correlation spectroscopy as a novel tool to study interactions of macromolecules with nanofiber scaffolds. *Acta Biomater*, 7(12):4195–4203.

[72] Owens, D. E. r. and Peppas, N. A. (2006). Opsonization, biodistribution, and pharmacokinetics of polymeric nanoparticles. *Int J Pharm*, 307(1):93–102.

[73] Page-McCaw, A., Ewald, A. J., and Werb, Z. (2007). Matrix metalloproteinases and the regulation of tissue remodelling. *Nat Rev Mol Cell Biol*, 8(3):221–233.

[74] Pisal, D. S., Kosloski, M. P., and Balu-Iyer, S. V. (2010). Delivery of therapeutic proteins. *J Pharm Sci*, 99(6):2557–2575.

[75] Pitt, W. G., Husseini, G. A., and Staples, B. J. (2004). Ultrasonic drug delivery–a general review. *Expert Opin Drug Deliv*, 1(1):37–56.

[76] Pluen, A., Boucher, Y., Ramanujan, S., McKee, T. D., Gohongi, T., di Tomaso, E., Brown, E. B., Izumi, Y., Campbell, R. B., Berk, D. A., and Jain, R. K. (2001). Role of tumor-host interactions in interstitial diffusion of macromolecules: cranial vs. subcutaneous tumors. *Proc Natl Acad Sci U S A*, 98(8):4628–4633.

[77] Pluen, A., Netti, P. A., Jain, R. K., and Berk, D. A. (1999). Diffusion of macromolecules in agarose gels: comparison of linear and globular configurations. *Biophys J*, 77(1):542–552.

[78] Pozzi, D., Colapicchioni, V., Caracciolo, G., Piovesana, S., Capriotti, A. L., Palchetti, S., De Grossi, S., Riccioli, A., Amenitsch, H., and Lagana, A. (2014). Effect of polyethyleneglycol (peg) chain length on the bio-nano-interactions between pegylated lipid nanoparticles and biological fluids: from nanostructure to uptake in cancer cells. *Nanoscale*, 6(5):2782–2792.

[79] Quaglia, F., Ostacolo, L., De Rosa, G., La Rotonda, M. I., Ammendola, M., Nese, G., Maglio, G., Palumbo, R., and Vauthier, C. (2006). Nanoscopic core-shell drug carriers made of amphiphilic triblock and star-diblock copolymers. *Int J Pharm*, 324(1):56–66.

[80] Ramanujan, S., Pluen, A., McKee, T. D., Brown, E. B., Boucher, Y., and Jain, R. K. (2002). Diffusion and convection in collagen gels: Implications for transport in the tumor interstitium. *Biophysical Journal*, 83(3):1650 – 1660.

[81] Roberts, M. J., Bentley, M. D., and Harris, J. M. (2002). Chemistry for peptide and protein pegylation. *Adv Drug Deliv Rev*, 54(4):459–476.

[82] Rosenberg, L., Hellmann, W., and Kleinschmidt, A. K. (1975). Electron microscopic studies of proteoglycan aggregates from bovine articular cartilage. *J Biol Chem*, 250(5):1877–1883.

[83] Schindelin, J., Arganda-Carreras, I., Frise, E., Kaynig, V., Longair, M., Pietzsch, T., Preibisch, S., Rueden, C., Saalfeld, S., Schmid, B., Tinevez, J.-Y., White, D. J., Hartenstein, V., Eliceiri, K., Tomancak, P., and Cardona, A. (2012). Fiji: an open-source platform for biological-image analysis. *Nat Methods*, 9(7):676–682.

[84] Schneider, C. A., Rasband, W. S., and Eliceiri, K. W. (2012). Nih image to imagej: 25 years of image analysis. *Nat Methods*, 9(7):671–675.

[85] Schneider, M., Stracke, F., Hansen, S., and Schaefer, U. F. (2009). Nanoparticles and their interactions with the dermal barrier. *Dermatoendocrinol*, 1(4):197–206.

[86] Scientific, T. F. Protein biology resource library: Fluorescent probes.

[87] Sethuraman, V. A., Lee, M. C., and Bae, Y. H. (2008). A biodegradable ph-sensitive micelle system for targeting acidic solid tumors. *Pharm Res*, 25(3):657–666.

[88] SigmaPlot (2013). *version 13.0*. Systat Software Inc., San Jose California, USA.

[89] Snipstad, S., Hak, S., Baghirov, H., Sulheim, E., Mørch, Ý., Lélu, S., von Haartman, E., Bäck, M., Nilsson, K. P. R., Klymchenko, A. S., de Lange Davies, C., and Åslund, A. K. O. (2016). Labeling nanoparticles: Dye leakage and altered cellular uptake. *Cytometry Part A*, pages n/a–n/a.

[90] Sokka, S. D., King, R., and Hynynen, K. (2003). Mri-guided gas bubble enhanced ultrasound heating in in vivo rabbit thigh. *Physics in Medicine and Biology*, 48(2):223.

[91] Strable, E., Bulte, J. W. M., Moskowitz, B., Vivekanandan, K., Allen, M., , and Douglas, T. (2001). Synthesis and characterization of soluble iron oxide-dendrimer composites. *Chemistry of Materials*, 13(6):2201–2209.

[92] Stylianopoulos, T., Diop-Frimpong, B., Munn, L. L., and Jain, R. K. (2010a). Diffusion anisotropy in collagen gels and tumors: the effect of fiber network orientation. *Biophys J*, 99(10):3119–3128.

[93] Stylianopoulos, T., Poh, M.-Z., Insin, N., Bawendi, M. G., Fukumura, D., Munn, L. L., and Jain, R. K. (2010b). Diffusion of particles in the extracellular matrix: the effect of repulsive electrostatic interactions. *Biophys J*, 99(5):1342–1349.

[94] Sulheim, E. (2014). Mechanisms of cellular uptake and intracellular degradation of polymeric nanoparticles. Master's thesis, Institutt for fysikk, NTNU.

[95] Sung, K. E., Su, G., Pehlke, C., Trier, S. M., Eliceiri, K. W., Keely, P. J., Friedl, A., and Beebe, D. J. (2009). Control of 3-dimensional collagen matrix polymerization for reproducible human mammary fibroblast cell culture in microfluidic devices. *Biomaterials*, 30(27):4833–4841.

[96] Thorne, R. G., Lakkaraju, A., Rodriguez-Boulan, E., and Nicholson, C. (2008). In vivo diffusion of lactoferrin in brain extracellular space is regulated by interactions with heparan sulfate. *Proc Natl Acad Sci U S A*, 105(24):8416–8421.

[97] Verhoef, J. J. F. and Anchordoquy, T. J. (2013). Questioning the use of pegylation for drug delivery. *Drug Deliv Transl Res*, 3(6):499–503.

[98] WHO (2015). Cancer, fact sheet n°297.

[99] WOOD, G. C. and KEECH, M. K. (1960). The formation of fibrils from collagen solutions. 1. the effect of experimental conditions: kinetic and electron-microscope studies. *Biochem J*, 75:588–598.

[100] Zeiss, C. (2001). *CONFORCOR APPLICATIONS Manual LSM 510 - Confor 2.*

[101] Zhang, W. (2014). Nanoparticle aggregation: principles and modeling. *Adv Exp Med Biol*, 811:19–43.